NUMERICAL SIMULATION AND EXPERIMENTAL STUDY OF TRANSIENT LIQUID PHASE BONDING OF SINGLE CRYSTAL SUPERALLOYS

by

Adam Ghoneim

A Thesis submitted to the Faculty of Graduate Studies of

The University of Manitoba

in partial fulfillment of the requirements of the degree of

DOCTOR OF PHILOSOPHY

Department of Mechanical and Manufacturing Engineering

University of Manitoba

Winnipeg, Manitoba

ABSTRACT

A major factor that has limited commercial exploitation of the benefits of transient liquid phase (TLP) bonding to joining of difficult-to-bond single crystal nickel base superalloys is prolonged isothermal solidification time, t_f, that is required to produce reliable joints free of deleterious eutectic microconstituents. The primary goals of the research in this dissertation are to perform a systematic study to identify and understand the fundamental cause of prolonged t_f and use the acquired knowledge to develop an effective way to reduce it without sacrificing the single crystalline nature of the base materials. To achieve these objectives, a multi-scale numerical modeling approach was developed, using a 2-D fully implicit moving-mesh finite element method and a cellular automata method, to theoretically investigate the cause of the long t_f and determine a viable way to minimize the problem. Subsequently, the predictions of the theoretical models are experimentally validated.

Whilst it has been previously suggested that the absence of a high diffusivity path through grain boundaries is a likely factor that causes long t_f in single crystals, numerical calculations and experimental verifications have shown that enhanced intergranular diffusivity has a negligible effect on t_f in cast superalloys and that another important factor must be responsible. In addition, it was found that the concept of competition between solute diffusivity and solubility as predicted by standard analytical TLP bonding models and reported in the literature as a possible cause of long t_f is not suitable to explain salient experimental observations. In contrast, however, this study shows that the problem of long t_f, which anomalously increases with temperature is fundamentally caused by departure from diffusion controlled parabolic

migration of the liquid-solid interface with holding time during bonding due to a significant reduction in the solute concentration gradient in the base material.

Theoretical analyses showed it is possible to minimize t_f and prevent formation of stray-grains in joints between single crystal substrates by using a composite powder mixture of brazing alloy and base alloy as the interlayer material, which prior to the present work has been reported to be unsuitable. This was experimentally verified and the use of the composite powder mixture as interlayer material to reduce t_f and avoid stray-grain formation during TLP bonding of single crystal superalloys has been reported for the first time in this research. The newly developed numerical model is demonstrated to be applicable for studying TLP bonding behavior not only in Ni-base superalloys but also in a new generation structural intermetallic alloy and during joining of dissimilar base materials, enabled by the novel preclusion of symmetry assumption in the model. Overall, the application of composite powder mixture as the TLP bonding interlayer material for joining single crystal materials, shown possible by this research, has significant industrial appeal due to the fact that in addition to minimizing t_f, it reduces undesirable substrate erosion and enables the enrichment of the joint region with base material alloying elements.

ACKNOWLEGEMENTS

I would like to acknowledge my advisor, Dr. O.A. Ojo, for being generous with his time and for his valuable guidance throughout the project. I am also grateful to him for giving me the opportunity to contribute to knowledge and to put my passion for applied computational science into good use by investigating a relevant scientific problem and, in turn, producing industrially relevant innovative results.

I would also like to acknowledge my former advisor, Dr. J. Cahoon, who has been an inspiration and I had the great opportunity and privilege to work under him. I do not think I would be where I am today if he did not give me the opportunity in scientific research during my undergraduate work. It was at that time when I realized how much I enjoyed research and discovery. I would also like to thank Dr. Richards who has taught me many courses and I had the great privilege and opportunity to learn from him. Our discussions and his valuable advice over the years have been helpful in my understanding. I would also like to acknowledge Dr. Chaturvedi for allowing me to use his laboratory equipped with advanced materials characterization equipment.

I would like to thank my father and my mother for their love and support over the years. Most importantly, I thank God for giving me the energy and the capability to fulfill my work and for all the blessings bestowed upon me. Throughout my scientific journey, time and time again, I realize the perfection and intricate balance in all things created. This work is my testament to his glory and a humble offering to the exalted and grandest designer of all.

TABLE OF CONTENTS

LIST OF FIGURES

LIST OF TABLES

CHAPTER 1: INTRODUCTION

Gas turbine engines come in a wide variety of shapes, sizes and types and are extensively used in aircrafts and land-based power generators. The components of these engines operate under severe service conditions for prolonged exposure times. To cope with the harsh operating conditions, nickel (Ni)-base superalloys are extensively used in the manufacture of turbine engines due to their excellent elevated temperature strength and corrosion resistance [1]. In order to keep up with the ever increasing demand for better engine efficiency, both advanced processing techniques and alloy designs have been utilized to induce two major microstructural features in Ni-base superalloys: (i) a fewer number of grain boundaries and (ii) a higher stability and larger volume fraction of the γ' phase. The number of grain boundaries is reduced or altogether eliminated by resorting to directional solidification or to produce single crystal (SX) Ni-base superalloys. Higher operating temperature demands on jet engine components have led to an extensive use of SX superalloys in the aerospace industry over the past decade.

Nevertheless, as turbine efficiency increases, so does the geometric complexity of the engines, which in addition to the need to prevent freckle formation in large cast sections, often requires that engine components be made in smaller parts to be joined together by an appropriate bonding technique. Moreover, severe operating conditions often result in degradation of engine parts due to creep, fatigue, hot corrosion, foreign object damage and a combination of these factors. Economic necessity to reduce the life cycle cost of expensive SX components require the repair and refurbishment of service-damaged parts rather than complete replacement. Application of

conventional fusion welding techniques to SX Ni-base superalloys is severely restricted due to their extreme susceptibility to weld-cracking during welding and post weld heat treatment [2].Transient liquid phase (TLP) bonding, combines the benefits of liquid phase joining and diffusion bonding techniques, and has evolved as an attractive viable alternate joining method for difficult-to-weld superalloys.

In the TLP bonding process, an interlayer that contains a melting point depressant element such as boron (B), silicon (Si) or phosphorous (P), melts between two base metals that are to be joined. Subsequent to melting of the filler alloy, base metal dissolution occurs, which results in rapid displacement of the liquid-solid interface. The liquid phase rapidly attains equilibrium with the solid base metal and inter-diffusion of the alloying elements between the base metal and the liquid occurs resulting in an increase in the melting point of the interlayer liquid. Consequently, this results in isothermal solidification of the liquid. As isothermal solidification progresses, the liquid present at the joint decreases and the liquid-solid interface recedes to the center of the joint. If sufficient holding time is provided, complete isothermal solidification of the liquid and homogenization of the joint with the base metal could occur. However, residual liquid interlayer transforms into eutectic-type microconstituents at the joint centerline if the holding time is insufficient for complete isothermal solidification. These microconstituents are brittle in nature and have been found to reduce the mechanical properties of bonded materials [3].

An important parameter in the consideration of TLP bonding for commercial applications is the holding time (t_f) required to complete diffusional solidification, which is necessary to prevent the

formation of deleterious non-equilibrium solidification microconstituents. Generally, high temperature processing time t_f during the TLP bonding of SX superalloys is excessively long, which also can exhibit anomalous behavior by inversely increasing with bonding temperature [4]. This often limits the application of the technique since the desirable use of highly alloyed bonding fillers with a chemical composition comparable to the base SX alloy, but with associated high melting temperature, often requires high diffusion bonding temperature. Whilst this continues to constitute a key challenge, the cause of a long t_f at high temperatures and its inverse temperature dependence on SX materials had not been fully understood, which are imperative to the efficient optimization of the process to produce reliable joints. Therefore, the key objectives of the present research are:

1. to develop an appropriate numerical simulation model to study and understand the actual cause(s) of prolonged t_f that is required to produce reliable eutectic-free joint during TLP bonding of SX Ni-base superalloys and experimentally verify the theoretical predictions;
2. to use the newly developed numerical model and the acquired knowledge and understanding of the cause(s) of prolonged t_f to develop a viable procedure that will minimize t_f in SXs, thereby improving the effectiveness and efficiency of the joining technique.

To achieve these goals, a 2-D numerical simulation model, without the usual symmetry assumption, is developed to study the diffusion-controlled isothermal solidification process during TLP bonding of Ni-base materials, including the influence of grain boundaries on solidification kinetics. The computational model utilizes the following:

a) a fully implicit moving-mesh finite element method to calculate transient solute distribution and a direct interface-tracking technique to study the migration of liquid-solid interfaces; and

b) a cellular automata (CA) method to model and simulate the dissolution of additive gap-filler alloy powder particles by liquation of the brazing alloy during powder TLP bonding of SX materials.

Contrary to the assumption that an increased grain boundary diffusion coefficient would significantly accelerate the rate of liquid-solid interface migration, numerical calculations and experimental verifications showed that enhanced intergranular diffusivity has a minimal effect on the time required to achieve complete diffusion-induced solidification in cast superalloys. This indicates that the problem of a long t_f during high temperature TLP bonding of SX superalloys cannot be merely attributed to the absence of grain boundaries in these materials. Likewise, it was found and reported for the first time that, in contrast to suggestions in the literature based on analytical TLP bonding models, the general concept of competition between diffusivity and solubility of solutes cannot explain the anomalous reversed temperature dependence of t_f, where t_f increases with bonding temperature. Instead, careful numerical analyses coupled with experimental verification in this research show that the anomalous behavior and the problem of long t_f are caused by the departure of the propagating liquid-solid interface from parabolic displacement with holding time. Application of the numerical simulation model developed in this work coupled with the understandings provided by the study has resulted in a viable approach to minimizing t_f while preventing the deleterious formation of stray-grains during TLP bonding of SX superalloys. The method involves the use of a powder

mixture of brazing alloy and additive gap-filler powder, which had been generally assumed and previously reported to be unsuitable for SXs, due to the formation of stray-grains in bonded regions.

Furthermore, experimental study was performed to verify two pertinent issues (i) applicability of the new model to understand TLP bonding behavior in another type of new generation aerospace alloy, Ni_3Al-based intermetallic material and (ii) the use of the non-symmetry component of the new model to simulate and understand TLP bonding of dissimilar materials, for which no numerical model was found reported in the literature prior to the present work. The results show that the model is equally applicable to other types of high temperature materials and also suitably captures asymmetric diffusional solidification behaviors during TLP bonding of dissimilar materials. The use of a powder mixture of brazing and additive gap-filler alloys as the interlayer material for TLP bonding of SXs, not only minimizes $t_{f,}$ but also reduces undesirable erosion of base material liquid, and enables desirable enrichment of the joint with base-material alloying elements. Ultimately, the method will significantly enhance the commercial appeal of TLP bonding for industrial joining applications that involve components made of new generation SX heat resistant alloys.

CHAPTER 2: LITERATURE REVIEW

2.1 Ni-base Superalloys

The development of Ni-base superalloys has significantly contributed to advancements in aircrafts, rockets, and land-based power generation turbine engines, where performance under high operating temperatures and highly corrosive environments is required. Ni-base materials exhibit high melting temperatures, high tensile strength, high creep rupture strength, and excellent corrosion and oxidation resistance [2]. Furthermore, Ni is stable in face-centered-cubic (FCC) crystal structures from room temperature to its melting point. As a result, there are no phase transformations that cause significant expansions and contractions that would complicate their use in high temperature applications. Additionally, Ni-base superalloys generally exhibit reliable microstructural stability at elevated temperatures. Other high temperature materials include Co-alloys, which exhibit hexagonally-closed-packed (HCP) crystal structure and tend to be more expensive than Ni-base superalloys [5].

Generally, Ni-base superalloys contain up to ten different alloying elements, including chromium (Cr), cobalt (Co), rhenium (Re), tungsten (W), tantalum (Ta), molybdenum (Mo), niobium (Nb), aluminum (Al) and titanium (Ti) and minor additions of boron, zirconium and carbon [6]. The main phases that are present in Ni-base superalloys are briefly discussed as follows:

Gamma (γ) Matrix:

The γ matrix is an FCC Ni-base austenitic phase that normally contains substitutional solid solution alloying elements like Co, Cr, Al, Ti, etc. Common solid solution elements in the γ phase include Co, Fe, Cr, Mo, W [7]. These elements have atomic radii that are not very different from that of Ni and as a result tend to stabilize the austenitic phase γ at high temperatures. The γ matrix gains some of its strength by solid solution strengthening which can be related to the increase in resistance to dislocation motion due to induced lattice distortion caused by the difference in atomic size between Ni and the alloying solute atoms. At temperatures $T > 0.6\ T_m$, the strengthening of the γ phase becomes diffusion dependent and the slow diffusing elements Mo and W contribute the most as hardeners [5]. The γ matrix acts as the medium for the dispersion of second phase particles that contribute to the properties of the material.

Gamma prime (γ'), Gamma Double Prime (γ'') and Delta (δ) Phases:

Elements such as Al, Ti, Nb and Ta have a larger atomic radii than Ni and as a result, promote the formation of ordered phases such as Ni_3(Al, Ta, Ti) γ' phase (Figure 2.1), which is the primary strengthening phase in Ni-base superalloys. A close match exists between the lattice parameters of the γ matrix and γ', which enables the γ' phase to homogeneously precipitate within the γ matrix and be stable at high temperatures [5]. Factors that can contribute to the hardening produced by the γ' phase include γ' fault energy, coherency strains, volume fraction of γ' and particle size. Small γ' precipitates usually exist in a spherical shape to reduce surface energy. As the precipitates grow, the morphology can change to cubes or plates depending on the matrix/precipitate lattice mismatch [5].

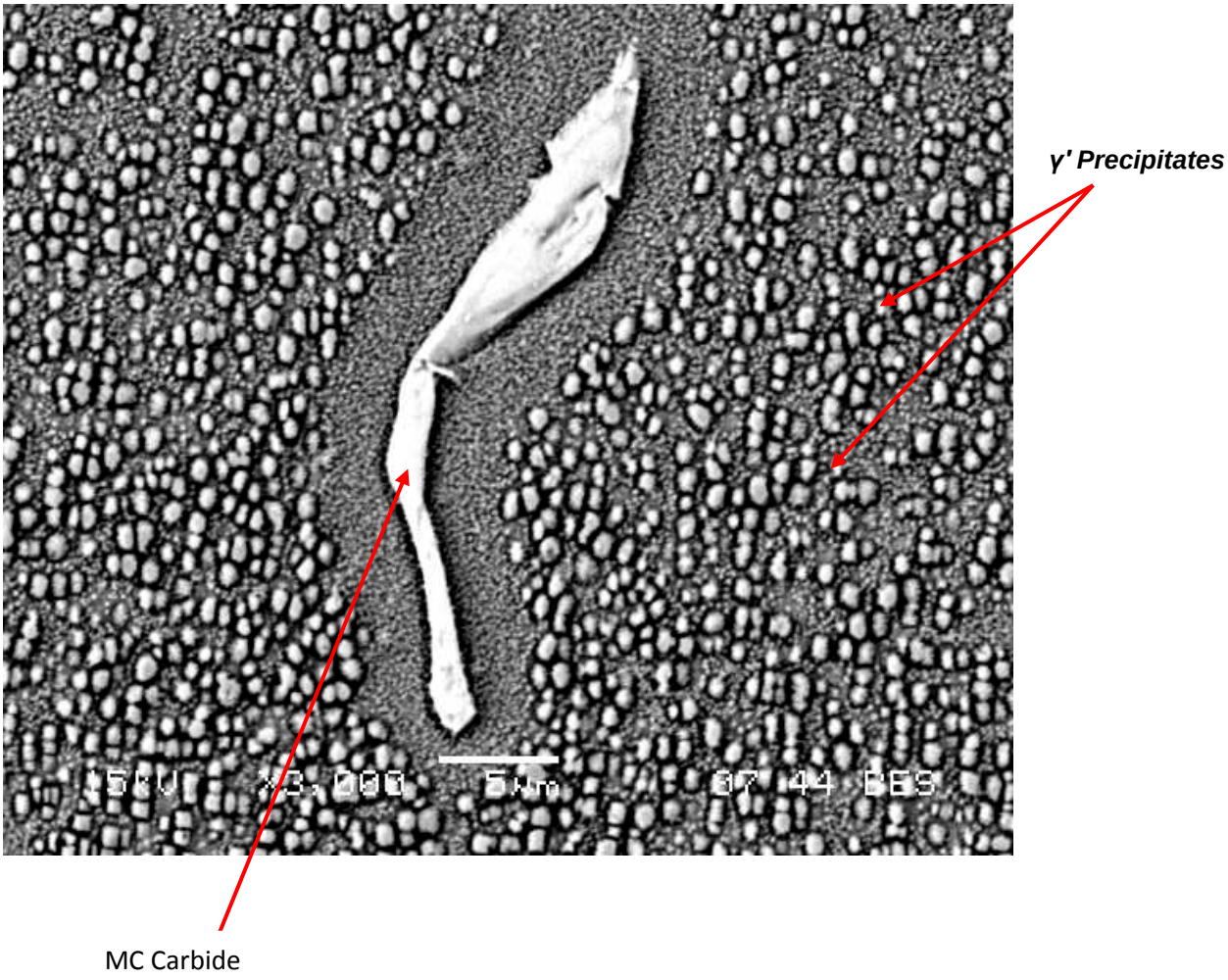

Figure 2.1: Scanning Electron Microscopy (SEM) micrograph of IN738 showing MC carbides, γ matrix and γ' precipitates

Ni-base superalloys rich in Fe and Nb tend to form a related secondary phase, γ" phase. Precipitates of this phase exhibit body-centered-tetragonal structure and display a disc-shaped morphology with thickness as small as 10 nm, diameter of about 50 nm and are generally found to be coherent with the matrix. Ni-iron alloys that contain γ" precipitates are susceptible to the formation of an orthorhombic δ phase in over aged conditions [6] which are incoherent with the γ matrix and as a result do not confer strength.

MC Carbides:

Alloying elements including Cr, Mo, W, Nb, Ta and Ti react with carbon in Ni-base superalloys to form primary MC carbides and secondary $M_{23}C_6$ and M_6C carbides, where M stands for the metallic alloying elements [6]. In many alloys, MC carbides precipitate at high temperatures from the liquid phase during ingot casting. As a result, they are often found in the interdendritic regions in cast alloys with no distinct orientation relationship with the γ matrix, which results in blocky and script morphologies [5]. Their formation has been attributed to the breakdown of MC carbides via the reaction:

$MC + \gamma \rightarrow M_{23}C_6 + \gamma'$

There is some disagreement on whether carbides are detrimental or beneficial to superalloy properties. In polycrystalline superalloys, intergranular $M_{23}C_6$ carbides contribute to strengthening by pinning down and inhibiting grain boundary sliding at elevated temperatures. The effects of carbon addition on properties of polycrystalline nickel-based superalloys have been studied by Chen and Knowles [8]. They reported that carbon addition up to 0.09 wt % contributed to improved creep rupture life from 10 to 100 hours, due to the formation of fine coherent intergranular $M_{23}C_6$ carbides.

Topologically Close-Packed Phases:

It has been reported [9] that excessive concentrations of Cr, Mo, W and Re, promote the precipitation of intermetallic phases that have atomic packing density with complex crystal structure and normally refered to as topologically closed-packed (TCP) phases. Particles of these phases usually exhibit plate-like morphologies and have been found to be potentially damaging to mechanical properties of superalloys since they can act as crack initiators due to their brittle nature and they can tie up essential γ and γ' strengthening elements [6]. Generally speaking, TCP phases such as μ, σ, P and R phases have the formula A_xB_y where A and B are transition elements. The μ phase is based on the stoichiometry A_6B_7 and has a rhombohedral crystal structure with 13 atoms per unit cell. The σ phase is based on the stoichiometry A_2B and it has a tetragonal crystal structure with 30 atoms per unit cell. The P phase has a primitive orthorhombic crystal structure with 56 atoms per unit cell. Finally, the R phase has a rhombohedral crystal structure with 53 atoms per unit cell [5].

2.2 Single Crystal Ni-base Superalloys

When Ni-base superalloys were first developed in the 1940's they exhibited equiaxed polycrystalline (multi-grained) microstructure. Advancements in materials and processing have now resulted in the development of SX Ni-base superalloys with significantly improved high temperature properties compared to conventional polycrystalline materials, achieved through directional solidification casting techniques. During directional solidification processes, columnar grains are formed parallel to the growth axis, which normally occurs along the <100> crystallographic direction in Ni-base superalloys [10].

The elimination of grain boundary strengtheners such as C, B and Si increases the melting temperature of SX materials and lowers the elastic modulus associated with the <100> directions, which enhances the thermo-mechanical fatigue resistance in areas of constrained thermal expansions [5]. The elimination of grain boundaries also results in better corrosion resistance since grain boundaries are usually more susceptible to corrosion. To study the effect of removing grain boundaries on creep performance, an experiment was performed on a CMSX-4 superalloy with and without grain boundaries [5]. The data indicated that for an applied stress of 300 MPa at 850 ^{o}C, an SX had a stress rapture life of 10,000 hrs while the presence of grain boundaries resulted in creep life reduction to 100 hrs. In another related study, it was reported that under a creep load of about 200 MPa at 980 ^{o}C, the removal of transverse grain boundaries increased the creep ductility from below 5% to over 25% [11].

It has become common practice to manufacture SX components, such as turbine blades, by investment casting techniques. There are several different manufacturing methods used in practice to create SX turbine blades all of which use the principles of directional solidification. A common method is the Bridgeman technique where the melt is placed inside a furnace and a temperature gradient is induced such that solidification is obtained in one direction due to constitutional undercooling. As the liquid-solid interface advances, a varying solute concentration ahead of the liquid-solid interface changes the equilibrium solidification temperature. At this point, the temperature of the liquid is lower than the equilibrium solidification temperature causing an undercooling effect, where heat is transferred from the solid to the liquid, promoting dendritic growth. To remove grain boundaries a grain selector at

the bottom of the mould is used to achieve dendritic growth into a single grain microstructure [5].

2.3 Joining Techniques for Single Crystal and Polycrystalline Nickel-Base Superalloys

Ni-base superalloys experience service degradation due to severe and prolonged operating conditions. Due to the specialized methods used to manufacture these materials they are normally very expensive and complete replacement of defective parts may not be economical. Repair and refurbishment of service-damaged superalloy components are, therefore, more desirable over complete replacement. As a result, a great deal of research has been directed towards developing appropriate and reliable techniques to join and repair parts made of Ni-base superalloys. The common traditional joining and repair methods for structural engineering materials include fusion welding and diffusion brazing, which are discussed next.

2.3.1 Fusion welding

Fusion welding involves the joining of two mating surfaces by controlled melting through localized heating and subsequent cooling of the liquid metal. Welding is usually done such that the base material is at or near room temperature which results in significant temperature gradients between the weld pool and the base material [12]. Major types of fusion

welding processes include gas, arc, and high-energy beam welding. Gas welding produces the highest heat input and lowest power density among the various welding processes. High heat input increases damage to the work piece while high energy beam welding, with the lowest heat input, increases penetration and the general quality of the welds. Joints that require multiple-pass arc welding can be welded in a single pass by electron beam welding at high speeds with narrow heat-affected zones (HAZ) and little distortion [12]. The equipment required for electron beam welding, however, is very expensive and the associated x-ray shielding can be inconvenient and time consuming.

Fusion welding is generally used to join some superalloy materials but its application to Ni-base superalloys that contain significant amount of Ti and Al is, however, limited. This is due to the high susceptibility of these materials to HAZ cracking during welding and subsequent heat treatment. Rapid heating and cooling generates grain boundary liquation and thermally-induced stresses that result in intergranular micro fissuring [13]. During post weld heat treatment, the presence of welding residual stresses coupled with aging contraction stress could cause further cracking depending on the metallurgical state of the superalloy [14]. Additionally, physical distortion of components can occur during welding due to the localized nature of the concentrated heat source involved in the process. Fusion welding is generally problematic in joining dissimilar materials [12]. In Ni-base superalloys, it has been found that the weldability problem worsens with an increase in concentrations of γ' forming elements [15].

2.3.2 Brazing

Brazing is extensively used in the aerospace industry due to its ability to join difficult- to-weld Ni-base superalloys. Conventional brazing is a joining technique that involves the joining of two metal surfaces by the use of a filler metal and heating to temperatures above 425 ^{o}C. The filler metal melts at the brazing temperature and the resultant liquid is held within the joint by surface tension. Metallurgical reactions between the liquid and the substrate results in the formation of joints upon cooling. Due to the short holding time associated with conventional brazing, the limited extent of solid state diffusion of solute elements is possible [12]. Some brazing processes such as diffusion brazing involve much longer holding times so that significant diffusion of elements can take place.

Effective capillary joining during brazing requires the efficient transfer of heat from the heat source into the joint. The size of individual assemblies, numbers required, and the rate of production influence the type of heating method used in brazing. Consideration of the rate of heating, thermal gradients and cooling rate is also important when choosing a heating method, since these factors significantly vary with different heating methods. The most common methods of heating include torch, furnace, induction and resistance brazing.

Manual torch brazing is most frequently used for repairs with short production runs as an alternative to fusion welding. Heating of the assembly is achieved by using a gas (oxyfuel) as the heat source and a flux material is usually used to promote wetting of the filler metal [16]. Furnace brazing is a high volume production process for self-fixture assemblies with pre-placed filler metal. The furnace is usually purged with a gaseous

atmosphere or evacuated of air and heated to a temperature above the liquidus of the filler metal but less than the melting point of the base metal. Pre-placed filler metal can be in the form of wire, foil, powder, paste, slugs or preformed shapes [16]. Induction brazing employs material's resistance to the flow of electricity induced by coils around a work piece to provide the heat required for brazing. The process relies on a high-frequency alternating current that flows through the induction coils to create electromagnetic fields around the work piece. The opposing currents that are induced into the work piece generate the heat required for brazing. Some advantages of the process include selective heating of the work piece and quick attainment to brazing temperature. Induction brazing is also well suited for high-volume production applications that can be remotely controlled. High-strength components can be induction brazed with little loss of strength because of the precise heating capabilities of the process [16]. In dip brazing, the assembly is immersed into a heated bath of either molten metal or a flux bath of molten salt. The dipping technique is used to manufacture electronics and similar very small components. The parts to be joined are held together and immersed into a bath of molten metal that flows into the joints for brazing [16]. Resistance brazing is most applicable to relatively simple joints in metals that have high electrical conductivity. In resistance brazing, the work piece has pre-placed filler, is part of the electric circuit. Brazing heat comes from either placing carbon electrodes in contact with the brazement to conduct heat into the work or by relying on the resistance of the brazement to generate heat [16].

Brazing filler alloys usually contain melting point depressant (MPD) elements such as B, Si, or P, which are added to depress their melting temperature. Other elements such as C, Ti

and Al are deliberately excluded from filler alloys due to their tendency to form undesirable stable phases that can embrittle the joint. It is necessary for brazing to be conducted under a protective atmosphere, including vacuumed environments to prevent the joint from coming into contact with volatile contaminants and the formation of oxides. Brazing in chemically inert gas atmospheres such as nitrogen, argon or helium prevent oxygen and other gaseous elements that might react with the components to form surface films and inhibit the flowing and wetting of the liquated interlayer [17]. A hydrogen-type atmosphere has been used in the past due to its ability to dissociate oxides developed at high temperatures during bonding. Its effectiveness is, however, reduced if employed on Ti and Al containing alloys such as Ni-base superalloys. Controlled gas atmospheres require a confining vessel which enables the incorporation of a heating furnace. This can reduce post-processing operations such as cleaning and removal of flux residues.

Some potential disadvantages of using a gaseous atmosphere for joining include the high capital costs of the equipment, including the handling of associated gas atmosphere or vacuum system, and the recurring costs due to consumption of gas atmospheres used to procedss and maintain the vacuum pumps. Additionally, certain metals may not be compatible with standard atmospheres. Hydrogen atmospheres can cause hydrogen embrittlement of some metals including Ti, Zr and Ta. Likewise, nitrogen atmospheres cannot be used when the parent materials and filler metals contain elements susceptible to nitriding such as molybdenum, titanium and zirconium [16]. Inert atmospheres such as argon and helium may also be employed by performing multiple inert gas purging prior to furnace brazing [17]. Brazing conducted in a high vacuum atmosphere can reduce the formation of

oxide layers on filler-substrate mating surfaces.

Surface preparation is of paramount importance for the production of good quality joints. Any residual oxide films, grease or oils may inhibit the initiation of spreading and wetting of the liquid filler after melting. The influence of low surface energy non-wettable interlayer oxides on liquid surface energies has practical importance. Oxides entrapped at the liquid/solid interface may also act as a diffusion barrier. A good brazing surface requires sufficient surface roughness and good wettability by the filler alloy. Low viscosity and good flow are also important qualities that help to improve the quality of brazement [17]. Mechanical cleaning that involves grit blasting, grinding and brushing, all of which slightly roughens the surface, is sometimes necessary and usually used when there are large amount of surface oxides. Traces of oil or grease may be removed by chemical cleaning methods which involve the use of degreasing solutions. Spraying, soaking, and suspension in hot vapor are some of the general techniques used during chemical cleaning. Chemically cleaned components can subsequently be ultrasonically cleaned in alcohol to ensure the complete removal of all traces of degreasing solutions. Fluoride cleaning is another method of surface cleaning employed to effectively remove oxide layers on thermal fatigue cracks and other narrow hard-to-reach cracks. Cleaning is done by exposure to fluoride ions in a reducing atmosphere but proper control of the process is important to ensure adequate cleaning of deep narrow cracks and avoid excessive surface depletion [17].

Generally, brazing is done by using a flux. The primary purpose of brazing fluxes is to promote the wetting of the base material by the liquid filler metal. Fluxes must be capable of dissolving any oxide that remain on the base metal after it had been cleaned and oxide

films on the filler metal. In some instances, fluxes may serve to suppress the volatization of high-vapor-pressure constituents in a filler metal [16]. Fluxes need to be applied as an even coating and must completely cover and protect the surfaces until the brazing temperature is reached. Viscosity and interfacial energy between the flux and mating surfaces are important for good wetting and it is recommended that fluxes should be used in their proper temperature ranges and on the materials for which they are designed for. Many chemical compounds are used in the preparation of fluxes. The most common ingredients of chemical fluxes include [16] borates (sodium, potassium, lithium, etc.), fused borax, elemental boron, fluoborates (potassium, sodium, etc.), fluorides (sodium, potassium. etc.), chlorides and alkalis (potassium hydroxide, sodium hydroxide). Certain filler metals contain alloy additions of deoxidizers, such as phosphorous, lithium, and other elements that have strong affinities for oxygen. In some instances, these additions make the filler metal self-fluxing without the application of prepared fluxes or controlled atmospheres. Such fillers are self-fluxing only in the molten state and will oxidize during the heating cycle [16]. Therefore, the use of protective atmospheres or fluxes in conjunction with these fillers is usually preferred.

Brazing has many distinct advantages. It can be used to economically fabricate complex and multi-component assemblies. It exhibits excellent stress distribution and heat transfer properties. It can also be used to join non-metals to metals or metals that vary widely in size. Additionally, strong, uniform and leak proof joints can be rapidly and inexpensively made. Complicated assemblies that are made of thick and thin sections, in odd shapes, and differing wrought and cast alloys can be successfully brazed. Closer tolerances can be met by using brazing than fusion welding due to the much lower amount of base

metal melting [17]. Brazing, however, has the limitation of producing a joint with physical and mechanical properties that are inferior to the base metal due to the presence of intermetallic phases at the brazed joint.

2.3.3 Transient Liquid Phase (TLP) Bonding

Transient liquid phase (TLP) bonding evolved from brazing to address the problem of brittle intermetallic formation in brazement. TLP bonding is a high temperature fluxless process that combines the beneficial features of liquid phase joining and solid- state diffusion bonding. It has been used to produce high strength joints in difficult-to- weld heat resistant alloys. Fundamentally, the process involves no plastic deformation of the components being joined, although some pressure may be needed to ensure that mating surfaces are in intimate contact [16]. The process involves the use of an interlayer material (filler alloy) that contains a melting point depressant (MPD) element(s) such as B, Si and P. At a joining temperature below the solidus temperature of the base metal, the interlayer melts and interdiffusion of alloying elements occurs between the substrate and the liquated interlayer. This results in changes in the composition of the solid and the liquid phases until equilibrium is established at the joint's interface. Further diffusion of the MPD into the base metal raises the melting point of the liquid, which results in its isothermal solidification. Complete isothermal solidification can be achieved if sufficient holding time at the joining temperature is provided before cooling to the ambient temperature. A longer holding time, after achieving complete isothermal solidification, may also be necessary to homogenize both the microstructure and the composition of the bonded materials.

In contrast to brazing, TLP bonding is more suitable for joining components intended for demanding high temperature service. The microstructure and mechanical properties of the TLP bonded joint are close to those of the base material. Dissimilar base alloys with complex shapes and varying thicknesses can also be joined by TLP bonding and mass production can be employed which can significantly reduce production costs [18]. Due to the solid state diffusion that must occur during TLP bonding, a long holding time may be required to achieve complete isothermal solidification, which somewhat limits the use of the process commercially. An incomplete isothermal solidification results in the formation of eutectic-type microconstituents at the joint, which are brittle and provide an easy path for crack initiation and propagation. Precipitation of second phase particles within the joint- substrate interface due to the diffusion of the MPD into the base material may also have detrimental effects on the mechanical properties of the bonded materials. Improper or inadequate surface preparation or poor bonding atmosphere can also result in a poorly joined part or filler spillage upon melting, similar to the case during brazing.

2.3.3.1 Surface Preparation

Surface preparation is also very important for the production of good quality TLP joints. Any surface oxide films, grease or oils may inhibit the initiation of wetting and spreading of liquid filler after melting. The influence of low surface energy non-wettable interlayer oxides on liquid surface energies is of practical importance. Oxides entrapped at the liquid/solid interface may also act as a diffusion barrier. A good brazing surface requires sufficient surface roughness and good wettability by the filler alloy. Low viscosity and

good flow are also important qualities that help to improve the quality of the joint [17].

2.3.3.2 Interlayer (Filler) Alloys

Suitability of a filler alloy for use in TLP bonding depends on some important criteria. The liquidus temperature of the alloy must be less than the solidus temperature of the base material. Proper fluidity of the liquid filler at the brazing temperature is necessary to ensure wetting and flow over base material surfaces [19]. Filler alloys are available in various forms such as amorphous foil, tape, powder/paste, and rapidly solidified sheets. Foils are usually made by rapid solidification during melt spinning operations, while powdered forms are usually produced by gas atomization. The powders may be mixed with plasticizers or organic cements to facilitate their positioning on the base metal surface. Tape forms are usually made up of powders that are uniformly applied to a flexible organic backing strip. In some instances organic binders tend to burn during brazing, which causes voids at the joint. Cored fillers are another type of fillers where the base material, such as pure Ni, is surrounded by a surface rich in MPD elements produced by diffusion treatment. Some elements such as chromium are often added to Ni-base filler alloys to increase the oxidation and corrosion resistance of the resulting joint [20].

Factors that affect the kinetics of TLP bonding and the time required to achieve complete isothermal solidification include:

- *type of MPD solute.* Generally, fillers with MPD solute that has high solubility and diffusivity in the base material are most desirable to minimize the time required to achieve complete isothermal solidification. Some commercial fillers also have more

than one MPD solutes present in the same alloy. For example, Si, which has high solubility in Ni, can be coupled with B, which has high diffusivity in Ni, to bond Ni-based materials;

- *initial thickness of the filler alloy*. Generally, the amount of liquation of the base material increases as the thickness of the filler alloy increases. As a result, longer processing time is required in order to achieve complete isothermal solidification.

2.3.3.3 Base Material Characteristics

TLP bonding can be used to join SXs or polycrystalline materials as well as dissimilar materials including metals-ceramics. Certain characteristics of the base material must be met to achieve optimum joint microstructure and properties and these include:

- *type of base material*. The base material must be able to sufficiently accommodate the MPD solute. The base material may or may not have an initial concentration of the MPD already present. If it does, then the amount of solute from the filler material that can be accommodated may be reduced, which may prolong the time required to achieve complete isothermal solidification;

- *thermal properties of the base material*. It is necessary that the base material has sufficient strength and thermodynamic stability at the bonding temperature. Also a significantly higher base material solidus temperature compared to the liquidus temperature of the filler is paramount in order to prevent undesirable incipient melting in the substrate during joining;

- *microstructural properties of the base material.* Another important factor is the propensity of the substrate form second phase precipitates with the base material region adjacent to the substrate-joint interface. It has been noted that a high density of these precipitates degrades mechanical and corrosion resistance properties of bonded materials [20]. In some cases, post processing thermal treatment may be used to dissolve the second phase particles in order to prevent their damaging effects.

2.3.3.4 Wide Gap TLP Bonding

An interlayer material in the form of a powder mixture can be used in situations where the foil form is not adequate, such as for the repair of cracks or surface erosion on Ni-base turbine parts. The interlayer powder mixture generally consists of a filler alloy powder that contains MPD solute and a powder additive with comparable chemical composition to the base material and which normally has a higher melting temperature than the bonding temperature. Upon melting of the low melting temperature powder, the undissolved additive powder particles could acts as a sink for the diffusion of the solute, which may result in reduced time to achieve complete isothermal solidification. Optimization of the process parameters is essential in obtaining a superior joint [20]. Depending on the temperature and type of additive powder, melting of the additive particles can occur and the un-melted remaining solid components can be saturated with solute. Huang et. al. [21], investigated the diffusion bonding of Al-based dissimilar composites by using Al-Si, Al-Cu and Al-Si-SiC powders as fillers. They reported that the segregation of SiC particles and formation of porous zones at the joint lead to a reduction of in the joint shear strength. They also reported an increase in the shear strength of

the joint with increasing temperature and holding time. Wu et. al. [22] also investigated wide gap bonding of stainless steel to Ni-base superalloy. They reported that during the bonding process, the additive particles reacted with the liquid by dissolution but remain largely unmelted and provided the necessary capillary force to retain the molten filler material, which would otherwise be overly fluid to bridge the gap faying surfaces. They also reported that the strength and elongation of the brazed joint increase with increasing bonding temperature. If the bonding temperature is not high enough, unfilled spaces between unmelted additive powder particles could result in a porous joint. Zhuang and Eager [23] experimented with powder TLP bonding by using metallic powders coated with a small amount of material that contained an MPD solute. They reported that the coating material and the thickness of the deposit influence porosity formation within the joint. Two different powder materials, Ni-20Cr and 304L stainless steel, both of which were coated with Ni-10P, to join 304L stainless steel base alloy. They reported joints with good mechanical properties when the Ni-20Cr powder was used, while inferior properties are obtained by using the 304L powder, which was attributed to residual porosity observed within the joint. To reduce porosity, they proposed a liquid infiltration approach where a thin foil that contained an MPD solute is inserted between the base material and the powder mixture. Although wide gap TLP bonding is a versatile technique to bond non-weldable materials, it has been reported that the method is unsuitable to bond SX base materials due to formation of stray grains in the joint region, which compromises the properties of bonded materials.

2.4 Mechanisms of TLP Bonding

It is generally assumed during TLP bonding that after the melting of the filler material, the solid substrate and the liquid insert rapidly equilibrate to their respective solidus and liquidus compositions at the bonding temperature. Solid-state diffusion of the MPD in the base alloy follows the equilibration and results in gradual isothermal solidification of the liquated interlayer. Duvall et. al. [3] defined the three stages of TLP bonding as:

1) base metal dissolution,

2) isothermal solidification of the liquid interlayer, and

3) homogenization of bonded material.

Tuah-Poku et. al. [24] introduced a fourth stage, namely, the homogenization of the liquid after base metal dissolution. An initial stage prior to base metal dissolution (stage 0) was added by MacDonald and Eager [25] to account for the heating time from room temperature to just before the onset of liquation of the filler. This is due to the possible loss of solute during the heating of the joint, which was also reported by Niemann et al. [26]. They noticed that at slow heating rates insufficient liquid forms at the interface due to premature diffusion of MPD solute into the base material. Zhou et. al. [27] re-classified TLP bonding into four stages: i) heating stage, ii) dissolution and widening which is subdivided into two stages; (a) heating from the melting point to bonding temperature, and (b) isothermal dissolution at the bonding temperature, iii) isothermal solidification and iv) homogenization.

2.4.1 Initial TLP Bonding Conditions

A binary eutectic diagram shown in Figure 2.2, with A as the base material and B as the MPD solute, can be used to explain the TLP bonding process. Important initial bonding parameters can be summarized as follows (Figure 2.3):

- *initial concentration of the MPD solute in the interlayer (filler alloy),* $C_{F.}$ Commercial filler alloys have a solute concentration that is usually higher than the liquidus composition of the base alloy at the bonding temperature.

- *initial concentration of the MPD solute in the base material,* C_m . The base material may be completely free of the MPD solute prior to joining or in some cases, could contain unintentional or intentional small amounts of MPD solutes (Figure 2.4).

- *bonding temperature,* $T_{bonding}$. The bonding temperature is usually higher than the melting temperature of the interlayer alloy but lower than the melting temperature of the base material. The selection of bonding temperature affects the diffusivity of

  the MPD solute in the liquid and solid and equilibrium solidus and liquidus concentrations at the liquid-solid interface; and

- *initial thickness of the interlayer alloy,* W_o . Commercially, interlayer foils can vary in thickness from 25 µm - 150 µm. Thicker alloys result in increased base alloy dissolution and longer isothermal solidification time.

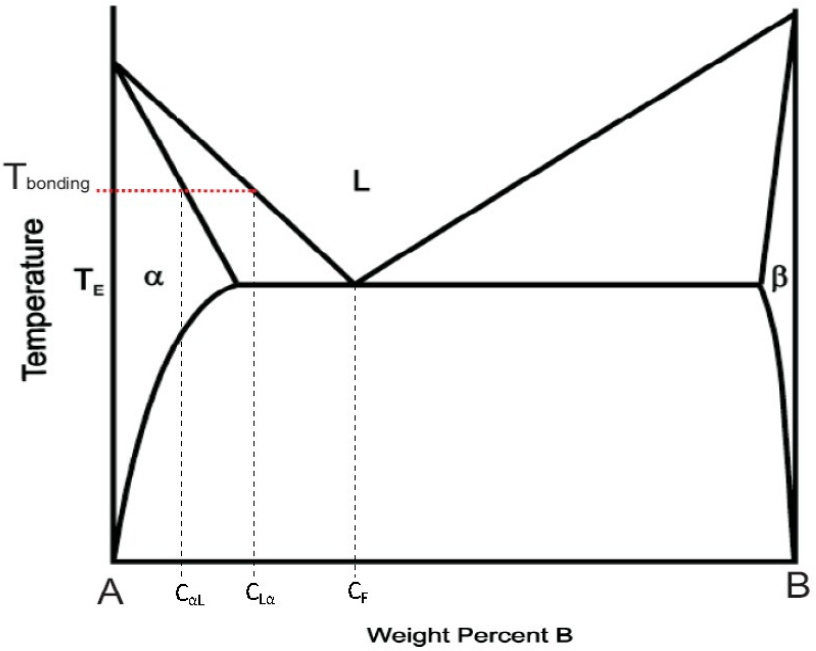

Figure 2.2: Binary eutectic phase diagram

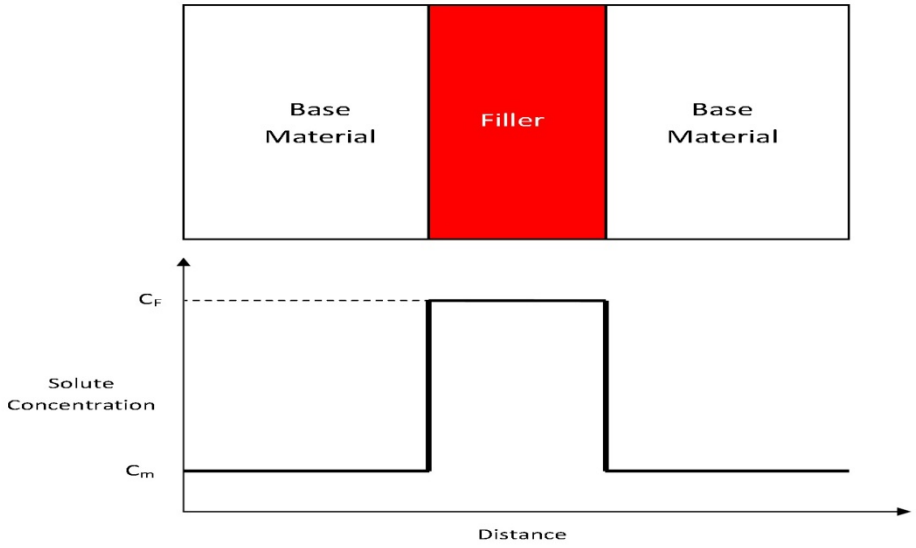

Figure 2.3: Initial conditions of TLP bonding

2.4.2 Heating and Melting of Filler Alloy

During the heating stage, the TLP bonding assembly is heated up from room temperature to a temperature above the melting point of the filler. Prior to reaching the melting temperature of the filler, some solid-state diffusion between the filler alloy and the base metal may occur. The extent of diffusion will depend on several factors including the eutectic temperature, heating rate and diffusivity of the MPD solute. Very slow heating rates may result in severe solute depletion in the filler, which may result in lower solute concentration relative to the solidus composition at the bonding temperature. As a result, no liquid will form upon reaching the joining temperature. This problem becomes most severe with very thin filler alloys and low solute concentrations [26]. Upon melting, the filler wets the solid substrate and flows throughout the joint. Wettability depends on the liquid-solid surface energy and the viscosity of the liquid phase.

2.4.3 Base Material Dissolution

Initially, upon melting of the filler material, the amount of solute at the liquated joint is generally higher than the solidus and liquidus compositions required to achieve equilibrium at the bonding temperature. Therefore, to attain equilibrium at the solid-liquid interface, the base alloy melts-back into the liquid, which results in an increase in the volume of the liquid interlayer. The interfacial reactions are rapid and controlled by liquid phase diffusion. Base metal dissolution occurs after liquation of the filler alloy and progresses during further heating above the melting temperature of the filler alloy. The maximum width of the liquid at the joint represents the maximum dissolution width W_{max}, which is attained some time after

reaching the bonding temperature $T_{Bonding}$ and the solute concentrations in the solid and liquid at the interface are the same as the equilibrium solidus and liquidus concentrations $C_{\alpha L}$ and $C_{L\alpha}$, respectively, as illustrated in Figure 2.4. The dissolution stage is important in aerospace applications such as thin honeycomb structures, rocket fins and thin foil structures where large base metal dissolution can lower the load bearing capability of thin sections. The extent of base metal dissolution depends on many factors including the initial concentration of MPD solute in the filler C_F, initial filler thickness and solubility of the MPD solute in the base material.

Several authors have suggested various analytical models to explore base material dissolution. Nakao et al. [28] analyzed base metal dissolution based on the Nernst-Brunner theory and formulated the equation shown below:

$$\frac{dC}{dt} = K\left(\frac{A}{V}\right)\left(C_s - C_t\right) \tag{2.4.1}$$

where C_s is the solute concentration at the saturated state; C_t is the solute concentration at spontaneous time t; K is the dissolution rate constant. A is the surface area of the solid and V is the volume of the liquid. C_s and C_t can be calculated as shown in the following Equations 2.4.2 and 2.4.3:

$$C_s = \left[\frac{ph}{x_s + ph}\right]C_F \tag{2.4.2}$$

$$C_l = \left[\frac{ph}{x + ph}\right]C_F \tag{2.4.3}$$

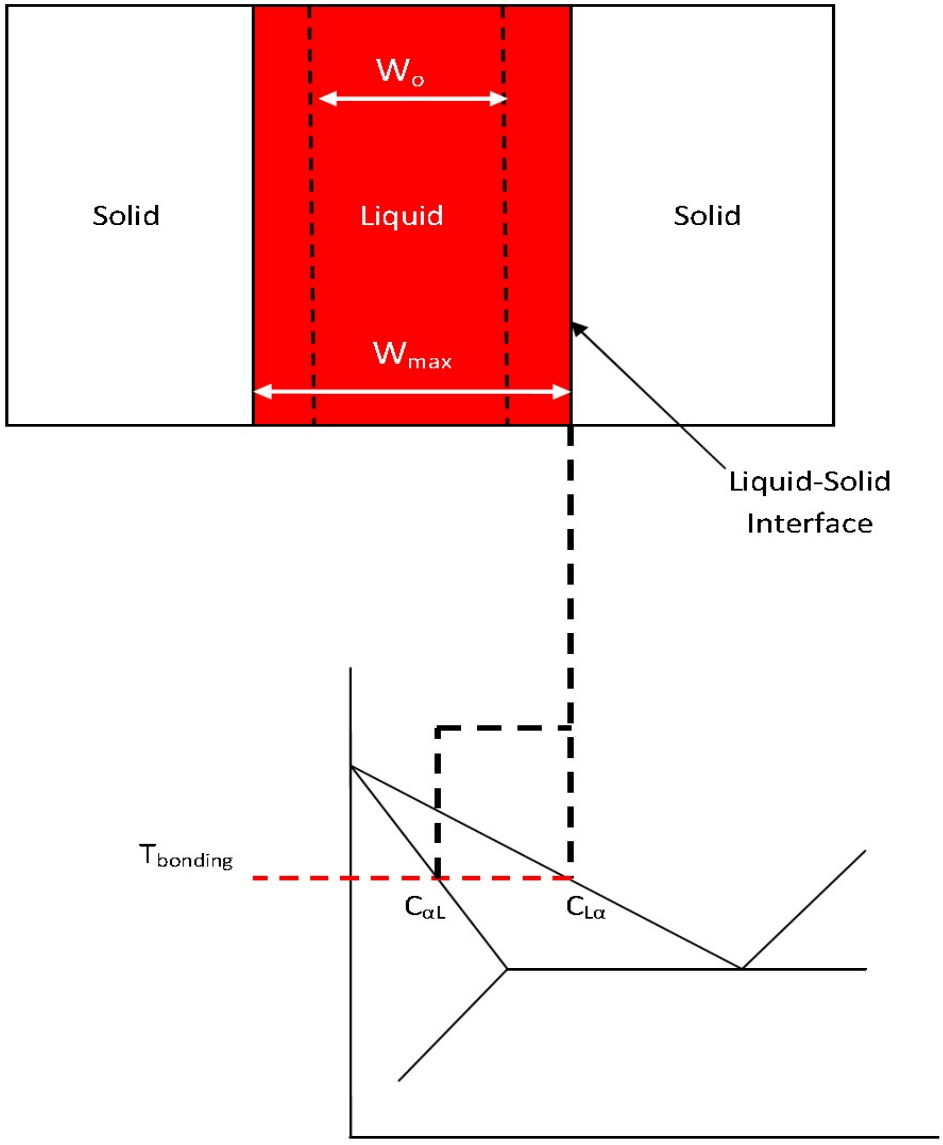

Figure 2.4: Base material dissolution during TLP bonding

where C_F is the initial concentration of the MPD solute in the liquid interlayer; p is the ratio ρ_l/ρ_s where ρ_l is the density of the liquid filler and ρ_s is the density of the base metal; h is half of the initial thickness of the filler; x is the instantaneous dissolution width and x_s is the maximum dissolution width at the saturated state. A dissolution parameter P was expressed as follows:

$$P = Kt = h\left\{\ln\frac{x_s(x+ph)}{ph(x_s-x)}\right\} \tag{2.4.4}$$

Nakao et al. [29] reported a linear relationship between the dissolution parameter P and the holding time. The dissolution time was found to be in the order of seconds or few minutes and did not play a significant role in the total time required for TLP bonding, which is usually in hours. Nakao et al. [28] assumed in their model that the liquid and adjacent solid have compositions fixed by the respective liquidus and solidus values before and after equilibration. In order to improve the analysis, Gale et al. [30] used Equation 2.4.5, where the concentration of the MPD solute in the base alloy can be obtained as a function of the holding time.

$$C(x,t) = 0.5C_o\left[\frac{erf\,(h-x)}{2\sqrt{Dt}}\right] + \frac{erf\,(h-x)}{2\sqrt{Dt}} \tag{2.4.5}$$

where C(x,t) is the concentration of the solute as a function of distance from the center of the interlayer (x) and time (t); 2h is the width of the interlayer; D is the diffusivity of the solute in the substrate and C_O is the initial solute concentration in the filler. They assumed that the MPD solute diffuses out of a finite liquid interlayer into a semi-infinite solid substrate during the base material dissolution stage, and the diffusivity of the solute is that observed in

the solid substrate by ignoring its greater diffusivity in the liquid. This results in the flattening of the concentration profile in the liquid, which influences diffusion in the solid substrate.

2.4.4 Isothermal Solidification Stage

Isothermal solidification is normally assumed to commence after the dissolution stage and proceeds at a constant bonding temperature during which the MPD solute diffuses into the base material across the liquid-solid interface. Local equilibrium is maintained at the solid-liquid interface throughout the isothermal solidification process and the compositions of the liquid and the adjacent solid remain fixed at $C_{\alpha L}$ and $C_{L\alpha}$, respectively. A decrease in the amount of liquid that can be maintained at a constant temperature due to the loss of the MPD solute causes isothermal solidification to occur by migration of the liquid-solid interface towards the centerline of the joint as illustrated in Figures 2.5 and 2.6.

If the holding time is sufficient, the liquid can be entirely removed, which results in complete isothermal solidification (Figure 2.7). The isothermal solidification stage is much slower than the dissolution stage since it is controlled by solid-state diffusion of the MPD solute in the base metal. The time required to complete the isothermal solidification process is system specific because it depends on the diffusion flux of the solute in the base metal and the amount of solute that must be diffused. These depend on many factors including the diffusion coefficient of the solute in the base metal, initial filler thickness, solubility of the MPD element and its concentration gradient in the base material.

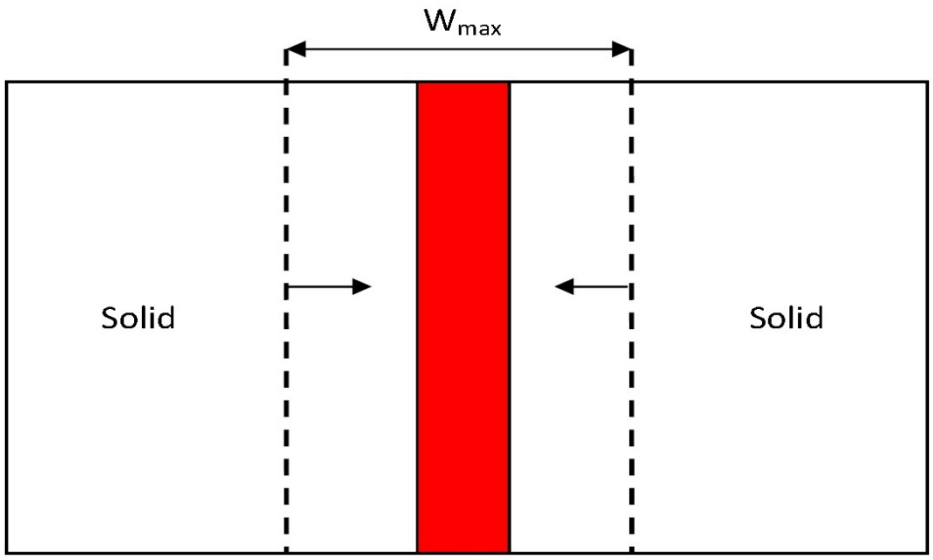

Figure 2.5: Isothermal solidification of liquated interlayer

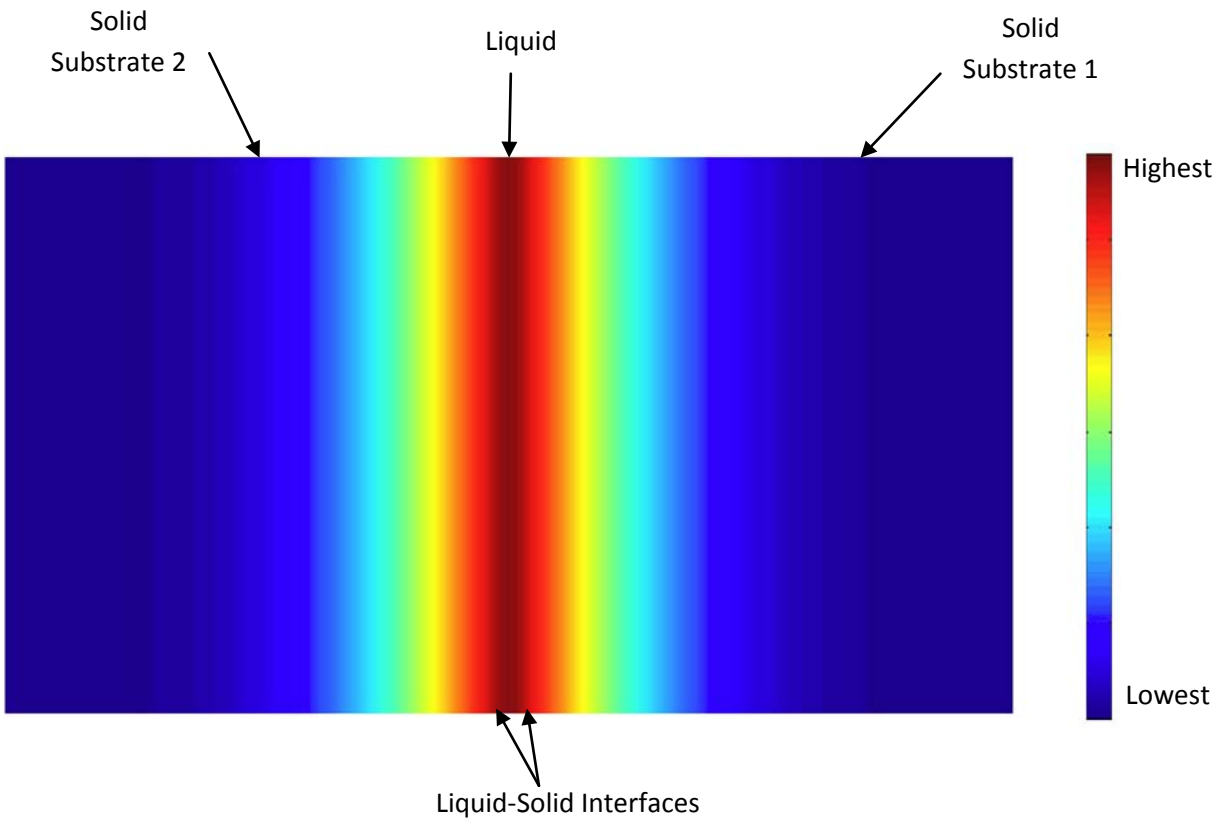

Figure 2.6: Numerical simulation illustrating the MPD solute distribution during the isothermal solidification stage of TLP bonding

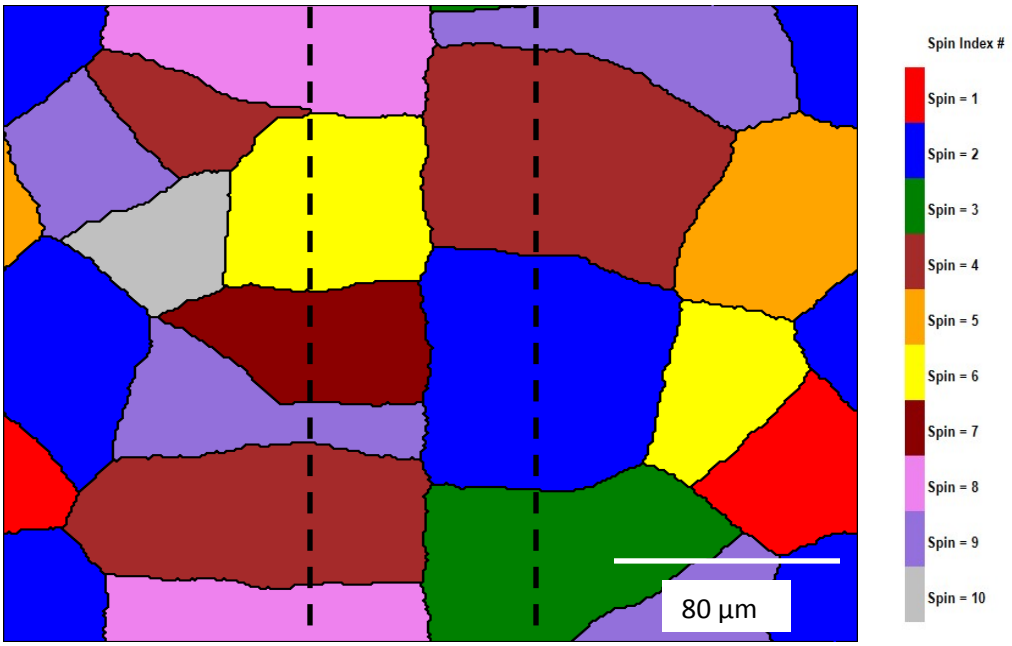

Figure 2.7: Numerical simulation of the joint microstructure showing complete isothermal solidification and elimination of the liquated centerline eutectic

Modeling of the isothermal solidification stage has been done by various authors in an effort to better understand how to optimize the isothermal solidification stage. In these models, local equilibrium is assumed to exist at the solid-liquid interface at the bonding temperature and the effect of convection in the liquid is generally assumed to be negligible due to the small thickness of the liquid interlayer with uniform composition. The interdiffusion coefficients in the liquid and the solid are assumed to be independent of composition and the base metal is generally taken to be a semi-infinitely long medium. Analytical modeling approaches used for TLP bonding can be generally classified into two categories, single-phase and two-phase solutions.

The single-phase solution treats the system as a single semi-infinite base metal with a constant solute concentration ($C_{\alpha L}$) at its mating surface with the liquid phase. This eliminates the challenge of dealing with the liquid phase and the migrating solid-liquid interface [31]. The two-phase analytical solution treats the system as two semi-infinite phases with a coupled diffusion-controlled moving solid-liquid interface. This is more accurate than the single-phase solution, since it better approximates the process and it allows the interface to advance towards the joint centerline as the liquid is being consumed.

Single Phase Stationary Interface Analytical Solution

For a semi-infinite medium with a constant surface composition Fick's second law of diffusion can be expressed by using an error function, as follows:

$$C(x,t) = C_{\alpha L} + (C_0 - C_{\alpha L})erf\left(\frac{x}{2\sqrt{Dt}}\right) \tag{2.4.6}$$

Differentiating with respect to x yields:

$$\frac{\partial C(x,t)}{\partial x} = (C_0 - C_{\alpha L})\frac{\partial}{\partial x} erf\left(\frac{x}{2\sqrt{Dt}}\right) \tag{2.4.7}$$

Equation 2.4.7 can be expressed as:

$$\frac{\partial C(x,t)}{\partial x} = \frac{C_0 - C_{\alpha L}}{\sqrt{\pi Dt}} \exp\left(\frac{-x^2}{4Dt}\right) \tag{2.4.8}$$

Tuah-Poku et. al. [32] suggested that the solidification stage is complete when all excess solutes in the initial liquid have diffused across the solid-liquid interface. The total mass, M, transferred is given by:

$$M = \int J dt = \int (C_{\alpha L} - C_0)\left(\sqrt{\frac{D}{\pi t}}\right) dt \tag{2.4.9}$$

where J is the diffusion flux and solving Equation 2.4.9 gives

$$M = 2(C_{\alpha L} - C_0)\left(\sqrt{\frac{D}{\pi t}}\right) \tag{2.4.10}$$

A mass balance of the initial solute and the amount of solute diffused yields:

$$C_F W_o = 2M \tag{2.4.11}$$

where C_F is the MPD solute concentration in the filler metal, and W_o is the initial filler thickness.

The time required to achieve complete isothermal solidification can then be expressed as:

$$t = \frac{\pi}{16D}\left(\frac{C_F W_o}{C_{\alpha L} - C_o}\right)^2 \tag{2.4.12}$$

where $C_{\alpha L}$ is the solute concentration at the interface; C_o is the initial composition of the MPD in the base metal; D is the solute diffusion coefficient, and t stands for time.

Two Phase Moving Interface Analytical Solution

Using a two-phase analytical approach, Lesoult [33] treated the solid-liquid interface as a moving boundary to derive an expression for the time for complete isothermal solidification. The solute concentration in the base material was assumed to take the general form:

$$C(x,t) = A + B.erf\left(\frac{x}{2\sqrt{Dt}}\right) \tag{2.4.13}$$

where A and B are constants. As a boundary condition at the interface, $C(X(t),t) = C_{\alpha L}$, and farther away from the interface the boundary condition can be expressed as $C(\infty,t) = C_0$.

Taking X(t) as the moving interface and knowing that X(t) must be proportional to the root of time as seen in Equation 2.4.14, Lesoult [33] used a mass balance approach to derive the following equation:

$$X(t) = -2K\sqrt{Dt} \tag{2.4.14}$$

where K is the rate constant. Increasing K results in faster solid-liquid interface motion and shorter duration for complete isothermal solidification. The constants A and B can be

solved to produce Equations 2.4.15 and 2.4.16.

$$A = C_0 - \frac{C_{\alpha L} - C_0}{erf(K) - 1} \tag{2.4.15}$$

$$B = \frac{C_{\alpha L} - C_0}{erf(K) - 1} \tag{2.4.16}$$

Therefore, for a semi-infinite medium the concentration can be expressed as:

$$C(x,t) = C_0 - \frac{C_{\alpha L} - C_0}{erf(K) - 1} + \left(\frac{C_{\alpha L} - C_0}{erf(K) - 1} \right) . erf\left(\frac{x}{2\sqrt{Dt}} \right) \tag{2.4.17}$$

and by using the mass balance equation,

$$\left(C_{L\alpha} - C_{\alpha L} \right) \frac{d}{dt} X(t) = D \left. \frac{\partial C(x,t)}{\partial x} \right|_{x = X(t)} \tag{2.4.18}$$

Lesoult [33] used numerical methods to calculate the rate constant K in Equation 2.4.19 and used the value of K to compute the time required for complete isothermal solidification based on Equation 2.4.20. Sakamoto et. al. [34] and Ramirez and Liu [35] also followed the same approach.

$$\frac{C_{\alpha L} - C_o}{C_{L\alpha} - C_{\alpha L}} = \sqrt{\pi} \frac{K(1 + erf(k))}{\exp(-K^2)} \tag{2.4.19}$$

$$t = \frac{W_{\max}^2}{16 K^2 D} \tag{2.4.20}$$

where W_{max} is the maximum width of the liquated region obtained during base material dissolution and can be calculated by using the following equation:

$$W_{\max} = \frac{C_F W_o}{C_{L\alpha}} \tag{2.4.21}$$

The single-phase solution derived by Tuah-Poku et. al. [32] reported high estimates of the isothermal solidification time compared to their experimental results but it has one advantage over the two-phase solution in that the latter requires a numerical solution to solve the rate constant K. As previously stated, in analytical models the base metal is assumed to be semi-infinite, which may be valid for some engineering applications where the thickness of the pieces to be joined is often large relative to diffusion distances. In certain other applications, however, such an assumption might not hold. For example in the microelectronics industry and for honey-comb structures, the parts can be very small or very thin, and as such assuming a semi-infinite "sink" can be grossly inaccurate [36].

2.4.5 Joint Homogenization

It is usually assumed the homogenization stage follows the isothermal solidification stage. During homogenization, the MPD solute concentration at the joint decreases while other elements from the base alloy diffuse into the joint [37]. The homogenization stage is complete when the microstructure and the chemistry of the joint are similar to those of the base alloy. There can be an acceptable amount of MPD solute that remains at the joint, which depends on the material and intended application of the repaired component. The solute concentration at the joint, however, needs to be below the concentration required to form second phases which are considered deleterious to the mechanical properties of the material.

2.5 Grain Boundaries and TLP Bonding of Polycrystalline Materials

In SX materials, atoms are arranged in a long range periodic order. Due to entropic effects which favor the presence of imperfections in the microstructure of solids, naturally occurring SXs of considerable size are very rare in nature and can only be obtained under controlled conditions. If there is an orientation difference between two adjacent parts of a crystal, a boundary will exist between these two parts which results in the formation of a grain boundary that separates the crystals which are compositionally similar but exhibit different orientations. Orientation of the grain boundary can be identified by relative rotation angle θ which would bring two adjacent grains into perfect registry [39]. Grain boundaries can be divided into low angle boundary, high angle boundary and coincidence site lattice boundary. Low angle boundaries include tilt boundaries, where the boundary plane is parallel to the axis of rotation, and twist boundaries, where the boundary plane is perpendicular to the axis of rotation. Generally, the energy of low angle grain boundaries increases with misorientation angle. The grain boundary energy, however, becomes independent of misorientation angle at angles higher than 15^{o}, when the boundary can be classified as a high angle boundary [40]. The misorientation angle at which transition from low to high angle grain boundaries takes place is between 10^{o} to 15^{o}.

Harrison [41] defined three categories of kinetics of atomic diffusion along grain boundary, depending on the relationship between the lattice diffusion distance and material grain size. These are summarized as follows;

- *Type A kinetics.* Here, the lattice diffusion distance is much larger than the grain size. Hart [42] demonstrated the existence of an apparent diffusion coefficient that combines the diffusivity in the bulk material with the fraction of sites associated with the grain boundaries, f. The apparent diffusion coefficient is expressed as:

$$D_{app} = D_b\left(1 + f\frac{D_{gb}}{D_b}\right) \tag{2.5.1}$$

  where D_{gb} is the diffusion coefficient along the grain boundary and D_b is the diffusion coefficient in the bulk material.

- *Type B kinetics.* In Type B kinetics, the lattice diffusion distance is much less than the grain size and each grain boundary is assumed to be isolated. This is similar to the semi-infinite bi-crystal situation first modeled by Fisher [43]. Lidiard et. al. [44] reported that in Type B kinetics, the amount of material removed at time t is proportional to $t^{3/4}$ and that there is no single apparent diffusion coefficient associated with this type of kinetics.

- *Type C kinetics.* In Type C kinetics, bulk diffusion is negligible and diffusion occurs only within the grain boundary region. Different apparent diffusion coefficients may be calculated depending on the type of experiment that is being performed.

In TLP bonding of SXs, solute transport depends on volume diffusion in the solid and the liquid. However, in polycrystalline materials, grain boundaries can affect the solute diffusion by a number of factors including:

- *grain boundary diffusion.* Diffusivity is higher at grain boundary regions than in the bulk

material when the temperature is in the range T = 0.5-0.75T_m, where T_m is the equilibrium melting temperature. At these temperatures, the ratio of grain boundary diffusivity to bulk diffusion D_{gb}/D_b can reach 10^5 or higher. At temperature T > 0.75T_m the ratio D_{gb}/D_b is 10^3 or less [45].

- *grain boundary migration:* Solute transport can also occur by diffusion-induced grain boundary migration. A very interesting observation made by Hillert and Pardy [46] when they studied grain boundary migration due to the diffusion of zinc atoms along grain boundaries in thin iron films. The precise nature of grain boundary migration is still quite complex and factors that can influence this mechanism include:

  i) free energy differences due to the compositions of the two adjacent grains.

  ii) elastic effects due to the sharp change in composition ahead of the moving grain boundary.

  iii) adsorption of the solute at the grain boundary.

- *grain boundary elemental segregation.* Elemental segregation to the grain boundary regions may influence intergranular free energy and solute diffusivity [47]. This may occur prior to joining during pre-bonding heat treatment or during bonding, which may lead to the formation of intergranular precipitates that could affect the properties of bonded materials.

- *grain Boundary grooving:* It has been established that when a grain boundary intercept a liquid-solid interface the liquid tends to penetrate the grain boundary resulting in a groove in order for the liquid-solid interfacial energy to balance the grain boundary

energy. A detailed explanation of the grain boundary grooving phenomenon was first proposed by Mullins [48]. In his analysis, grain boundary grooving occurred when a bi-crystal contacted a saturated fluid phase at a sufficiently high temperature. It was proposed that grooving can occur as a result of surface diffusion, volume diffusion, and evaporation/condensation. In an experimental study by Allen [49], Cr, Mo, and W alloyed with Re greed with Mullin's theoretical predictions. It should, however, be noted that Mullins' analytical solutions assumed that interface motion is driven only by interfacial curvature, which implies that a planar interface will not migrate. This is not necessarily true in TLP bonding where the main driving force for interface migration is the solute concentration gradients around the interface. Therefore, even in the absence of grain boundaries, a completely planar liquid-solid interface will still migrate depending on the solute distribution near the interface.

Saida et al. [50] investigated the influence of grain size on the time required to achieve complete isothermal solidification. They used Ni-11 wt.% P filler alloy and pure Ni as a base material and performed the bonding at 1150 ^{o}C. They reported that the eutectic width decreased linearly with the square-root of brazing time in single crystal, coarse-grained and fine-grained nickel. Also, when comparing the time for complete isothermal solidification, they reported that the solidification time decreased in the order: single crystal, coarse-grained and fine-grained nickel. They attributed the observation qualitatively to increase in apparent mean diffusion coefficient of phosphorous in solid nickel due to decrease in grain size.

North et. al. [51] suggested that the influence of grain size on the motion of the liquid-solid

interface could be the reason behind the large discrepancy between their experimentally observed isothermal solidification completion times and theoretical values predicted without considering the role of grain boundaries. Tuah-Poku et al. [52] also suggested that liquid penetration at the grain boundaries affected the accuracy of their calculated and observed isothermal solidification times. Using scanning electron microscopy (SEM) and electron channeling pattern (ECP) technique, Kokawa et. al. [53] observed that the liquid penetration depth at the grain boundary depended on the amount of misorientation at base metal grain boundaries. They noted that liquid penetration was greatest at high angle grain boundaries.

2.6 Mathematics of Diffusion

The kinetics of TLP bonding is mainly governed by atomic diffusion of the MPD solute into the base material and, as such, it is worthwhile to briefly present an overview of the fundamental mathematics of atomic diffusion. Diffusion is a process by which matter is transported by an atomic motion primarily to reduce the Gibb's free energy of a material, which often involves the migration of solute atoms from a region of high concentration to a region of lower concentration. Fick first quantified diffusion by adopting a mathematical equation for heat conduction derived by Fourier. In Fick's second law, the non-steady state of diffusion is expressed in Cartesian coordinates x, y and z, as [54]:

$$\frac{\partial C}{\partial t} = D\left(\frac{\partial^2 C}{\partial x^2} + \frac{\partial^2 C}{\partial y^2} + \frac{\partial^2 C}{\partial z^2}\right) \tag{2.6.15}$$

where D is the diffusivity of the solute in the substrate material, assumed here independent of solute concentration.

However, in some systems, D may depend upon the concentration of the diffusing substance, C. In this case, Equation 2.6.15 becomes:

$$\frac{\partial C}{\partial t} = \frac{\partial}{\partial x}\left(D\frac{\partial C}{\partial x}\right) + \frac{\partial}{\partial y}\left(D\frac{\partial C}{\partial y}\right) + \frac{\partial}{\partial z}\left(D\frac{\partial C}{\partial z}\right) \tag{2.6.16}$$

In cylindrical coordinates with polar coordinates r and θ :

$$x = r(\cos\theta) \tag{2.6.17}$$

$$y = r(\sin\theta) \tag{2.6.18}$$

Thus, by considering an element volume with dimensions dr, $d\theta$, dz, the equation for diffusion in a cylinder becomes:

$$\frac{\partial C}{\partial t} = \frac{1}{r}\left\{\frac{\partial}{\partial r}\left(rD\frac{\partial C}{\partial r}\right) + \frac{\partial}{\partial \theta}\left(\frac{D}{r}\frac{\partial C}{\partial \theta}\right) + \frac{\partial}{\partial z}\left(rD\frac{\partial C}{\partial z}\right)\right\} \tag{2.6.19}$$

In spherical coordinates with polar coordinates r, θ and ϕ:

$$x = r(\sin\theta)(\cos\phi) \tag{2.6.20}$$

$$y = r(\sin\theta)(\sin\phi) \tag{2.6.21}$$

$$z = r(\cos\theta) \tag{2.6.22}$$

The diffusion equation for a sphere becomes:

$$\frac{\partial C}{\partial t} = \frac{1}{r^2}\left\{\frac{\partial}{\partial r}\left(r^2 D\frac{\partial C}{\partial r}\right) + \frac{1}{\sin\theta}\frac{\partial}{\partial \theta}\left(D\sin\theta\frac{\partial C}{\partial \theta}\right) + \frac{D}{\sin^2\theta}\left(\frac{\partial^2 C}{\partial \phi^2}\right)\right\} \tag{2.6.23}$$

The bulk lattice diffusion coefficient is generally represented by the classical Arrhenius-type

equation:

$$D = D_o \exp\frac{-Q}{RT} \tag{2.6.24}$$

where D_o is known as frequency factor, Q is the activation energy for diffusion, R is the gas constant and T is the absolute temperature. In the presence of grain boundaries, it has been experimentally found that diffusion coefficients along grain boundaries and free surfaces, D_g and D_{sur} , respectively, can be expressed by the following equations [54]:

$$D_g = D_{go} \exp\frac{-Q_g}{RT} \tag{2.6.25}$$

$$\text{or } D_{sur} = D_{suro} \exp\frac{-Q_{sur}}{RT} \tag{2.6.26}$$

In general, when compared to lattice diffusion, D_L: $D_{sur} > D_g > D_L$. Surface diffusion can play an important role in many metallurgical phenomena. However, generally speaking, the total grain boundary area is much greater than the surface area; hence, grain boundary diffusion is usually more important.

Rapid diffusion along grain boundaries can increase the overall solute transport in some systems, which may result in an increase in apparent diffusivity, D_{app} , in the material as a whole. Assuming that the concentration gradients in the lattice and along the grain boundary are identical, the solute fluxes through the solid lattice, J_s , and through the grain boundary, J_g , are given by:

$$J_s = -D_s \frac{\partial C}{\partial x} \quad \text{and} \quad J_g = -D_g \frac{\partial C}{\partial x} \tag{2.6.27}$$

If the grain boundary has a thickness of δ and the grain size is d, the total solute flux is given by:

$$J = \left(J_g \delta + J_s d\right)/ d = -\left(\frac{D_g \delta + D_s d}{d}\right)\frac{\partial C}{\partial x} \tag{2.6.28}$$

The apparent diffusion coefficient in this case becomes:

$$D_{app} = D_s + D_g \delta / d \tag{2.6.29}$$

Hence, the relative importance of lattice and grain boundary diffusion in relation to the total solute flux depends on the ratio $D_g \delta / D_s d$.

2.7 Numerical Methods to Simulate Propagation of Interphase Interfaces

Over the past few decades, computational methods used to mathematically simulate and analyze microstructural phenomena in materials science and condensed-matter physics have experienced significant advancement with the fast development of computers. Compared to the early 90's, there is presently a considerable number of computational methods for the analysis of microstructural evolution and propagating interfaces. Some of the most popular methods are discussed in this section.

The analysis of the evolution of interfaces during solid-state phase transformations and solidification reactions is one of the most complex problems encountered during materials simulation, mainly due to the highly complex topology (such as in dendritic solidification) and the large number of process parameters that affect the evolution kinetics of interphase interfaces. Various factors such as solute concentration gradient, thermal gradient, boundary curvature, surface energy and conservation laws influence the kinetics of interface migration. The continuously moving interfaces (or boundaries) coupled with interfacial discontinuities and the non-linearity of propagating boundary problems significantly complicate the analysis. Over the years, some refined and now popular methods have been used to solve the moving-boundary problem, which are summarized as follows.

2.7.1 Interface-Tracking Methods

Interface tracking methods, also known as boundary-tracking and front-tracking methods, explicitly track the motion of an interface by tracking the motion of nodal points imposed directly at the interface. In this method, a domain is divided into discretized elements within which thermal and solutal distributions are calculated for each phase inside the domain. This is normally done through finite difference and finite volume methods, or the more flexible finite element methods. Depending on the problem being analyzed, an energy balance or a mass balance equation is applied at the interface, which governs its movements depending on the local gradients [55].

Fourier's law of transient conduction can be used to calculate the local temperature distribution within a domain which can be expressed as follows:

$$\rho C_p\left(\frac{\partial T}{\partial t}\right)=\nabla\left(K.\nabla T\right) \tag{2.7.1}$$

where ρ is density, C_p is the heat capacity, K is conductivity, t is time and T is temperature.

Transient solute distribution can be expressed by using Fick's second law of diffusion:

$$\left(\frac{\partial C}{\partial t}\right)=\nabla\left(D.\nabla C\right) \tag{2.7.2}$$

where C is the solute concentration, t is time and D is diffusivity of solute.

If the interface moves due to thermal heat flow (as in the propagation of liquid-solid interface during thermal dendritic solidification) then a heat balance equation is applied which ensures an energy balance at the interface and relates the diffused energy to the interfacial velocity [55].

$$K_L.\nabla T\big|_{I-}-K_S.\nabla T\big|_{I+}=\rho\lambda\frac{dI}{dt} \tag{2.7.3}$$

where λ is the latent heat for fusion and I is the interface.

For a case where movement of the interface is dependent on solute diffusion, a mass balance equation can be applied:

$$D_L\nabla C_L\big|_{I-}-D_S\nabla C_S\big|_{I+}=\left[C_{\alpha L}-C_{L\alpha}\right]\frac{dI(t)}{dt} \tag{2.7.4}$$

where $C_{\alpha L}$ and $C_{L\alpha}$ are the equilibrium solidus and liquidus concentrations.

The above equations are solved by keeping in mind that equilibrium boundary conditions are imposed at the interface. A Gibbs-Thompson effect is incorporated at the interface to account for the effects of curvature on the equilibrium temperature and solubility at the interface.

A major advantage of the interface tracking method is that it allows for direct tracking of the interface and can be highly efficient computationally. Depending on the type of problem being analyzed, it can provide an accurate representation of the moving interface. The method, however, is very sensitive to topological variations at the migrating interface [55]. Therefore, inaccuracies may arise when nodal points at the interface get too close together or too far apart. As a result, to ensure simulation validity, an extra step may be required to either remove or add nodal points, depending on the position of the nodes relative to one another. Depending on the nature of the problem, this can be very difficult to represent during programming, which may result in increased computational time. Moreover, major difficulties can be encountered when an interface breaks apart into separate boundaries or when interfaces merge together. Special attention is needed to mitigate these problems which, in turn, can drastically increase the complexity of programming.

2.7.2 Level-Set Methods

The level-set method is a more robust and powerful computational technique to directly track the propagation of interfaces than interface-tracking methods. It was developed by Sethian and Osher [56] and has been used in many areas including computer vision, mesh generation and image segmentation. It has proven to be a promising mathematical tool to track migrating

interfaces with reasonable computational times. In many problems, it has been effective in handling topological complexities such as corners and cusps.

The method involves the use of a level-set variable, φ, which a signed distance function to the solid-liquid interface with "+" sign in the liquid phase, and "-" sign in the solid phase and a value of zero at the interface. To obtain the evolution of the interface, it is necessary to find values where the level set function is zero, or in other words, the zero-level-set of the function. The evolution of the higher-order implicit level set function φ can be expressed as [57]:

$$\left(\frac{\partial \phi}{\partial t}\right) + \vec{F}.\nabla\phi = 0 \tag{2.7.5}$$

where $\vec{F}$ is an external velocity field and t is time.

If the interface motion is governed by mean curvature, then, $\vec{F} = F_n\vec{N} + F_t\vec{T}$, where F_n and F_t are the normal and tangential velocities of the interface and $\vec{N}$ and $\vec{T}$ are the normal and tangential vectors, respectively. $\vec{N}$ and $\nabla\phi$ are along the same direction while for any tangential vector, $\vec{T}.\nabla\phi = 0$. This implies that the tangential velocity components vanish when inserted into the level set equation, i.e.:

$$\left(\frac{\partial \phi}{\partial t}\right) + \left(F_n\vec{N} + F_t\vec{T}\right).\nabla\phi = 0 \tag{2.7.6}$$

which yields

$$\left(\frac{\partial \phi}{\partial t}\right)+\left(F_n \vec{N}\right)\nabla \phi = 0 \tag{2.7.7}$$

The normal vector $\vec{N}$ is equivalent to $\frac{\nabla \phi}{|\nabla \phi|}$. Therefore,

$$\left(\frac{\partial \phi}{\partial t}\right)+\frac{\nabla \phi}{|\nabla \phi|}.\nabla \phi = 0 \tag{2.7.8}$$

For a convection-diffusion case, the level set equation can be described as:

$$\left(\frac{\partial \phi}{\partial t}\right)+\vec{F}.\nabla \phi = b\kappa|\nabla \phi| \tag{2.7.9}$$

Assuming that the movement of the interface is based on a curvature dependent term (such as $F_n = a - b\kappa$) and an external velocity field, then, a more general equation is applicable:

$$\left(\frac{\partial \phi}{\partial t}\right)+\vec{F}.\nabla \phi + a|\nabla \phi| = b\kappa|\nabla \phi| \tag{2.7.10}$$

which includes the velocity term $\vec{F}$ of the bulk material, displacement normal to the interface and migration driven by mean curvature.

In materials science, the level set method has found a considerable amount of applications including simulation of solidification, and dissolution of particles in multi-component alloys. Tan and Zabaras [58] used the level set method to model dendritic growth during solidification in pure and multi-component materials and studied the interaction between multiple dendrites

during solidification [59]. They also incorporated multi-scale methods and melt convection into the calculations. Javierre et al. [60] also used the level set method to develop a three dimensional model for precipitate dissolution in binary alloys.

Disadvantages of the method include its sensitivity to instabilities and oscillations if simple (or intuitive) numerical methods are used. Specialized numerical methods such as essentially non-oscillatory (ENO) interpolation and Range-Kutta techniques can be used to solve the level set equation. Additionally, classical level set methods require constant re-initialization of the approximated level-set function to ensure validity of the calculated solution [61].

2.7.3 Phase-Field Methods

Over the past two decades, significant progress has been made in the simulation of microstructure evolution in solidification processes by using phase-field methods. The basic idea of the phase-field method is to employ a phase field variable φ that varies smoothly from zero to unity between two phases over a diffused interface region which has a small but numerically resolvable thickness. The control equation for the phase-field variable is derived from the thermodynamics of phase transition. Important physical mechanisms such as curvature, anisotropy and kinetics effects are implicitly incorporated in the phase-field equation. Field variables can either be conserved or non-conserved depending if they satisfy the local conservation law. Composition and temperature fields are both conserved, while long-range order parameter fields that describe ordered domain structures are non-conserved. Likewise, artificial phase-fields in solidification

modeling of a single component is non-conserved since their value can go from 0 to 1 for the whole system [62].

The phase-field methodology is based on the construction of a Cahn-Hilliard or Ginzburg-Landau energy or entropy functional. By variational derivatives, a set of partial differential equations for the appropriate thermodynamics quantities, such as temperature and concentration, with an additional reaction-diffusion equation for the phase-field variable can be derived from an energy or entropy functional. In a solid-liquid phase system, a phase-field model may be scaled such that $\phi(\vec{x},t)=1$ in the solid and $\phi(\vec{x},t)=0$ in the liquid and $0<\phi(\vec{x},t)<1$ at the diffuse interface layer.

For a pure material with one component ($c=1$), and internal energy, e, an order parameter $\phi(\vec{x},t)$ characterizes the phase state of the system and its volume fraction in space, $\vec{x}$, to ensure consistency with classical irreversible thermodynamics. The model formulation is based on an entropy functional [62]

$$S(e,\phi)=\int_{\Omega}\left(s(e,\phi)-((\varepsilon a(\nabla\phi)+\frac{1}{\varepsilon}w(\phi))\right) \tag{2.7.11}$$

where s is the bulk entropy density which depends on the phase-field variable ϕ and on the inner energy density e. The contributions $a(\nabla\phi)$ and $w(\phi)$ of the entropy function reflect the thermodynamics of the interface and ε is a small length scale parameter related to the thickness of the diffuse interface.

The phase-field and the energy conservation equations can be derived by taking the derivatives of the entropy function [62].

$$\frac{\partial e}{\partial t} = -\nabla\left\{ M(T,\phi)\nabla \frac{\delta S}{\delta e} \right\} \qquad \text{Energy conservation equation} \qquad (2.7.12)$$

$$\tau\varepsilon \frac{\partial \phi}{\partial t} = \frac{\partial S}{\partial \phi} \qquad \text{Phase-field equation} \qquad (2.7.13)$$

where τ is kinetic mobility, T is temperature, and $M(T,\phi)$ is the mobility related to heat conductivity. A superposition polynomial function $h(\phi)$ is imposed to connect the two phases such that it fulfills the condition $h(1) = 1 \text{ and } h(0) = 0$. For example:

$$h(\phi) = \phi^3(6\phi^2 - 15\phi + 10) \qquad (2.7.14)$$

The governing equation for the temperature field $T(\vec{x},t)$ can be expressed as:

$$\frac{\partial T}{\partial t} = \frac{k}{C_p}\nabla^2 T + \frac{L}{C_p}\frac{\partial h(\phi)}{\partial t} \qquad (2.7.15)$$

where k is thermal conductivity, C_p is the specific heat, and L is the latent heat.

By using classical Lagrangian formalism, the variational derivative $\frac{\delta S}{\delta \phi}$ is given by

$$\frac{\delta S(e,\phi)}{\delta \phi} = \frac{\partial S}{\partial \phi} - \nabla . \frac{\partial S}{\partial(\nabla \phi)} \qquad (2.7.16)$$

Based on the thermodynamics relation $e = f + Ts$, which has a derivative of $\frac{\partial s}{\partial \phi} = -\left(\frac{1}{T}\right)\left(\frac{\partial f}{\partial \phi}\right)$,

the phase-field equation can be expressed in terms of the bulk free energy density, $f(T,\phi)$, instead of the bulk entropy density, $s(e,\phi)$,which yields

$$\tau\varepsilon\frac{\partial\phi}{\partial t}=\varepsilon\nabla\frac{\partial a(\nabla\phi)}{\partial\nabla\phi}-\frac{1}{\varepsilon}\frac{\partial\omega(\phi)}{\partial\phi}-\frac{1}{T}\frac{\partial f(T,\phi)}{\partial\phi} \tag{2.7.17}$$

where $f(T,\phi)$, $\omega(\phi)$ and $a(\nabla\phi)$ can be expressed as:

$$f(T,\phi)=L\frac{T-T_M}{T_M}\phi^2(3-2\phi) \quad \text{Bulk free energy density} \tag{2.7.18}$$

$$\omega(\phi)=\gamma\phi^2(1-\phi)^2 \quad \text{Double well potential} \tag{2.7.19}$$

$$a(\nabla\phi)=\gamma a^2{}_c(\nabla\phi)\left|\nabla\phi\right|^2 \quad \text{Gradient entropy density} \tag{2.7.20}$$

T_M is the melting temperature and γ defines the surface entropy density of the liquid-solid interface. The double well function is a potential with two minima corresponding to the two bulk phases, solid and liquid.

The diffuse-interface approach leads to many computational advantages. There is no need to directly track the motion of the interface because it is implicitly defined in the phase-field variable. Additionally, since the need to directly track the interface is eliminated, this method can be used to simulate the evolution of complex interfaces and can capture intricate local changes in topologies such as secondary and tertiary branching of dendrites. It can also be coupled with the density functional theory to study the atomistic nature of interfaces. It has been shown that the phase field solution for a diffuse interface reduces to the sharp interface

solution in the limit of vanishing interface thickness. This was achieved by Caginalp et al. [63] and it was later rigorously proven by others. Thin interface asymptotics were developed by Karma et al. [64] for the simulation of dendritic growth at small undercoolings, by using the phase-field method. Various versions of phase-field models have been developed to describe formation and coarsening of primary and secondary dendrites during solidification of pure materials and binary alloys.

The quality of the phase-field solution deteriorates with increasing interface thickness. As a result, this necessitates the use of a grid spacing which has an order of or smaller than that of the interfacial thickness. One of the drawbacks of the phase-field method is the significant computational effort required, especially when investigating solidification dendrite formation and multiple array dendritic growth. It has been reported [65] that 10 CPU hours were required to produce a solution using an improved phase-field method to model the growth of a single dendrite. Another drawback of phase-field methods is related to the large number of parameters involved in the solution of the evolution equations many of which are difficult to determine experimentally for accurate physical crystal growth simulation of multi-component alloys [58]. As a result, their values are generally assumed which may affect the validity of the final solution and its agreement with experimental observations. Nevertheless, A large number of research is devoted to advancing phase field methods and mitigating some of these drawbacks.

2.7.4 Cellular Automata Methods

CA methods, like phase-field methods, do not directly track the motion of interfaces. A cellular automaton is a dynamical system, in which space, time, and the states of the system are discrete. It was first developed by John Von Neumann in 1963 after a suggestion by Ulam [66] as a means to study universal copiers and destructors. It was later analyzed by Wolfram [67] in the 1980's as part of his work on analyzing complexity in nature. The CA found a wide range of applications including evolution, natural selection, growth of bacterial cultures, pattern recognition, microstructural evolution, crystallization etc.

In CA, the microstructure is usually discretized into cells. Each cell can have a finite number of states such as concentration, temperature, or phase order parameter (i.e. 0 for liquid and 1 for solid). Transition rules are imposed to determine cell evolution during one time step depending on the states of its neighboring cells, which can be a Neumann-type or Moore-type, in a square cell lattice. The basic idea of CA for solidification studies is to mimic interface propagation by capturing transition from nearby liquid cells to the solid body according to certain criteria. It is assumed that three kinds of possible cells exist within a simulation domain i.e. solid, liquid and interface cells. Solid cells have a solid fraction of 1, liquid cells have a value of 0, and interface cells have a solid fraction which varies between 0 and 1. Cell capturing rules can be applied to calculate the future solid fraction in each cell, depending on the solutal and thermal distribution in the domain. In CA, the interface is not explicitly tracked like in interface-tracking and level set methods. However, the location of the interface can be obtained by determining the cells where the solid fraction varies from 0 to 1.

Heat transfer equation within a domain can be calculated using [68]:

$$\rho C_p\left(\frac{\partial T}{\partial t}\right)=\nabla\left(K.\nabla T\right)-\rho L\frac{\partial f_L}{\partial t} \tag{2.7.21}$$

where T is temperature, ρ is density, t is time, K is the heat conductivity, L is the latent heat, and f_L is the liquid fraction.

The solute conservation at the interface can be expressed as:

$$V_n C_L(1-k)=D_L(\nabla C)-D_S(\nabla C) \tag{2.7.22}$$

where V_n is the normal velocity of the interface, and k is the equilibrium partition coefficient

$$C_{\alpha L}=kC_{L\alpha}$$

When an interface cell grows with velocities V_X and V_Y, in two dimensions, the solid fraction increment can be calculated by using:

$$\partial f_s=\frac{\delta t}{a}\left(V_X+V_Y-V_X V_Y\frac{\delta t}{a}\right) \tag{2.7.23}$$

From the context of solidification, CA has been used to analyze the effect of process parameters on the growth of thermal dendrites and solutal dendritic growth [68]. The method has been also applied to study microstructural evolution during solid-state recrystallization and growth [69]. A major advantage of the method is that it does not directly involve tracking of interface location and its implementation is relatively simpler than the phase-field methods [70]. Additionally, it provides a frame work to simultaneously study changes in the entire

computational domain depending on the state of each cell and its immediate neighbors. This makes the method very useful in studying microstructural evolution where a very large number of different states are present and explicit treatment of localized event is not computationally feasible. Its computational requirements (memory and time) are much lower in comparison to other numerical methods, such as the phase field and direct interface-tracking methods. It can also be coupled with other computational methods such as finite element and finite volume methods to calculate the transient changes in concentration and temperature.

A variation of the method include probabilistic CA. It has also been coupled with the finite element method to simulate crystal growth during solidification. Rappaz et al. [71] used probabilistic CA to study the microstructure formation in solidification processes. Their model included mechanisms of heterogeneous nucleation and grain growth. They also developed a three dimensional CA algorithm coupled with the finite element method and used it to calculate heat flow and model growth of dendrite grains [72. Krane et al. [73] coupled the finite volume method with the cellular automata method to study dendritic growth.

The main disadvantage of this method is that special considerations are needed to resolve anisotropic tendencies as the interface propagates. This anisotropy is mainly due to the structured lattice (computational grid) used for the analysis, which in turn may affect the validity of the final solution. Therefore, special techniques can be used to mitigate these obstacles, such as, randomized grids, non-synchronous scanning, and special growth rules [74].

2.7.5 Monte-Carlo Methods

Monte-Carlo methods are probably the most widely used methods for simulating and analyzing solid-state microstructural evolution and grain growth kinetics. This is mainly due to their flexibility in studying a wide range of phenomena. The method originated from the Potts [75] model, in the context of magnetic domain evolution. Anderson et al. [76] introduced the Potts model into simulations of grain growth to model grain growth kinetics, grain size distribution and topology, influence of particle dispersion and anisotropic grain growth. The model is used to simulate boundary motion driven by curvature variation along the interface. It can also be applied to incorporate anisotropic energy and boundary mobility, which can be used to study anisotropic grain growth, abnormal grain growth, pinning and recrystallization.

In basic Monte-Carlo Potts modeling, the spatial domain is discretized into a set of lattice points onto which a continuum microstructure is bit mapped so that each lattice point is allocated with a grain orientation. The boundaries are not directly tracked, but they are implicitly defined as existing between lattice sites of neighboring grains. The energy of the system is defined as a Hamiltonian which sums the interfacial energy of the system [62]. For example, in the Ising model which describes an ideal two component system, the state of the system is described in terms of the set of components of the system, called spins, which are associated with each lattice site. The system defines a boundary between dissimilar spins and no boundary between similar spins, as follows:

$$\gamma(s_i, s_j) = 0 \quad \text{for} \quad s_i = s_j \tag{2.7.24}$$

$$\gamma(s_i, s_j) = \frac{J}{2} \quad \text{for} \quad s_i \neq s_j \tag{2.7.25}$$

where i represents a site and j is its neighbor, and $J > 0$ is an interfacial energy constant of the system. Thus the energy of the system can be written as a summation over the spatial distribution of the spins as $E = \sum_{i=1}^{N} \sum_{j=1}^{z} \gamma(s_i, s_j)$, where N is the total number of lattice sites in the system and z is the maximum number of neighbors. A Hamiltonian may be included such that $H > 0$, which lowers the energy of one type of spin relative to another. This energy is associated with an external or volume driving force and results in a modified Hamiltonian.

$$E = \sum_{i=1}^{N} \sum_{j=1}^{z} \gamma(s_i, s_j) - H \sum_{i=1}^{N} s_i \tag{2.7.26}$$

The Monte-Carlo method is used to sample different states in a domain. Basically, a random site is chosen, and a change of spin is proposed when energy change associated with a spin swap is calculated. The new spin is then either accepted or rejected depending on this energy change. There are two main methods to perform Monte-Carlo dynamics, Glauber and Kawasaki dynamics [62]. In Glauber dynamics, the spins are unconserved, while they are conserved in Kawasaki dynamics. The new Hamiltonian is computed and the change is accepted or rejected depending on the probability transition function $P(\Delta E)$, which can be expressed as follows:

$$P(\Delta E) = 1 \qquad \text{if} \quad \Delta E \leq 0 \tag{2.7.27}$$

$$P(\Delta E) = \exp\left(\frac{-\Delta E}{kT_s}\right) \quad \text{if} \quad \Delta E > 0 \tag{2.7.28}$$

where kT_s defines simulation thermal energy, and even though it is analogous to the thermal energy of experimental systems, it is not directly related to it.

The Monte-Carlo method has been extensively used to simulate and analyze recrystallization and grain growth. Its popularity is mainly due to its ability to study changes in the entire computational domain simultaneously, regardless of the number of different states/spins present, which makes it a very effective method to study solid-state phase transformation reactions. Ivasishin et al. [77] proposed a 3-D Monte-Carlo model for recrystallization and grain growth during annealing of deformed polycrystalline metallic materials. Fjeldberg et al. [78] used the Monte-Carlo method to study the effect of grain boundary anisotropy and second phase precipitates on the size distribution of grains after recrystallization and grain growth. Harris and Grant [79] proposed a Monte-Carlo simulation model to study dendritic growth. Jorgenson et al. [80] later proposed a Monte-Carlo simulation model to study dendritic instabilities with faceted tips. Plapp et al. [81] proposed a novel hybrid computational method to simulate dendritic solidification in the low undercooling limit, where the dendrite radius is one or more orders of magnitude smaller than the characteristic spatial scale of variation of the surrounding thermal or solutal diffusion field. They combined the diffusion Monte-Carlo method with phase-field formulation of the interface dynamics and showed that it can accurately simulate three-dimensional solidification dendritic growth in a previously unreachable range of low undercoolings.

2.8 Numerical Methods Used for Simulating TLP Bonding

2.8.1 Simulation of Liquid-Solid Interface Migration

The previous section discussed the most common numerical methods used for studying microstructural evolution and propagating interfaces. This section discusses the numerical methods that have been developed specifically for simulating TLP bonding.

Numerical modeling of TLP bonding involves solving diffusion-controlled liquid-solid interface migration equations. Most of the numerical solution methods available in the literature assume a one dimensional (1-D) planar geometry as illustrated in Figure 2.8. The moving boundary problem can be expressed by diffusion equations 2.8.1 to 2.8.3 [82] in which Equation 2.8.1 describes the diffusion in the liquid phase.

$$\frac{\partial C(x,t)}{\partial t} = \frac{\partial}{\partial x}\left(D_L(C(x,t)) \frac{\partial C(x,t)}{\partial x} \right) , \qquad 0 < x < I(t) \tag{2.8.1}$$

$$\frac{\partial C(x,t)}{\partial t} = \frac{\partial}{\partial x}\left(D_S(C(x,t)) \frac{\partial C(x,t)}{\partial x} \right) , \qquad I(t) < x < L \tag{2.8.2}$$

$$D_L(C(x,t)) \frac{\partial C(x,t)}{\partial x}\bigg|_{x=I-} - D_S(C(x,t)) \frac{\partial C(x,t)}{\partial x}\bigg|_{x=I+} = \left[C_{\alpha L} - C_{L\alpha} \right] \frac{dI(t)}{dt}, \qquad x = I(t) \tag{2.8.3}$$

Equation 2.8.2 describes the diffusion in the solid phase. Equation 2.8.3 describes the moving boundary condition at the interface where $C_{L\alpha}$ and $C_{\alpha L}$ represent the equilibrium liquidus and solidus concentration, respectively.

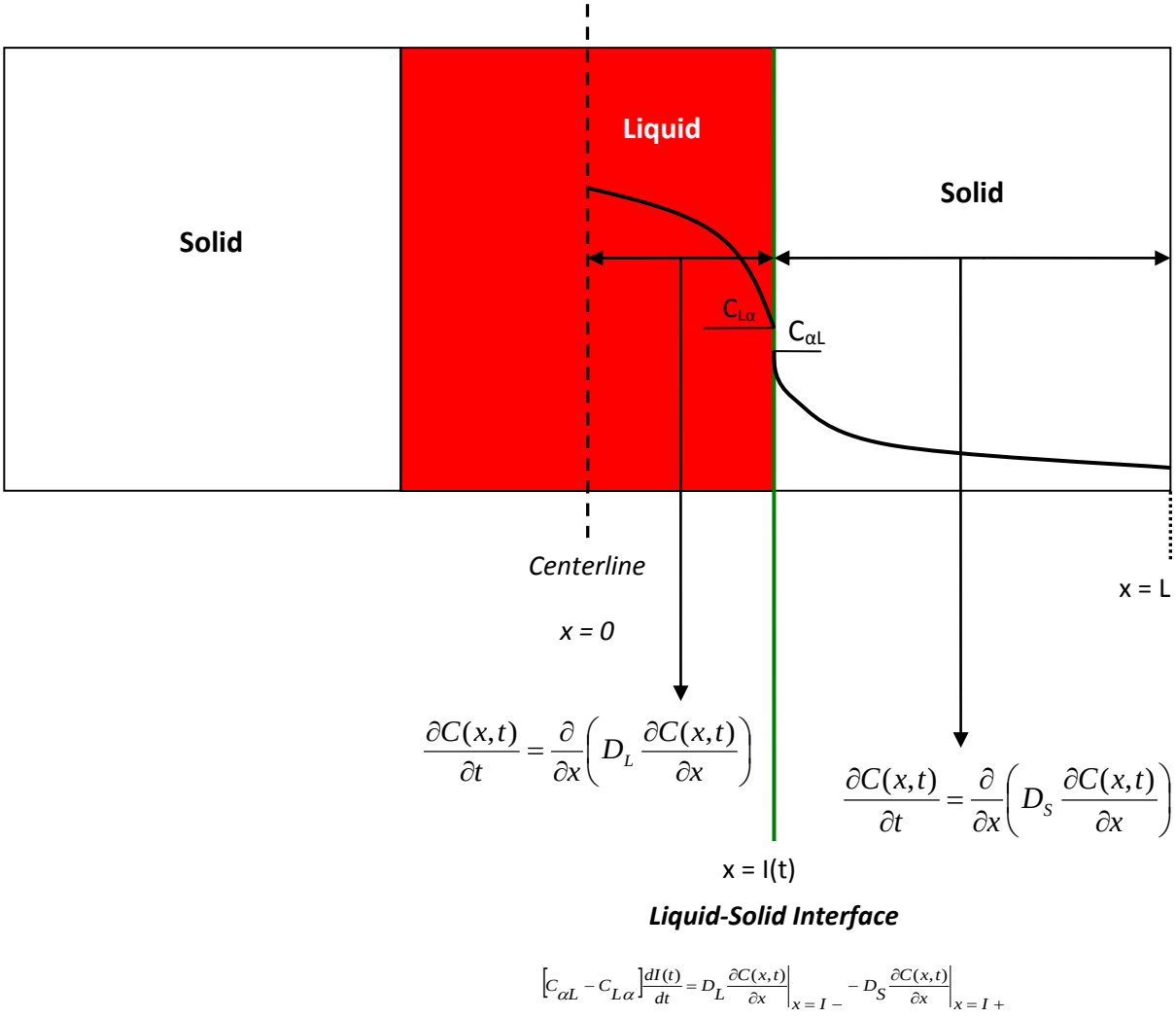

Figure 2.8: Illustration of the one dimensional form of the TLP bonding problem

Nakagawa et al. [83] and Cain et al. [84] solved the set of diffusion equations 2.8.1-2.8.3 by discretizing the domain into fixed points and imposing the interface to be located at one of the discretization points, which implies that only step-wise motion is permitted. However, such a constraint on interface position, may introduce significant errors due to inaccurate approximation of the interface location, which would affect estimates of diffusion fluxes across the interface. Shinmura et al. [85] produced a more refined model that explicitly calculates interface position for predicting its motion. They solved the set of equations 2.8.1-2.8.3 explicitly; however, since the equations are independent, their model results are inaccurate owing to non-conservation of the diffusing solute. Zhou et al. [82] used the approach developed by Shinmura et al. [85] and proposed the use of a quadratic expression for the concentration profile near the interface to better estimate the fluxes and thereby improve the accuracy of the model. Their model, however, involved a semi-implicit scheme where only diffusion equations 2.8.1 and 2.8.2 were solved implicitly while the diffusion equation for the interface was solved explicitly. This caused a limitation on the size of time step that can be used to generate a solution, since the interface motion is generally rapid at the early stages of TLP bonding. Calculations that use large time steps, on the other hand, will contain inaccuracies since solute is no longer conserved. Reducing the time steps, on the other hand, will increase computational effort required to solve the problem. Using the approach by Tanzilli et al. [86], Illingworth et al. [36] solved the problem of fixed spatial discretization by using an approach with variable spatial discretization to conserve solute. A variable mesh that tracks the moving interface was used and it was ensured that the interface position coincided with a discretization point without constraining its motion. Illingworth et. al. [36] further improved the algorithm by ensuring that all the diffusion equations were solved implicitly

resulting in greater accuracy. The model was used to simulate interface motion during TLP bonding of pure Ni with the use of a Ni-P interlayer. It was reported that the model predictions do not exceed the theoretical maximum liquid layer thickness which is consistent with the fact that the model conserves solute.

In the 1-D numerical models discussed above, the following assumptions are made when solving equations 2.8.1-2.8.3:

1. diffusivity is independent of concentration in the liquid and solid phases.
2. the molar volume is assumed to be constant.
3. the liquid-solid interface always exhibits a planar geometry.
4. symmetry exists at the centerline of the joint; and
5. the role of grain boundaries and interfacial kinetics on the migration of the liquid-solid interface is ignored.

2.8.2 Simulation of Diffusion-Induced Grain Boundary Migration

In the work of Zhou and North [88], a simplified case of simulation of solute transport through diffusion-induced grain boundary migration was presented. The grain boundaries were assumed perpendicular to the free surface, with a finite thickness δ and could only move at velocity V in a direction parallel to the free surface, as illustrated in Figure 2.9.

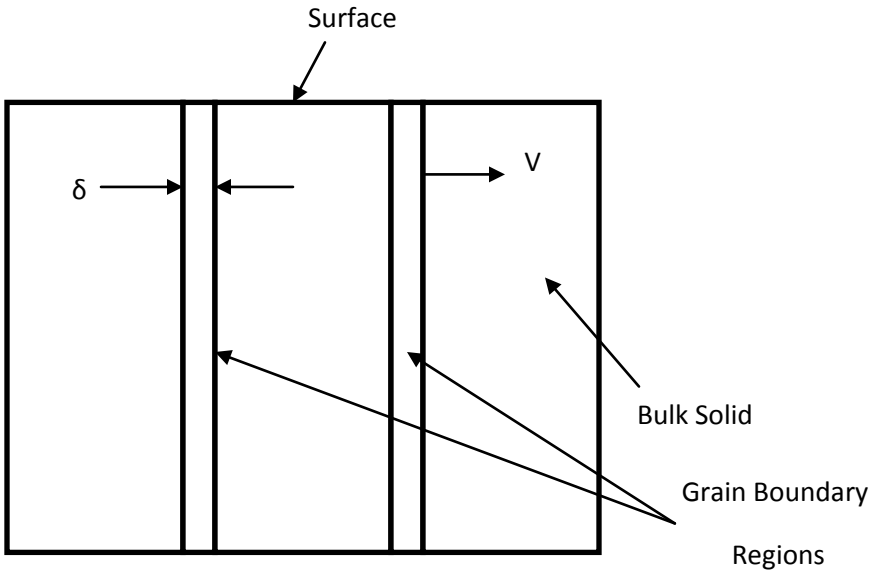

Figure 2.9: Schematic illustrating the grain boundary migration model

The diffusion coefficients, molar volumes and activity coefficients were assumed to be independent of composition. The governing equation for the change of the concentration of diffusing solute with holding time in the bulk material was expressed as:

$$\frac{\partial C}{\partial t} = D_S\left(\frac{\partial^2 C}{\partial x^2} + \frac{\partial^2 C}{\partial y^2}\right) - V\frac{\partial C}{\partial x} \tag{2.8.8}$$

while the solute diffusion along the grain boundary region can be expressed as [88] :

$$\frac{\partial C_{gb}}{\partial t} = D_{gb}\frac{\partial^2 C_{gb}}{\partial y^2} + \frac{D_s}{\delta}\left(\frac{\partial C}{\partial x}\right)\Bigg|_{x=+\delta/2} - \frac{D_s}{\delta}\left(\frac{\partial C}{\partial x}\right)\Bigg|_{x=-\delta/2} \tag{2.8.9}$$

where C and C_{gb} represent the solute concentration in the bulk solid and the grain boundary regions, respectively. D_s and D_{gb} are the diffusion coefficient in the bulk solid and grain boundary regions respectively. V is the rate of migration of the grain boundary and δ is the thickness of grain boundary region.

Zhou et al. [88] solved the equations 2.8.8-2.8.9 using an explicit finite difference method to evaluate the migration of grain boundaries due to the diffusion of solute. They reported that for high D_{gb}/D_s at temperatures in the range of $T < 0.5\text{-}0.75T_m$, grain size reduction can increase the total amount of diffused solute. However, at low D_{gb}/D_s ratios the influence of grain size on the total amount diffused is small. Brener et al. [89] proposed a new approach to address the concept of solute transport by diffusion-induced grain boundary migration. The unique feature in their approach is that they included not only grain boundary diffusion but also diffusion along free surfaces that are in contact with the grain boundary. They also took into account

elastic effects that arise due to the sharp concentration change ahead of the moving grain boundary. They reported that mass transport along free surfaces could play an important role in diffusion-induced grain boundary migration. Yang [90] studied grain boundary migration under the influence of grain boundary grooving by considering that lattice diffusion controls groove growth. A steady state equation was used to calculate the interface migration rate:

$$V\frac{\partial C}{\partial x} = D_S\left(\frac{\partial^2 C}{\partial x^2} + \frac{\partial^2 C}{\partial y^2}\right) \tag{2.8.10}$$

The boundary condition is given by the Gibbs-Thomson equation:

$$C(x,0,t) = C_o + \alpha K(x,t) \qquad \text{with} \qquad \alpha = C_o\gamma_s\Omega/kT \tag{2.8.11}$$

where C_o is the equilibrium concentration, γ_s is the surface energy, Ω is the atomic volume, k is the Boltzmann constant, T is absolute temperature and $K(x,t)$ is the surface curvature. They reported that with migration velocities $V \neq 0$, the grain boundary groove asymmetrically develops with time, as depicted in Figure 2.10, and that the asymmetry increases with migration velocity.

2.8.3 Simulation of Grain Boundary Grooving

In addition to a higher diffusion rate that is known to occur along grain boundaries, another way by which the presence of intergranular regions can influence the diffusion-controlled migration of the liquid-solid interface during TLP bonding is through a phenomenon known as grain boundary grooving.

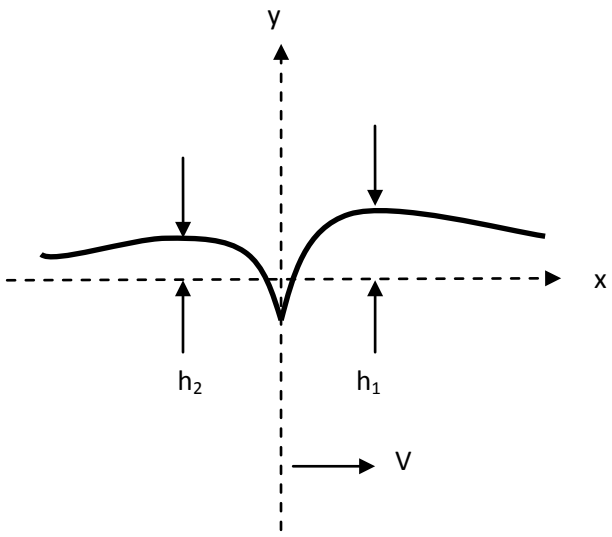

Figure 2.10: Schematic illustrating the asymmetric grooving due to grain boundary migration

In liquid-solid interaction, it has been found that when a grain boundary intercept a liquid-solid interface, in order to achieve an energy balance between the two interfaces, liquid penetration along the grain boundary occurs and results in a groove.

A detailed discussion on grain boundary grooving was first carried out by Mullins [91]. As illustrated in Figure 2.11, at the groove root, the dihedral angle θ, is determined by a well known equation for the balance between the grain boundary energy E_g and the interface energy E_s [92, 93].

$$E_g = 2E_s \cos\theta \tag{2.8.4}$$

An additional driving force for atomic diffusion is associated with the curved liquid-solid interface produced by the grooving process in the form of an excess chemical potential, $\Delta\mu$, which can be expressed as [94]:

$$\Delta\mu = K.\gamma_s\Omega \tag{2.8.5}$$

where K is the curvature, γ_s if the surface tension and Ω is the molar volume.

The interface curvature due to the presence of a grain boundary is given by:

$$K = \frac{\frac{\partial^2 I}{\partial x^2}}{\left(1+\left(\frac{\partial I}{\partial x}\right)^2\right)^{3/2}} \tag{2.8.6}$$

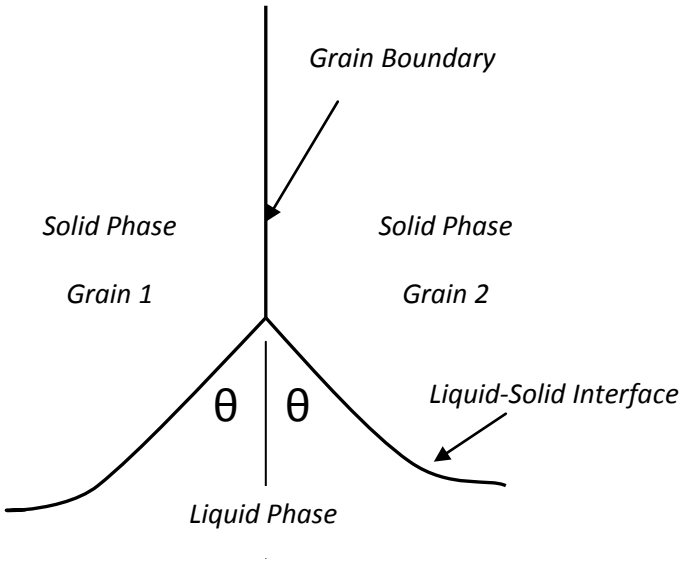

Figure 2.11: Schematic illustrating grain boundary grooving at liquid-solid interface

where I is the interface location. While studying grain boundary grooving of polycrystals exposed to a fluid, Mullins [91] assumed that the slope at the interface does not substantially change from the initial interface configuration, which implies that $\frac{\partial I}{\partial x}$ is much smaller than 1 and, thus, K was approximated to be:

$$K = \frac{\partial^2 I}{\partial x^2} \tag{2.8.7}$$

The approach applies to a situation where no diffusional flow occurs in the liquid and solid phases unless an interfacial curvature exists and the liquid phase intersects a grain boundary region in a solid. Therefore, in a case where grain boundaries are not present, such as in TLP bonding of SXs, the liquid-solid interface will not migrate. Clearly, such an approach cannot be used to simulate TLP bonding because even with the absence of grain boundaries the interface will migrate due to the concentration gradients in both solid and liquid phases.

Vogel et al. [92] also studied grain boundary grooving by using Al solid in contact with liquid Al-In alloy by taking into account grain boundary diffusion. They used a similar approach to that of Mullin's; however, they did not incorporate liquid-solid interface migration caused by diffusion of In atoms from the liquid into the aluminum substrate, which renders the approach unsuitable for tracking interface migration during TLP bonding. Ikeuchi et al. [95] were the first to simulate grain boundary grooving during TLP bonding. They used a moving boundary method to calculate the migration of the interface due to the concentration gradients in the liquid and solid phases along with the concentration at grain boundary. The calculations were coupled with those for the curvature of the interface at the grain boundary region to estimate an

overall migration of the liquid-solid interface. Their approach, however, lacks computationally since they used a fixed discretization scheme, which requires the approximation of interface location between two nodal points. Therefore, the user would need to use fine grids to reduce inaccuracies in the calculations. Additionally, initial planar interface geometry is assumed to coincide with the nodal points of the mesh. Therefore, analysis of rough surfaces, non-planar interface geometries, all of which are typical in actual TLP bonding, cannot be performed. They also solved the diffusion equations by using an explicit finite difference scheme that impose a critical time step size beyond which unstable solutions would result, and, considering that this is a two-dimensional problem, would impose computational limitations since longer times would be required to produce a solution. While this approach might be useful to estimate the interface after some elapsed time, it is impractical to estimate the time required to achieve complete isothermal solidification which can be in the order of several hours depending on the process parameters employed. More importantly, they assumed symmetry at the centerline of the joint. Although, this simplifies the analysis, it does not reflect the actual TLP bonding of polycrystalline materials where the grain boundaries in the upper and lower solids rarely align. In order to more accurately simulate an actual TLP bonding process, the assumption of symmetry needs to be removed and prior to this work, no numerical model without this non-trivial assumption is reported in the literature, but this worthwhile task will be undertaken in the present research.

2.9 Objectives and Scope of the Research

Generally, the market for gas turbine engine repairs constitutes a significant portion of the global economy. In Canada, the market is close to $1 billion in business. To meet the ever-increasing demand for higher operating temperature to achieve improved engine efficiency, the current trend involves the use of SX Ni-base superalloys to manufacture aero-engine and land-based turbine engine components. As stated earlier, these materials are extremely difficult to join by conventional welding methods due to their high susceptibility to weld cracking and formation of stray-grains in welded region, which compromises the integrity of welded materials. An attractive alternative joining technique is the TLP bonding process. Unfortunately, the commercial application of TLP bonding for the joining of SX superalloys is severely restricted due to the long processing time, t_f , required to produce a reliable high temperature joint. The time, t_f , is controlled by the complex interdependence of various process, material and design variables including chemical composition and the interlayer and substrate materials, size of the joint and bonding temperature. The ultimate target of this research is to develop a method to minimize t_f during TLP bonding of SX aerospace superalloys in order to improve the commercial appeal of the joining technique. To achieve this goal, it is fundamentally imperative to acquire an adequate understanding of the factors that are responsible for prolonged processing time during TLP bonding. Therefore, the main objectives of the present research are:

1. to develop an appropriate numerical simulation model to study and understand the actual cause(s) of prolonged t_f that is required to produce reliable eutectic-free joint, and its inverse dependence on temperature, during TLP bonding of SX Ni-based superalloys and to experimentally verify the theoretical predictions; and

2. to use the newly developed numerical model and the acquired knowledge and understanding of the cause(s) of a prolonged t_f to develop a viable procedure to minimize the processing time in SXs, thereby improving the effectiveness and efficiency of the joining technique.

The goal is to primarily use two types of Ni-base superalloys in the research, an older generation superalloy IN 738 and a newer generation superalloy CMSX-4. An attempt is made to verify the applicability of the numerical model developed in the research of TLP joining to (i) another type of new generation heat resistant aerospace materials, Ni_3Al-based intermetallics alloy IC 6 and (ii) dissimilar base materials that involve alloys IN 738, CMSX-4 and IC 6.

CHAPTER 3: THEORETICAL APPROACH AND EXPERIMENTAL WORK

3.1 Theoretical Approach

The t_f required to achieve complete diffusion-controlled isothermal solidification during TLP is dependent on various process variables including the chemical composition of the filler and base-alloy materials, size of the joint and bonding temperature. In terms of the kinetics of the process, material inherent parameters that have been reported to be vital include diffusivity and solubility of the MPD solute in the substrate, initial concentration of the MPD solute in the filler and base-alloys, and presence of grain boundaries. Due to the various materials, design and process parameters involved, the use of a robust numerical simulation tool in studying the interdependence of the variables and their influence on t_f is crucial to optimizing the joining technique and is a vital goal in this research. Currently, most of the numerical simulation schemes available in the literature on TLP bonding are limited to idealized one-dimensional cases that are solved by finite difference methods, where the interface is assumed to be planar. The assumption of planar interface in the one-dimensional models is not necessarily typical in actual TLP bonding and do not allow for investigations of some realistic design and material parameters that may influence the process in practice, such as bonding of dissimilar base materials, bonding of non-parallel mating surfaces and surface roughness, and grain boundary contribution. To analyze and study the possible influence of these parameters on TLP bonding kinetics, particularly, the influence of grain boundaries, at the very least, a two-dimensional numerical analysis is imperative.

Furthermore, existing numerical TLP bonding models necessarily assume symmetry between two adjacent substrates, which is a non-trivial variation from the actual situation in practice, as it is often unrealistic for grain boundaries in the upper and lower substrates to perfectly align. Additionally, the two substrates may have different diffusional and microstructural properties as in the case of TLP bonding of dissimilar materials. Another important limitation of existing numerical models is that, even though powder TLP bonding is very common in the industry to refurbish damaged and cracked aero-engine components, none can handle cases where brazing powder is used instead of foil filler alloys.

To achieve the objectives of this research, a versatile two-dimensional numerical simulation model without symmetry assumption has been developed to:

i) study the influence of grain boundaries in polycrystalline solids on diffusion-controlled liquid-solid migration during bonding in order to verify the reported suggestion that the absence of grain boundaries is the main cause of long t_f in SX materials .

ii) probe and understand the actual causes of a long t_f including verification of other suggested factors in the literature; and

iii) theoretically explore possible ways to minimize t_f. The plan is to follow up on the theoretical analyses with experimental study to verify the numerical simulation predictions.

The computational model utilizes the following:

a) a fully implicit moving-mesh finite element method to calculate transient solute distribution and a direct interface-tracking technique to study the migration of liquid-solid interfaces; and

b) a cellular automata method to model and simulate the dissolution of additive gap-filler alloy powder particles in liquated brazing alloy during TLP bonding of SX material.

The finite element analysis of the TLP bonding process and cellular automata simulations of powder TLP bonding are done by developing and using programming codes written in C++ and Matlab® languages. The model computes an algorithm developed to solve the governing diffusion equations by using a two-dimensional moving-mesh finite element method with higher mesh density near the liquid-solid interface and a user specified convergence error tolerance of about 1E-8 %. The code is written in a manner that does not restrict the motion of the liquid-solid interface and incorporates enhanced intergranular diffusivity and grain boundary grooving. The evolution of the powder particles in the liquid are tracked using a second cellular automata square mesh that is much finer than the mesh used for the finite element analysis to capture the intricate topological changes of the particles during the rapid dissolution stage.

Simulations were implemented using a 2.8GHz 4 Core processor with 8GB of RAM and a 64bit Linux-Windows dual boot operating system.

3.2 Experimental Work

3.2.1. Base and Filler Alloys

The Ni-based superalloys used for the experimental study of the primary objectives in the research are IN 738 and CMSX-4. The alloys were used in the as-cast condition and their chemical compositions are listed in Table 3.1. The brazing alloys used are Metglass MBF-80 brazing foil and Nicrobraz 150 powder and an additive gap-filler alloy IN 738 powder. The chemical compositions of the brazing alloys are listed in Table 3.1.

3.2.2 Sample Preparation and TLP Bonding

As-received base material plates were sectioned by using numerically controlled electro-discharge machining (EDM) into test coupons with dimensions 3 x 3 x 6 mm. The machined surfaces were ground by using 600 grade SiC papers to remove the oxide layers and the ground specimens were subsequently cleaned in an ultrasonic bath of acetone solution for 15 minutes. Ceramic paste was applied on the edges of the specimens to prevent spillage of the liquated filler during bonding. The filler alloy was placed between the cleaned mating surfaces and the assembly was placed in a vacuum brazing furnace operated at a vacuum of approximately 5 X 10^{-5} torr. The TLP bonding process was carried out by using a temperature-time cycle that schematically shown in Figure 3.1.

Table 3. 1: Nominal Composition of IN738, CMSX4 and filler alloy MBF80

	Nominal Composition (wt%)															
Material	**Ni**	**Cr**	**Co**	**Mo**	**W**	**Nb**	**Al**	**Ti**	**Fe**	**Ta**	**C**	**B**	**Zr**	**S**	**Re**	**Hf**
IN738	Bal.	15.84	8.5	1.88	2.48	0.92	3.46	3.47	0.07	1.69	0.11	.012	.04	.001	---	---
CMSX4	Bal.	6.5	9	0.6	6	---	5.6	1.0	---	6.5	---	---	---	---	3	0.1
MBF80	Bal.	15	---	---	---	---	---	---	---	---	0.06	4	---	---	---	---

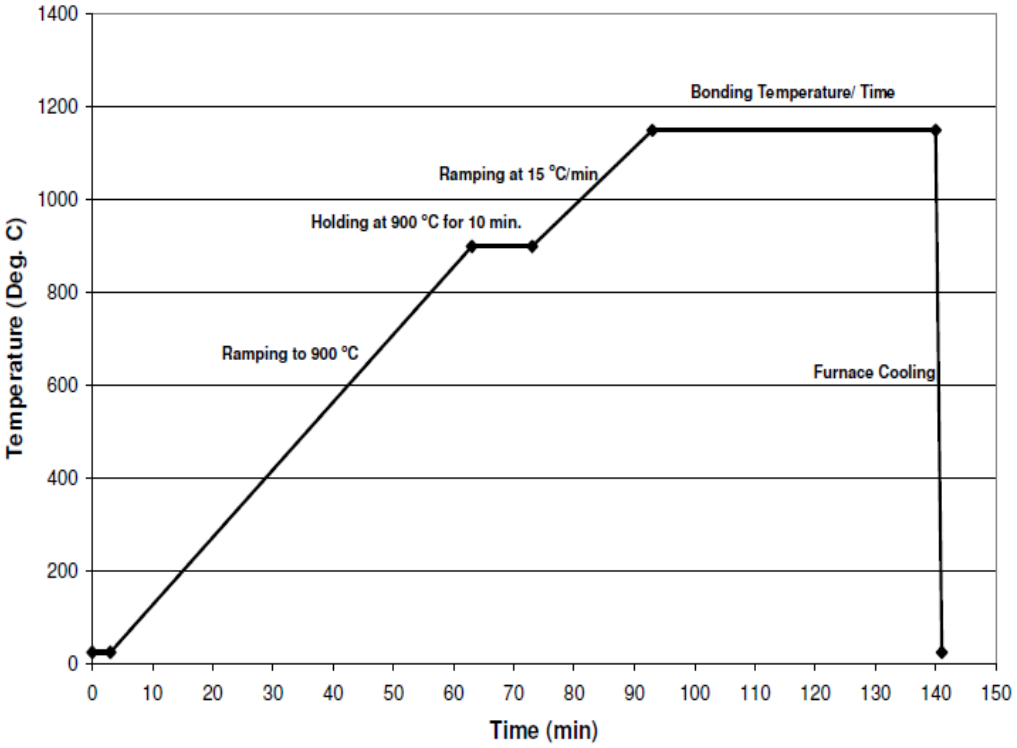

Figure 3. 1: Schematic of heating cycle during TLP bonding

3.2.3 Microstructure Examination and Analyses

The bonded specimens were sectioned by EDM and prepared by standard metallographic procedure for microstructure examination by optical microscopy (OP) and scanning electron microscopy (SEM) techniques. The initial OP assessment of the joint microstructure was performed by the use of an inverted-reflected light microscope equipped with a CLEMEX Vision 3.0 image analyzer. Further microstructural studies (by using secondary and backscatter electron imaging modes) and compositional analyses of brazement were conducted on a JEOL 5900 SEM, equipped with an ultra-thin window Oxford energy dispersive spectrometer (EDS) system equipped with INCA software. A minimum of 20 measurements was taken to calculate the average width of the eutectic microconstituent that formed along the centerline region of the TLP joint in bonded specimens. A SEM study of the bonded specimens was performed in both the secondary electron and backscatter electron imaging modes and semi-quantitative chemical composition analyses were done with the use of the EDS system. The crystallographic orientation relationship between SX substrates and isothermally solidified regions produced by powder mixture of brazing alloy and base-alloy powder was performed by using electron backscatter diffraction (EBSD) based orientation imaging microscopy techniques. This was done with the use of an HKL Nordlys EBSD detector (developed by Oxford Instruments), which was attached to a Philips XL 30 environmental scanning electron microscope. The EBSD detector is equipped with Oxford Instrument HKL Technology Channel 5 suite of programs.

CHAPTER 4: RESULTS AND DISCUSSION

4.1 Development of a 2-D TLP Bonding Numerical Model and Investigation of the Effect of Grain Boundaries on Bonding Kinetics

4.1.1 Introduction

Grain boundaries in crystalline materials are regions of enhanced diffusivity and their presence in solids has been suggested as an important factor that can influence the effective application of some material processing techniques which largely depend on atomic diffusion. The absence of grain boundaries in SX has been reportedly suggested to be a likely cause of long t_f required to produce reliable joint in these materials. Nevertheless, there is controversy as to whether or not enhanced intergranular atomic diffussivity is important in significantly influencing t_f at higher temperatures that is typically encountered during TLP bonding. In this research, the first task is to study the influence of grain boundaries on TLP bonding kinetics in order to verify the aforementioned suggestion of their role in prolonging t_f and this is done through numerical simulation and experimental verification.

A numerical simulation model based on the moving-boundary method was developed to track diffusion-controlled interphase interfacial migration during TLP processing. The governing equations are solved by using the implicit two-dimensional finite element method. The

simulation model is derived in a manner so that solute is conserved and symmetry between the solid substrates is not assumed. A computational domain is imposed such that it consists of a top and bottom solid substrates, a liquid phase, a top and bottom liquid-solid interfaces, and top and bottom grain boundary regions as shown in Figure 4.1. All of which can have independent diffusional properties. The grain boundaries are assumed to be parallel to the y-axis (i.e. perpendicular to an initially planar interface) and intersect the liquid-solid interfaces. A moving mesh is employed such that the upper and lower liquid-solid interfaces are tracked simultaneously without restricting their morphology or motion. This allows for studying TLP bonding of dissimilar base materials where the top and bottom base materials exhibit independent microstructural and diffusional properties. Furthermore, the energy balance between grain boundary energy and liquid-solid interface energy and enhanced grain boundary diffusion rate are incorporated into the algorithm.

4.1.2 Finite Element Formulation of the MPD Solute Concentrations

In the present work, Fick's second law of diffusion can be expressed in a two dimensional form for the bottom solid, liquid and top solid phases, respectively, as follows:

$$\frac{\partial C(x,y,t)}{\partial t} = \frac{\partial}{\partial x}\left(D_{s\_b}(C(x,y,t))\frac{\partial C(x,y,t)}{\partial x}\right) + \frac{\partial}{\partial y}\left(D_{s\_b}(C(x,y,t))\frac{\partial C(x,y,t)}{\partial y}\right)$$

$$0 < y < I_b(t)\,, 0 < x < W \qquad (4.1.1)$$

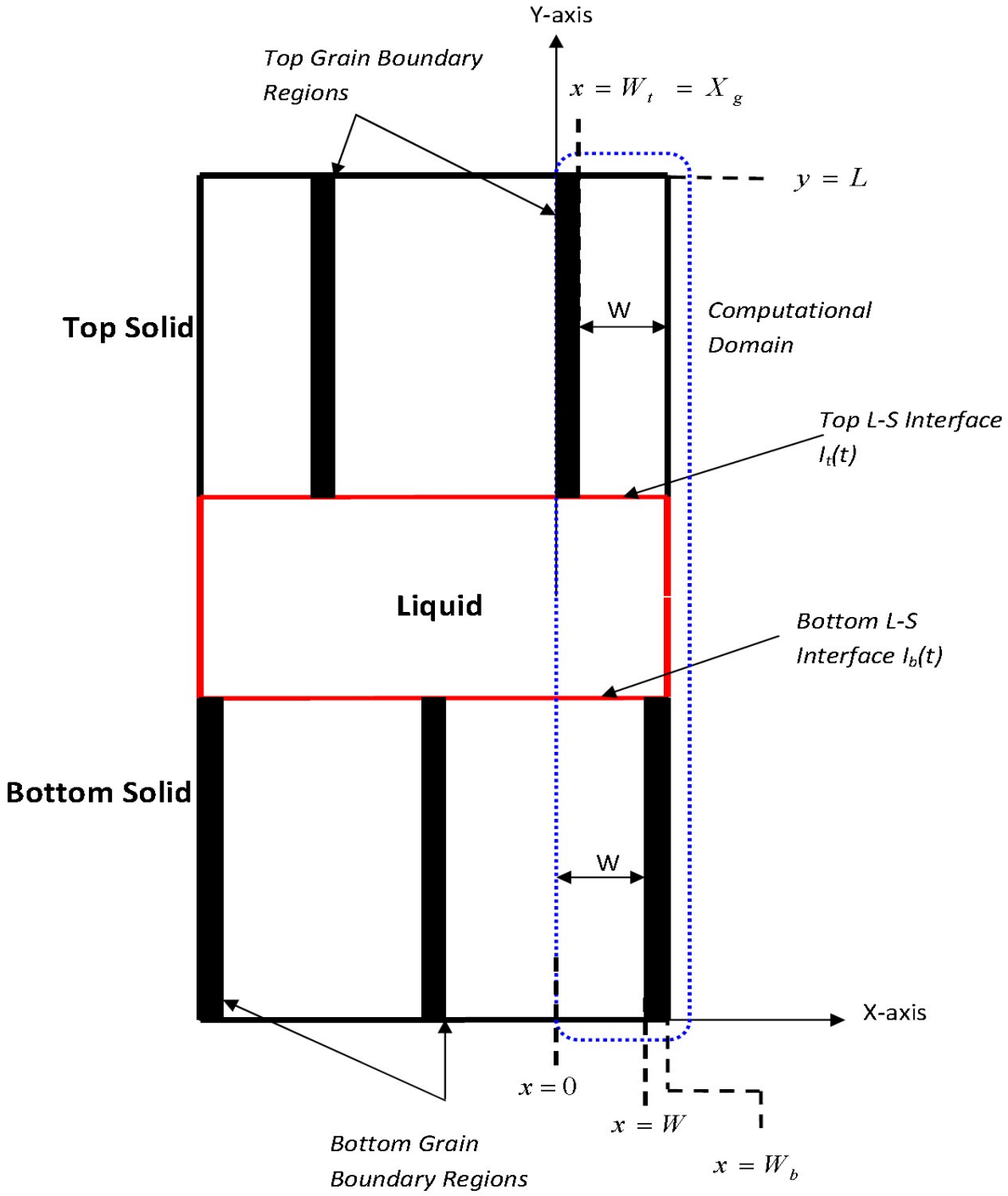

Figure 4. 1: Schematic representation of the problem and definition of the computational domain for simulation of TLP bonding in polycrystalline materials

$$\frac{\partial C(x,y,t)}{\partial t} = \frac{\partial}{\partial x}\left(D_l(C(x,y,t))\frac{\partial C(x,y,t)}{\partial x}\right) + \frac{\partial}{\partial y}\left(D_l(C(x,y,t))\frac{\partial C(x,y,t)}{\partial y}\right)$$

$$I_b(t) < y < I_t(t),\ 0 < x < W_b \qquad (4.1.2)$$

$$\frac{\partial C(x,y,t)}{\partial t} = \frac{\partial}{\partial x}\left(D_{s\_t}(C(x,y,t))\frac{\partial C(x,y,t)}{\partial x}\right) + \frac{\partial}{\partial y}\left(D_{s\_t}(C(x,y,t))\frac{\partial C(x,y,t)}{\partial y}\right)$$

$$I_t(t) < y < L,\ W_t < x < W_b \qquad (4.1.3)$$

where L, W, W_t and W_b represent the dimensions shown in Figure 4.1. D_{s_b}, D_{s_t} and D_l represent the diffusivities in bottom solid, top solid and liquid phases, respectively. I_b and I_t represent the bottom and top liquid-solid interface respectively.

Equations 4.1.4 and 4.1.5 express the solute diffusion in the grain boundaries present in the bottom and top solid phases

$$\frac{\partial C_{g\_b}}{\partial t} = -2.\frac{D_{s\_b}}{X_{g\_b}}.\left(\frac{\partial C_{s\_b}}{\partial x}\right)_{x=X_{g\_b}/2} + D_{g\_b}.\frac{\partial^2 C_{g\_b}}{\partial y^2}$$

$$0 < y < I_b(t)\ ,\ W < x < W_b \qquad (4.1.4)$$

$$\frac{\partial C_{g\_t}}{\partial t} = -2.\frac{D_{s\_t}}{X_{g\_t}}.\left(\frac{\partial C_{s\_t}}{\partial x}\right)_{x=X_{g\_t}/2} + D_{g\_t}.\frac{\partial^2 C_{g\_t}}{\partial y^2}$$

$$I_t(t) < y < L\ ,\ 0 < x < W_t \qquad (4.1.5)$$

where X represent the widths of the grain boundary, C represent the concentration and D represent the diffusion coefficient. Subscripts g_t and g_b represent the grain boundaries at the top and bottom solid phases respectively.

For quadrilateral elements, interpolation functions are introduced for every element such that:

$$N_1(m,n) = \frac{1}{4}(1-m)(1-n)$$
$$N_2(m,n) = \frac{1}{4}(1+m)(1-n)$$
$$N_3(m,n) = \frac{1}{4}(1+m)(1+n)$$
$$N_4(m,n) = \frac{1}{4}(1-m)(1+n)$$

where m and n are the nodal values for each element expressed in natural coordinates as shown in Figure 4.2. Expressing the interpolation functions in natural coordinates instead of physical coordinates is much simpler algebraically since the integrands are relatively simple polynomials and the integration limits when integrating over the area of the element are -1 and +1 [96].

By using the Galerkin finite element method, the introduction of interpolation functions $N_i(x,y)$ over an area A and denoting the phase with subscript p such that $p = l$ in the liquid and $p = s\_t$ in the top solid and $p = s\_b$ in the bottom solid, equations 4.1.1-4.1.3 can be expressed as follows [96]:

$$\iint_A N_i(x,y)\left\{\frac{\partial}{\partial x}\left(D_p^x \frac{\partial C}{\partial x}\right)+\frac{\partial}{\partial y}\left(D_p^y \frac{\partial C}{\partial y}\right)-\frac{\partial C}{\partial t}\right\}dA = 0 \qquad (4.1.6)$$

The diffusion term in Equation (4.1.6) can then be expressed as:

$$\iint_A \left\{\frac{\partial}{\partial x}\left(D_p^x \frac{\partial C}{\partial x}\right)N_i+\frac{\partial}{\partial y}\left(D_p^y \frac{\partial C}{\partial y}\right)N_i\right\}dA = -\iint_A\left(\frac{\partial J_x}{\partial x}N_i+\frac{\partial J_y}{\partial y}N_i\right)dA$$

(4.1.7)

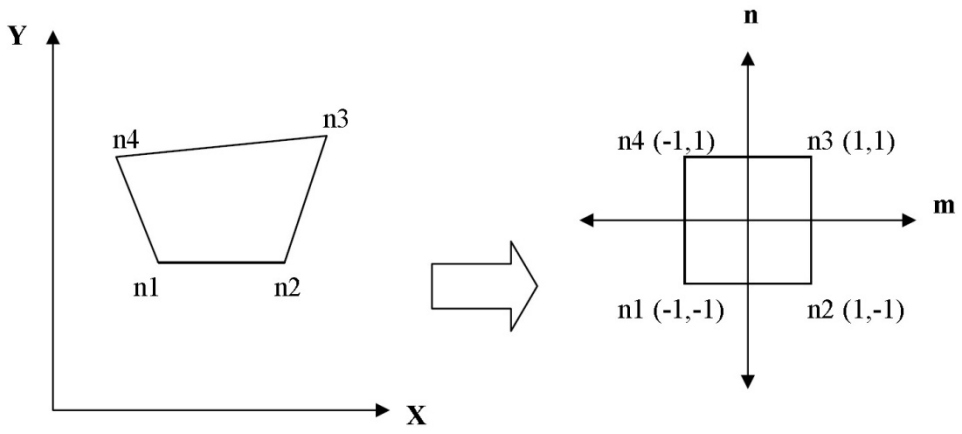

Figure 4. 2: Transformation from physical to natural coordinates for a quadrilateral element

where J_x and J_y represent the flux of diffusing solute in the x and y dimensions, respectively.

The integration of the x-axis term $\iint_A \left(\frac{\partial J_x}{\partial x} N_i \right) dA$ by parts yields the following equation:

$$\int_{y1}^{y2} J_x N_i \Big|_{x1}^{x2} dy - \iint_A J_x \frac{\partial N_i}{\partial x} dA = \iint_A \left(\frac{\partial J_x}{\partial x} N_i \right) dA$$

where the integrand $\int_{y1}^{y2} J_x N_i \Big|_{x1}^{x2} dy$ expresses the weighted value of the solute concentration flux in the x-axis. Assuming diffusion to be independent of the solute concentrations, this equation can then be expressed as:

$$\oint_S J_x N_i dS + \iint_A D_p^x \frac{\partial C}{\partial x} \frac{\partial N_i}{\partial x} dA = \iint_A \left(\frac{\partial J_x}{\partial x} N_i \right) dA \qquad (4.1.8)$$

On the y-axis the same procedure can be applied which yields:

$$\oint_S J_y N_i dS + \iint_A D_p^y \frac{\partial C}{\partial y} \frac{\partial N_i}{\partial y} dA = \iint_A \left(\frac{\partial J_y}{\partial y} N_i \right) dA \qquad (4.1.9)$$

Combining both equations and substituting into Equation 4.1.6 yields the following diffusion equation:

$$\iint_A \left(D_p^x \frac{\partial C}{\partial x} \frac{\partial N_i}{\partial x} + D_p^y \frac{\partial C}{\partial y} \frac{\partial N_i}{\partial y} \right) dA + \iint_A \left(N_i \frac{\partial C}{\partial t} \right) dA = -\oint_S \left(J_x + J_y \right) N_i . dS$$

(4.1.10)

By using the relation $C(x,y) = \sum_{i}^{M} N_i(x,y)C_i = [N][C]$, where M represent the number of nodes per element, the above equation can be expressed in matrix forms as follows:

$$\iint_A \left(D_p^x \left[\frac{\partial N}{\partial x}\right]^T \left[\frac{\partial N}{\partial x}\right] + D_p^y \left[\frac{\partial N}{\partial x}\right]^T \left[\frac{\partial N}{\partial x}\right] \right) \{C_p\} dA + \iint_A [N]^T [N] \left\{ \overset{*}{C}_p \right\} dA = -\oint_S J_s [N]^T .dS \tag{4.1.11}$$

where T denotes the transpose of the matrix. Numerical integration can be done by using the two dimensional Gaussian quadrature method which has the following form:

$$\int_{-1}^{1}\int_{-1}^{1} w_i w_k f(m,n) \approx \sum_{i=1}^{r}\sum_{k=1}^{u} f(m_i, n_k)$$

w_i and w_k are weights at the integration points, and $f(m,n)$ is the function to be integrated over an element expressed in its natural coordinates m and n. The terms r and u represent the total number of integration points per natural coordinate. In this work, numerical integration is done using 6x6 integration points for every quadrilateral element.

The diffusion equations in the liquid and solid phases, Equation 4.1.11, can be expressed in global matrix form:

$$[K]\{C\} + [P]\left\{ \overset{*}{C} \right\} = \{F\}$$

The $[K]$ term is the global stiffness matrix, $[P]$ is the global capacitance matrix and $\{F\}$ is the global force matrix and $\left\{ \overset{*}{C} \right\}$ is the partial differential for the nodal concentrations with respect to

time. The use of an implicit scheme to solve this equation yields the following equations in the bottom solid, liquid and top solid phases, respectively, expressed in their global matrix form:

$$\{C_{s\_b}\}^{j+1} = inv\left(\Delta t.[K_{s\_b}] + [P_{s\_b}]\right)\left(\Delta t\{F_{s\_b}\} + [P_{s\_b}]\{C_{s\_b}\}^{j}\right)$$

$$0 < y < I_b(t)\ ,\ 0 < x < W \qquad (4.1.12)$$

$$\{C_{l}\}^{j+1} = inv\left(\Delta t.[K_{l}] + [P_{l}]\right)\left(\Delta t\{F_{l}\} + [P_{l}]\{C_{l}\}^{j}\right)$$

$$I_b(t) < y < I_t(t), 0 < x < W_b \qquad (4.1.13)$$

$$\{C_{s\_t}\}^{j+1} = inv\left(\Delta t.[K_{s\_t}] + [P_{s\_t}]\right)\left(\Delta t\{F_{s\_t}\} + [P_{s\_t}]\{C_{s\_t}\}^{j}\right)$$

$$I_t(t) < y < L\ ,\ W_t\ < x < W_b \qquad (4.1.14)$$

Where subscripts s_b, s_t and l represent the bottom solid, top solid and liquid phase, respectively. Δt is the time step, j is the current time and $j+1$ is the future time.

A similar finite element formulation procedure as outlined above can be applied to equations 4.1.4 and 4.1.5 which would yield:

$$\{C_{g\_b}\}^{j+1} = inv\left(\Delta t.[K_{g\_b}] + [P_{g\_b}]\right)$$
$$.\left(\Delta t\{F_{g\_b}\} + \frac{4.\Delta t.D_{s\_b}}{X_{g\_b}^{2}}[P_{g\_b}]\{C_{s\_b}\}^{j+1} + [P_{g\_b}]\{C_{g\_b}\}^{j}\right)$$

$$0 < y < I_b(t)\ ,\ W\ < x < W_b \qquad (4.1.15)$$

$$\{C_{g\_t}\}^{j+1} = inv(\Delta t.[K_{g\_t}] + [P_{g\_t}])$$
$$.\left(\Delta t\{F_{g\_t}\} + \frac{4.\Delta t.D_{s\_t}}{X_{g\_b}^{2}}[P_{g\_t}]\{C_{s\_t}\}^{j+1} + [P_{g\_t}]\{C_{g\_t}\}^{j} \right)$$

$$I_t(t) < y < L \ , \ 0 < x < W_t \quad (4.1.16)$$

Where subscripts g_b, g_t represent the grain boundary regions at the bottom solid and top solid phases, respectively, and X represent the width of the grain boundary region. The $[K]$ term is the global stiffness matrix, $[P]$is the global capacitance matrix and $\{F\}$ is the global force matrix and $\{C\}$ is the nodal concentration vector.

4.1.3 Interfacial Migration due to Bulk Lattice Diffusion

The migration of the liquid-solid interface can be described by the following equation [95]:

$$(C_l^0 - C_s^0)V = \left\{ -D_l.\left(\frac{\partial C_l}{\partial n}\right) + D_s.\left(\frac{\partial C_s}{\partial n}\right) \right\}$$

where V is the velocity of the interface I in the direction normal to the interface. C_l^0 is the liquidus equilibrium concentration, C_s^0 is the solidus equilibrium concentration, and $\left(\frac{\partial}{\partial n}\right)$ is the directional differential normal to the interface. Patel et al. [97] transformed this equation which can be adapted to the top and bottom interfaces, respectively, as shown in equations 4.1.17 and 4.1.18.

$$\left(C^0_{l\_t} - C^0_{s\_t}\right).\frac{\partial I}{\partial t} = \left\{-D_l.\left(\frac{\partial C_l}{\partial y}\right)_{y=I\_t-} + D_{s\_t}.\left(\frac{\partial C_s}{\partial y}\right)_{y=I\_t+}\right\}.\left\{1+\left(\frac{\partial I}{\partial x}\right)^2\right\} \qquad (4.1.17)$$

$$\left(C^0_{l\_b} - C^0_{s\_b}\right).\frac{\partial I}{\partial t} = \left\{D_l.\left(\frac{\partial C_l}{\partial y}\right)_{y=I\_b+} - D_{s\_b}.\left(\frac{\partial C_s}{\partial y}\right)_{y=I\_b-}\right\}.\left\{1+\left(\frac{\partial I}{\partial x}\right)^2\right\} \qquad (4.1.18)$$

The liquid-solid interface is assumed to be sharp, or infinitesimally thin. To track the interface location along the y-axis equation 4.1.17 and 4.1.18 can be solved using the implicit finite difference method which yields the following equations for the future top and bottom interface locations.

$$I_t{}^{j+1}(x,y) = I_t{}^{j}(x,y) + \frac{\Delta t}{C^0_{l\_t} - C^0_{s\_t}}\left\{-D_l.\left(\frac{C^0_{l\_t} - C_l(x,y-1,t)}{\Delta y_{l\_t}}\right) + D_{s\_t}.\left(\frac{C_{s\_t}(x,y+1,t) - C^0_{s\_t}}{\Delta y_{s\_t}}\right)\right\}$$
$$.\left\{1+\left(\frac{I_t{}^{j+1}(x+1,y) - I_t{}^{j+1}(x-1,y)}{2.\Delta x}\right)^2\right\} \qquad (4.1.19)$$

$$I_b{}^{j+1}(x,y) = I_b{}^{j}(x,y) + \frac{\Delta t}{C^0_{l\_b} - C^0_{s\_b}}\left\{D_l.\left(\frac{C^0_{l\_b} - C_l(x,y+1,t)}{\Delta y_{l\_b}}\right) - D_{s\_b}.\left(\frac{C_{s\_b}(x,y-1,t) - C^0_{s\_b}}{\Delta y_{s\_b}}\right)\right\}$$
$$.\left\{1+\left(\frac{I_b{}^{j+1}(x+1,y) - I_b{}^{j+1}(x-1,y)}{2.\Delta x}\right)^2\right\} \qquad (4.1.20)$$

where Δx, Δy_{l_t}, Δy_{l_b}, Δy_{s_b} and Δy_{s_t} are the distances in the x and y directions between the nodes around the top and bottom liquid-solid interfaces for every interfacial node $I_b{}^{j}(x,y)$ and $I_t{}^{j}(x,y)$ at every time step Δt.

Interfacial migration in the top and bottom interfaces due to diffusion in the bulk material can be expressed as:

$$\Delta I_{bulk\_t}^{j+1} = I_t^{j+1} - I_t^j \tag{4.1.21}$$

$$\Delta I_{bulk\_b}^{j+1} = I_b^{j+1} - I_b^j \tag{4.1.22}$$

Since the concentration gradients in the solid and liquid phases are highest near the liquid-solid interface, a variable mesh density is used where the density of the mesh is increased in the liquid and solid phases near the interface. This is done to increase the accuracy of the numerical results and reduce computational time. For every estimate of the interfacial nodes at time t, the mesh automatically adapts to the shape of the interface and discretizes the domain accordingly without restricting the motion of the interfaces.

4.1.4 Formulation of Interfacial Curvature caused by Grain Boundary Grooving

Grain boundary grooving will occur when a grain boundary intercept the liquid-solid interface. An interfacial migration of ΔI_{gb} at the point of intersection will cause a change in free energy that is given by [98]:

$$\Delta G \approx (-E_{gb} + 2E_s \cos\theta)\Delta I_{gb} \tag{4.1.23}$$

where E_{gb} is the grain boundary energy, and E_s is the liquid-solid interface energy.

The change in the free energy per the number of moles of solute required to produce the interfacial shift would result in an increased chemical potential of the solute at the interface, i.e.:

$$\Delta\mu = \frac{\Delta G}{\Delta n} \tag{4.1.24}$$

Substituting Equation 4.1.24 into 4.1.23 yields:

$$\Delta\mu = \frac{(-E_{gb} + 2E_s\cos\theta)\Delta I_{gb}}{\Delta n} = \frac{(-E_{gb} + 2E_s\cos\theta)V}{(C_l^0 - C_s^0)\delta} \tag{4.1.25}$$

where V is the molar volume and δ represents the width over which the chemical potential of the solute is influenced by the grain boundary which is taken to be equal to the grid size in the x direction Δx. The increased chemical potential constitutes additional driving force for the diffusion of the solute. To incorporate this effect into the model, the chemical potential change can be expressed as [99]:

$$\Delta\mu = -\frac{E_s V}{r.(C_l^0 - C_s^0)} \tag{4.1.26}$$

and the solidus and liquidus solubilities at the top interface can be approximated as [95]:

$$C_{l\_t}^{curv} \approx C_{l\_t}^0.\left(1 + \frac{\Delta\mu_t}{RT}\right) \tag{4.1.27}$$

$$C_{s\_t}^{curv} \approx C_{s\_t}^0.\left(1 + \frac{\Delta\mu_t}{RT}\right) \tag{4.1.28}$$

Similarly, at the bottom interface:

$$C_{l\_b}^{curv} \approx C_{l\_b}^{0}.\left(1+\frac{\Delta\mu_b}{RT}\right) \tag{4.1.29}$$

$$C_{s\_b}^{curv} \approx C_{s\_b}^{0}.\left(1+\frac{\Delta\mu_b}{RT}\right) \tag{4.1.30}$$

The excess chemical potential along the liquid-solid interface causes diffusional flow along the liquid-solid interface and, consequently, contributes to migration of the liquid-solid interface, which can be described by [91]:

$$\frac{\partial I}{\partial t}=\frac{D_i C_i w}{R.T(C_l^0-C_s^0)}.\frac{\partial}{\partial x}\left\{\left[1+\left(\frac{\partial I}{\partial x}\right)^2\right]^{-1/2}.\frac{\partial\Delta\mu}{\partial x}\right\} \tag{4.1.31}$$

where D_i is the diffusion coefficient along the liquid-solid interface, C_i is the composition of the liquid-solid interface, and w is the thickness of the liquid-solid interface. The composition C_i is taken as:

$$C_i=\frac{C_l^0+C_s^0}{2} \tag{4.1.32}$$

Let

$$Z=\frac{D_i C_i w}{R.T(C_l^0-C_s^0)} \tag{4.1.33}$$

Applying the product rule for differentiation, Equation 4.1.26 can be expressed as:

$$\frac{\partial I}{\partial t}=Z\left\{\frac{\partial}{\partial x}\left[\left(1+\left(\frac{\partial I}{\partial x}\right)^2\right)^{-1/2}\right].\frac{\partial\Delta\mu}{\partial x}+\left(1+\left(\frac{\partial I}{\partial x}\right)^2\right)^{-1/2}.\frac{\partial^2\Delta\mu}{\partial x^2}\right\} \tag{4.1.34}$$

After differentiation this equation becomes:

$$\frac{\partial I}{\partial t} = Z\left\{\frac{-\left(\frac{\partial I}{\partial x}\right)\left(\frac{\partial^2 I}{\partial x^2}\right)\left(\frac{\partial \Delta\mu}{\partial x}\right)}{\left(1+\left(\frac{\partial I}{\partial x}\right)^2\right)^{3/2}} + \left(1+\left(\frac{\partial I}{\partial x}\right)^2\right)^{-1/2}.\frac{\partial^2 \Delta\mu}{\partial x^2}\right\} \tag{4.1.35}$$

Upon simplification, the equation becomes:

$$\frac{\partial I}{\partial t} = \left(\frac{Z}{\left(1+\left(\frac{\partial I}{\partial x}\right)^2\right)^{1/2}}\right).\left\{\frac{-\left(\frac{\partial I}{\partial x}\right)}{1+\left(\frac{\partial I}{\partial x}\right)^2}\left(\frac{\partial^2 I}{\partial x^2}\right)\left(\frac{\partial \Delta\mu}{\partial x}\right) + \frac{\partial^2 \Delta\mu}{\partial x^2}\right\} \tag{4.1.36}$$

In its finite difference form it becomes:

$$\Delta I_{curv}^{j+1}(x,y) = \frac{Z.\Delta t}{\sqrt{1+R}}$$
$$\left\{\left(\frac{-R}{1+(R)^2}\right)\left(\frac{I^{j+1}(x+1,y)-2I^{j+1}(x,y)+I^{j+1}(x-1,y)}{\Delta x^2}\right)(M)\right\} \tag{4.1.37}$$
$$\left\{+\left(\frac{\Delta\mu(x+1,y)-2\Delta\mu(x,y)+\Delta\mu(x-1,y)}{\Delta x^2}\right)\right\}$$

where $R = \frac{I^{j+1}(x+1,y)-I^{j+1}(x-1,y)}{2.\Delta x}$ and $M = \frac{\Delta\mu(x+1,y)-\Delta\mu(x-1,y)}{2\Delta x}$

This is solved for both the upper and lower interfaces to yield interfacial migration due to curvature $\Delta I_{curv\_t}^{j+1}$ and $\Delta I_{curv\_b}^{j+1}$.

The future location for the bottom and top liquid-solid interface for a time step Δt is then given by:

$$I_b^{j+1} = I_b^j + \Delta I_{bulk\_b}^{j+1} + \Delta I_{curv\_b}^{j+1} \tag{4.1.38}$$

$$I_t^{j+1} = I_t^j + \Delta I_{bulk\_t}^{j+1} + \Delta I_{curv\_t}^{j+1} \tag{4.1.39}$$

4.1.5 Implementation

The current numerical simulation model describes diffusion-controlled isothermal phase change under the following assumptions:

- there is local equilibrium at the liquid-solid interface;
- atomic diffusion can be described by Fick's second law of diffusion;
- the molar volume is assumed constant irrespective of phase or concentration;
- diffusivity of the MPD solute is independent of concentration in each phase;
- grain boundaries are assumed perpendicular to the liquid-solid interface; and
- grain boundaries are assumed stationary.

The initial and boundary conditions employed are as follows:

$$C_l = C_F \qquad \text{for } t = 0,\ I_b(x,y,t) < y < I_t(x,y,t)$$

$$C_{s\_b} = C_{M\_b} \qquad \text{for } t = 0,\ 0 < y < I_b(x,y,t)$$

$C_{s\_t} = C_{M\_t}$ for $t = 0,\ I_t(x,y,t) < y < L$

$I_t = H_b + h$ for $t = 0$

$I_b = H_b$ for $t = 0$

$\left(\frac{\partial C}{\partial y}\right)_{s\_b} = \left(\frac{\partial C}{\partial y}\right)_{g\_b} = 0$ for $t > 0,\ y = 0$

$\left(\frac{\partial C}{\partial y}\right)_{s\_t} = \left(\frac{\partial C}{\partial y}\right)_{g\_t} = 0$ for $t > 0,\ y = L$

In the absence of grain boundaries:

$C_{l\_b} = C^0_{l\_b}$ for $t \geq 0,\ y = I_b(x,y,t)$

$C_{l\_t} = C^0_{l\_t}$ for $t \geq 0,\ y = I_t(x,y,t)$

$C_{s\_b} = C^0_{s\_b}$ for $t \geq 0,\ y = I_b(x,y,t)$

$C_{s\_b} = C^0_{s\_t}$ for $t \geq 0,\ y = I_t(x,y,t)$

where C_F is the initial MPD solute concentration in the interlayer. C_{M_b} and C_{M_t} are the initial MPD solute concentration in the bottom and top solid phases respectively. H_b is the thickness of the bottom solid, H_t is the thickness of the top solid, h is the initial thickness of the liquid phase and $L = H_b + h + H_t$.

An algorithm that implements an iterative solution method was developed due to the non-linearity of the system of simultaneous equations. The algorithm can be outlined as follows:

1. initialization of the concentrations of the MPD solute in the liquid and solid phases. Also, initialization of the x and y coordinates of the interfaces I_b^j and I_t^j;
2. calculation of the initial estimate of the future interface position I_b^{j+1} and I_t^{j+1} using Equations 4.1.19 and 4.1.20;
3. by using the values for I_b^{j+1} and I_t^{j+1}, the mesh in the liquid and solid phases is adapted to accommodate the new estimate for the interface positions;
4. the finite element equations are solved to calculate the future concentrations in the liquid and solid phases by using equations 4.1.12-4.1.14;
5. the finite element equations are solved to calculate the future concentrations along the grain boundaries by using equations 4.1.15 and 4.1.16;
6. the future interface positions I_b^{j+1} and I_t^{j+1} are calculated using equation 4.1.19 and 4.1.20;
7. steps 3 to 7 are repeated until successive estimates of the future interface position I_b^{j+1} and I_t^{j+1} differ by less than some user defined tolerance;
8. the interfacial migration $\Delta I_{bulk\_t}^{j+1}$ and $\Delta I_{bulk\_b}^{j+1}$ are calculated;
9. using the converged estimates for the interface positions obtained in step 7, calculate the interfacial migration $\Delta I_{curv\_t}^{j+1}$ and $\Delta I_{curv\_b}^{j+1}$ due to grooving using equation 4.1.37; and finally
10. I_b^{j+1} and I_t^{j+1} are calculated using equations 4.1.38 and 4.1.39.

In the absence of grain boundaries, i.e. for SX, steps 5, 8, 9 and 10 can be omitted. The converged answer corresponds to a solution of the fully implicit set of discretized equations at some time step Δt. The coordinates for the interfacial nodes are then updated along with the concentrations at each finite element node in the solid and liquid phases and the algorithm is applied again at the next time step. The computer code implementing this algorithm is written in C++ and Matlab. It has been found that successive estimates of interface positions at each time step do indeed converge to a fixed value. Results from the model and comparisons with experimental and published data are discussed in the next section.

4.1.6 Validation of the Numerical Model

Using a Ni-B binary system and the process parameters listed in Table 4.1, spatial convergence tests were carried out by varying the mesh density in the SX crystal solid phase from 40 to 120 elements. The predicted interfacial migration with time was found to be independent of spatial discretization as the mesh density is increased, as shown in Figure 4.3. With the inclusion of grain boundaries in polycrystalline solids, the predicted interfacial morphology was also found to be independent of spatial discretization with increasing mesh density from 300 to 500 elements, as shown in Figure 4.4. Further increase in spatial resolution was found to have no significant effect on the accuracy of the solution, which indicates that truncation errors are mainly caused by coarse discretization of time. Time discretization tests were also performed by varying time step from 10 sec to 2000 sec. Figure 4.5 shows that the predicted liquid-solid interface location becomes independent of time discretization with decreasing time step size.

Table 4. 1: Process parameters used for the numerical simulations.

Parameter	Symbol	Value
Binary System	---	Ni-B
Bonding Temperature	T (^{o}C)	1100
Filler Full Thickness	h (cm)	0.008
Base Metal Thickness	H (cm)	0.6
Grain Size (microns)	w (cm)	0.004-0.2
Activation Energy for Diffusion in Solid	$Q_{\_bulk}$ (kJ/mol)	226
Solid Diffusion Frequency Factor	D_{o_bulk} (m^2/sec)	0.14
Diffusivity in Liquid	D_{Liq_bulk} (m^2/sec)	5E-9
Initial MPD Concentration in Liquid	C_F (at.%)	17
Initial MPD Concentration in Solid	C_m (at.%)	0
Solidus Solubility	C_s^0 (at.%)	0.294
Liquidus Solubility	C_l^0 (at.%)	16.5
Interface Thickness	z (cm)	3E-8
Grain Boundary Width	(cm)	5E-8
Surface Energy	E_s (J/m^2)	0.486
Grain Boundary Energy	E_g (J/m^2)	0.848
GB Solidus Diffusivity	$D_{\_g}$ (m^2/sec)	$1\text{-}10^5$ D_s
Molar Volume	V_molar (cm^3/mol)	6.6

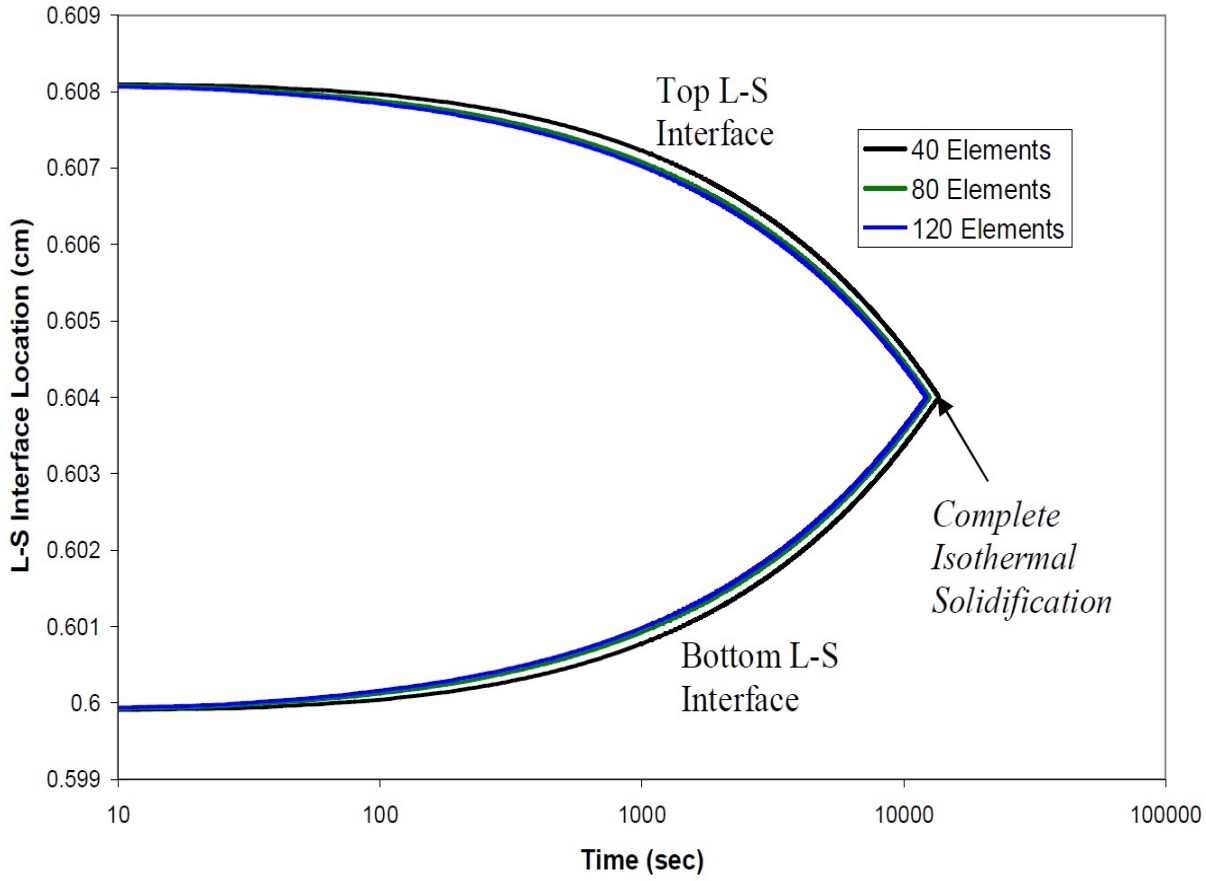

Figure 4. 3: Effect of mesh density on predicted liquid-solid interface migration during TLP bonding of two similar single crystal substrates

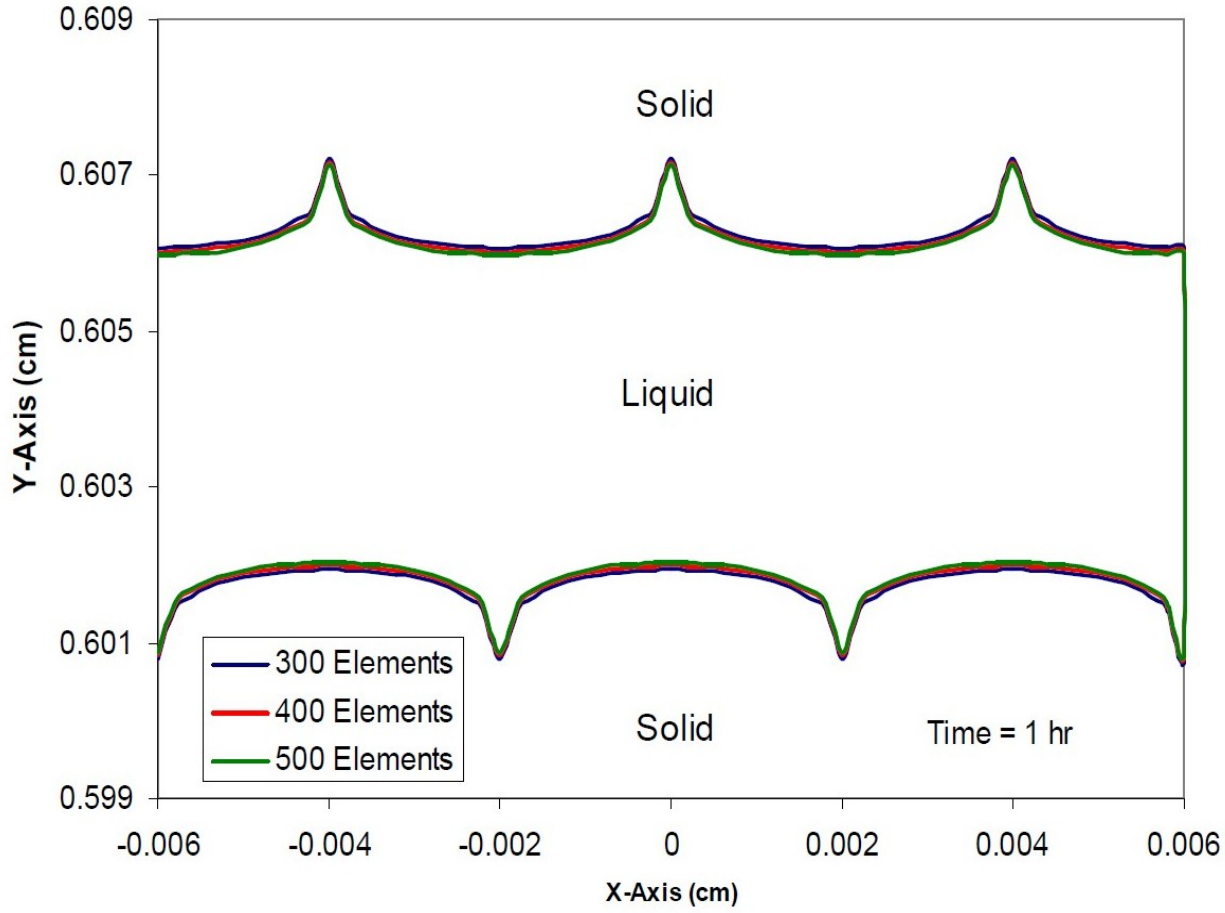

Figure 4. 4: Effect of mesh density on simulated joint microstructure during TLP bonding of two similar polycrystalline substrates

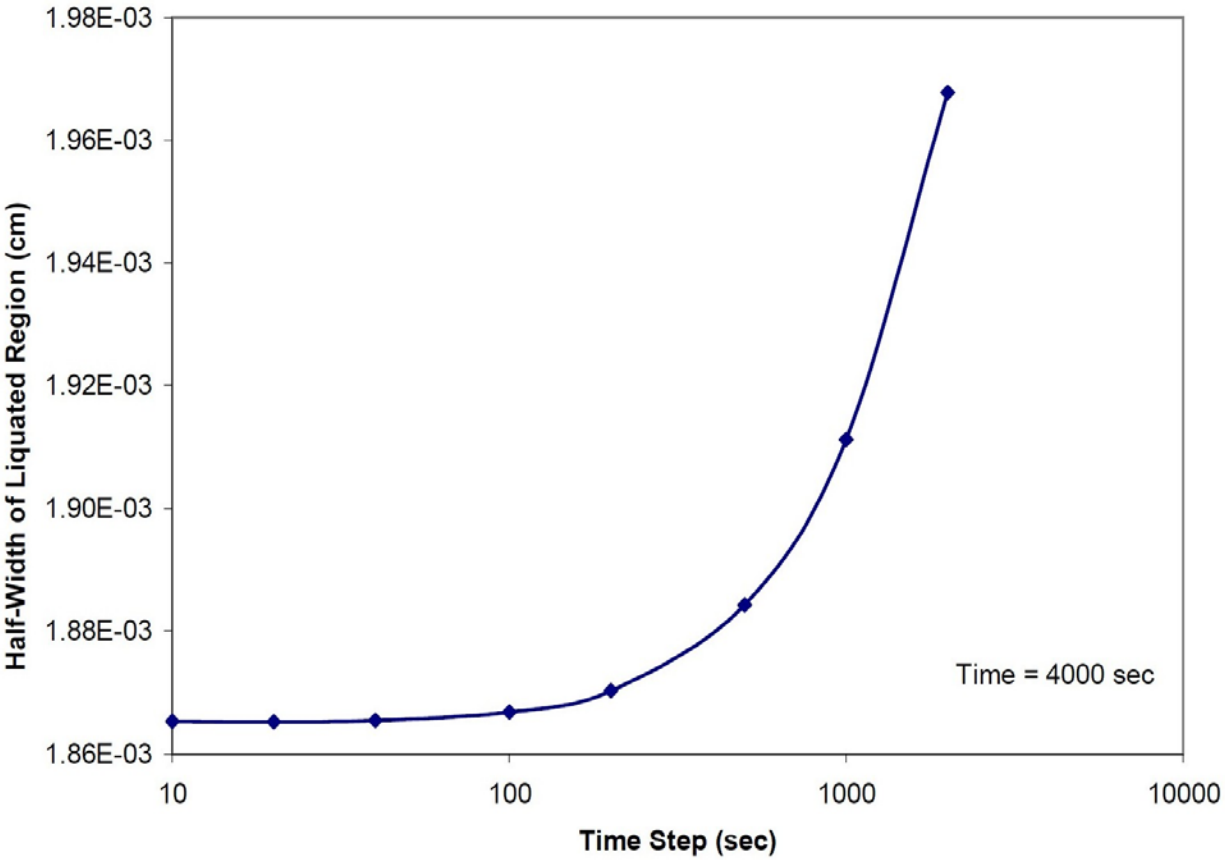

Figure 4. 5: Variation of predicted interface location with simulation time step

The results show that a truncation error caused by the use of a coarse time step of 2000 sec resulted in a predicted interface location that is only 0.6 μm off the converged solution. The results also indicate that the algorithm is first order accurate in time. In fact, decreasing the time step by a factor of two reduced the error from the converged solution by a factor that is slightly greater than two.

To compare the results of the new two dimensional non-symmetric-joint model with existing 1-D and symmetric-joint models, numerical simulations were carried out where grain boundary effects were not incorporated into the model and symmetry was assumed at the centerline of the joint. The output of the present 2-D finite element model is in good quantitative agreement with the experimental data published by Zhou et al. [88] for Ni-P system, as shown in Figure 4.6. The solution is also quantitatively very close to calculated results of models dedicated for 1-D analysis by Illingworth et al. [87] and Zhou et al. [88], which further reinforces the validity of the new 2-D model. Similar to their approach, in the present model, a constant molar volume is assumed, which allows for the calculation of the theoretical maximum liquid layer. This value represents the thickness at which the liquid is diluted to the equilibrium concentration without any diffusion of solute into the solid. The predictions of the present 2-D finite element model and that of Illingworth's et al. [87] do not exceed the theoretical maximum, which is consistent with the fact that they both conserve solute in space and time. When the presence of grain boundaries with non-symmetrical distribution in polycrystalline solid substrates was considered, initial qualitative validation was done by simulating TLP bonding of Ni-based superalloy and pure Ni.

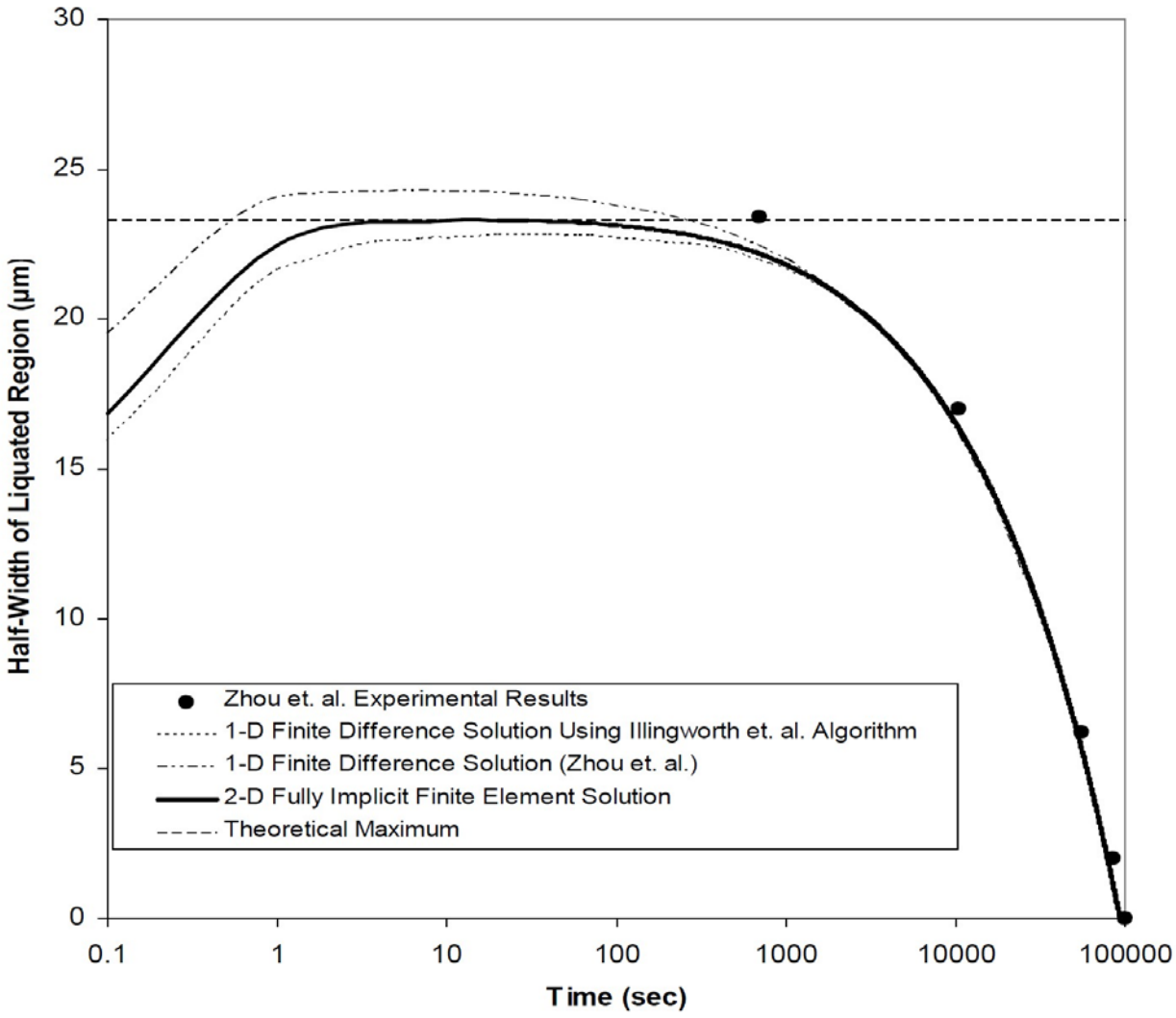

Figure 4. 6: Comparisons between the new 2-D finite element solution and published experimental and theoretical data

The numerically simulated joint microstructure that shows isothermally solidified and residual liquated regions is presented in Figure 4.7. The liquid-solid interface evolved from a relatively flat surface at the initial stage of the process into a rougher surface with grooves along the asymmetrically distributed grain boundaries due to intergranular liquid penetration. The migration morphology of the liquid-solid interface as predicted by the model is consistent with experimentally observed results in pure Ni and a Ni-base superalloy, where interceptions of the grain boundary and liquid-solid interface are not symmetrical (Figures 4.7 and 4.8). A major reported contribution of grain boundaries to the kinetics of diffusion-controlled interfacial migration is by a higher atomic diffusion rate that is possible along intergranular regions compared to lattice bulk diffusion [98]. Even in TLP bonding, this has been suggested as a reason why processing time t_f can be expected to be shorter in fine grain polycrystalline solids, with higher number of grain boundaries compared to coarse grain solids [100, 101]. In the present work, exclusive of the grain boundary grooving mechanism, the sole effect of higher grain boundary diffusivity on the migration of liquid-solid interfaces is simulated by varying the grain boundary diffusivity to be 10 to 1000 time faster than bulk lattice diffusion. As evident in Figure 4.9, the morphology of the migrating liquid-solid interface, particularly at the locations where it intercepts the grain boundary, is inconsistent and contrary to the experimental results. At these locations, the interface migrates away from the solid instead of towards the solid as experimentally observed and predicted by the model when the effects of grain boundary grooving are incorporated. This suggests that rather than merely higher grain boundary diffusivity, a major influence of grain boundaries on interface migration is through an intergranular grooving mechanism, which is consistent with the experimental results obtained by Kokawa et al. [102] and simulation result by Ikeuchi et al. [95].

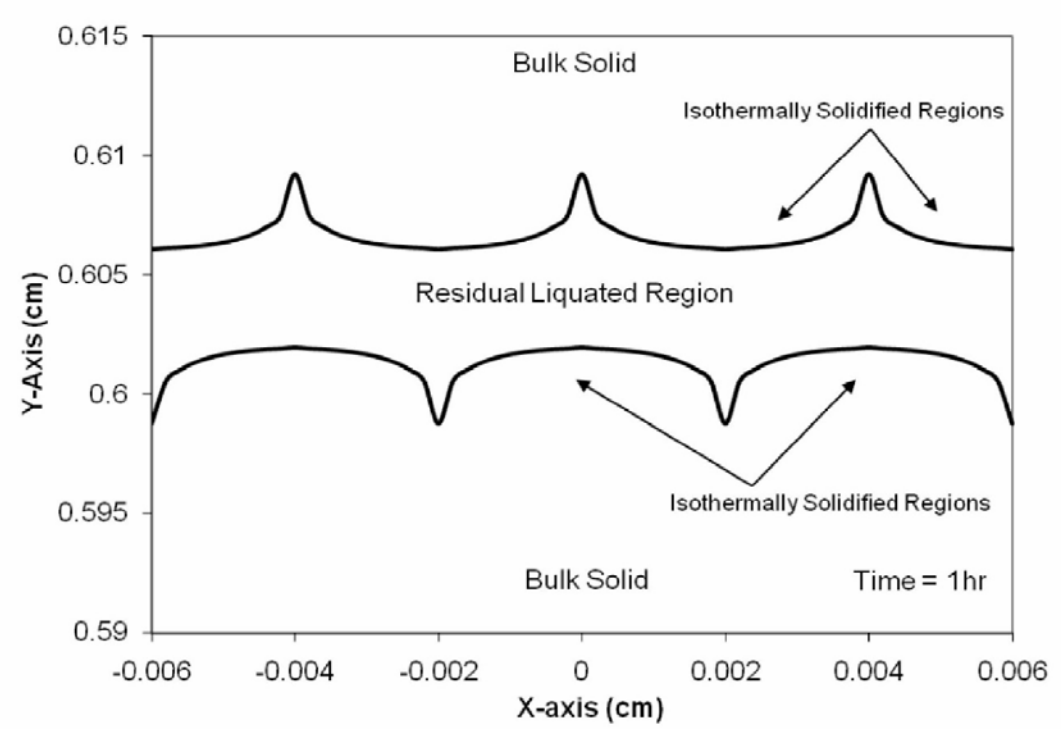

Figure 4. 7: Predicted morphology of residual interlayer liquid based on numerical simulation

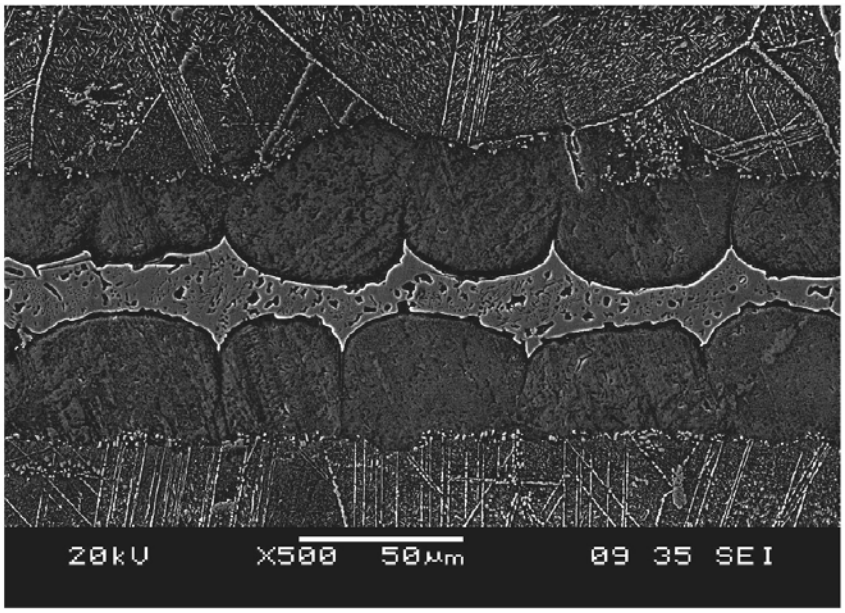

Figure 4. 8: Scanning electron microscopy micrograph of TLP joint in a nickel-base superalloy, showing the morphology of centerline eutectic that formed from residual interlayer liquid.

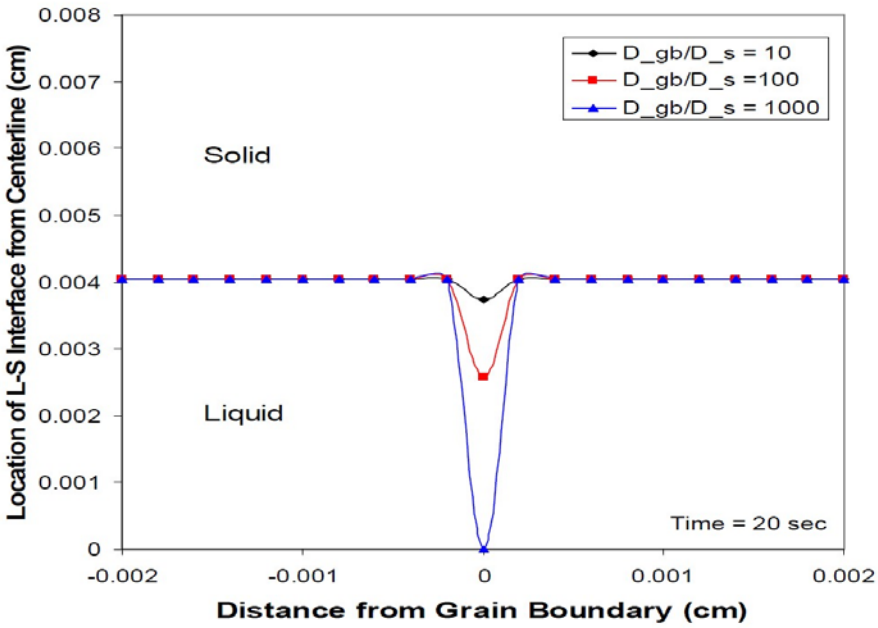

Figure 4. 9: Effect of grain boundary diffusivity on liquid-solid interface morphology without the consideration of grain boundary grooving

4.1.7 Numerical and Experimental Investigation of the Effect of Grain Boundaries on TLP Isothermal Solidification Kinetics

Combining grain boundary grooving and enhanced diffusion due to the resultant curved liquid-solid interface and higher grain boundary diffusivity, simulations were carried out to study the effect of grain boundaries on the extent of diffusion-induced isothermal solidification by comparing polycrystalline substrates with SX substrates. As illustrated in Figure 4.10, the calculation shows that the migration rate of the liquid-solid interface is slightly affected by the presence of grain boundaries. The extent of isothermally solidified region is somewhat, but not considerably, larger in the polycrystalline substrates compared to the case in the SX substrates. Generally, a decrease in grain size of the material results in an increased number of grain boundaries.

Further analysis was performed to evaluate and compare the t_f required to achieve complete isothermal solidification in polycrystalline solids that contain grains of different sizes (150 µm, 500 µm, 2 mm) with that in SXs and the results are shown in Figure 4.11. Interestingly, even though it was stated earlier that grain boundaries can influence the migration rate of the liquid-solid interface, the effect did not translate to significant differences between the values of t_f in the polycrystalline solids with different grain size solids and that of the single crystal substrates. It has been found that the ratio of the grain boundary diffusion coefficient, D_{gb}, to that of the bulk lattice, D_l, is about 10^3 or less within the temperature range $T > 0.5 - 0.75\ T_m$ (where T_m is the equilibrium melting temperature in K) [103].

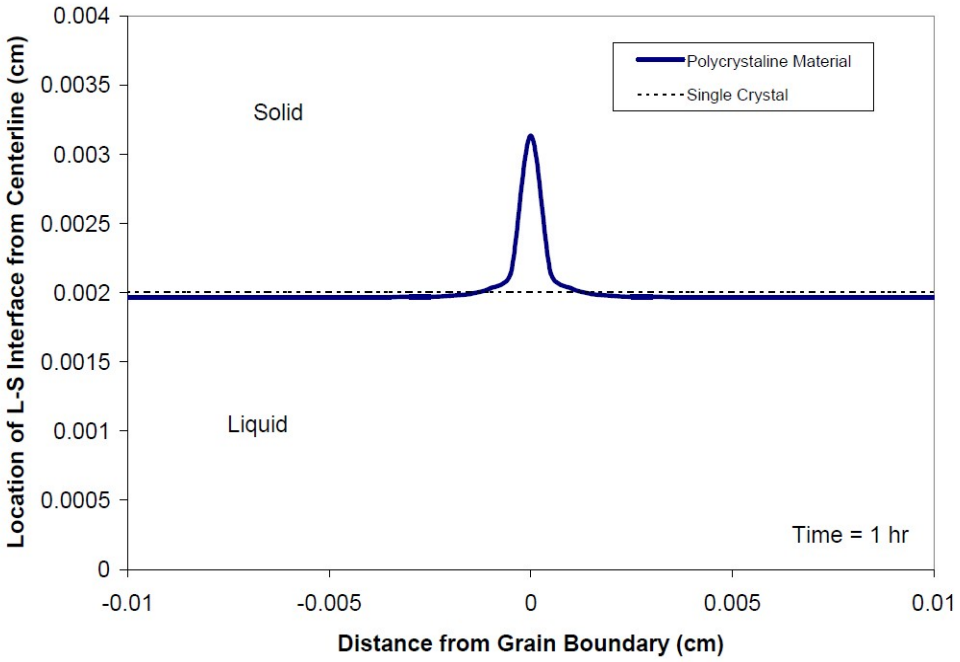

Figure 4. 10: Numerical simulation comparison of L-S interface migration in polycrystalline and single crystal substrates

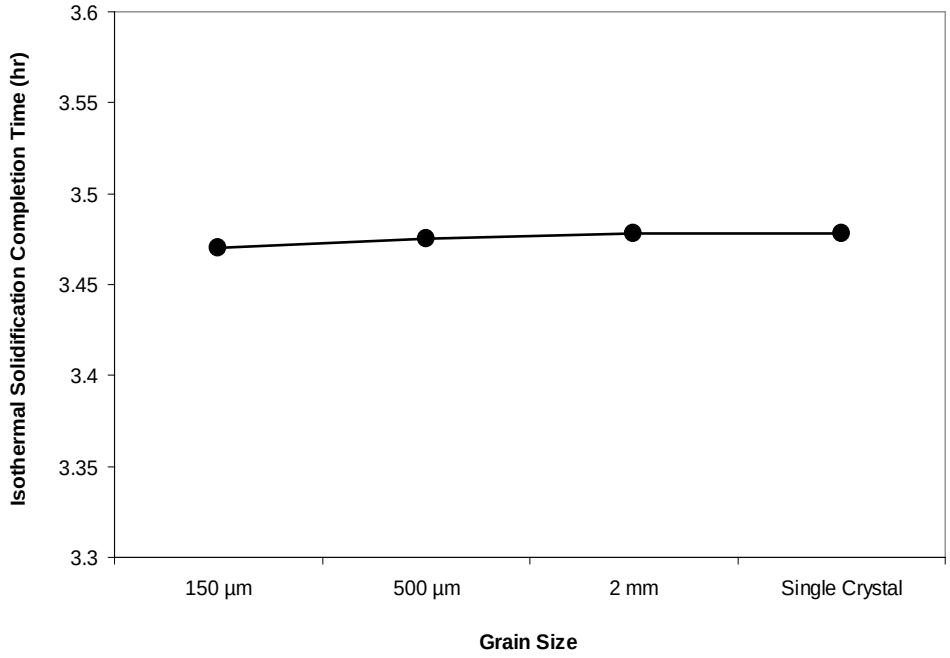

Figure 4. 11: Effect of grain size on predicted isothermal solidification time t_f

TLP bonding temperatures are typically higher than 0.75 T_m. Numerical calculations were performed to evaluate the effect of the increase in the ratio D_g/D_l from 10^2 – 10^5 on time t_f in polycrystalline solids with different grain sizes. The calculated results shown in Figure 4.12 show that an increase in the grain boundary diffusion coefficient does not produce any significant differences in t_f for the different grain size substrates. This is in contrast to the work of Ikeuchi et al. [95], where it was reported that alongside with grain boundary grooving, an increase in grain boundary diffusion coefficient can account for differences in isothermal solidification completion time in solids with different grain sizes.

To experimentally verify the prediction of the present numerical model, TLP bonding of a Ni-base alloy in equiaxed polycrystalline (average grain size ~ 1mm), directionally solidified (DS) polycrystalline (average grain size ~ 3 mm) and SX (no grain boundary) conditions, was performed at 1100^{o}C by using a commercial Ni-Cr-B filler alloy. The time, t_f, required to achieve complete isothermal solidification was observed to be comparable in all the materials, about 3 hrs (Figure 4.13), which is in agreement with the prediction of the present numerical model. This confirms that an increased atomic diffusion rate along grain boundaries in polycrystalline materials has a negligible effect on t_f during the TLP bonding process. In contrast to the effect of grain boundary diffusivity, calculations with the new model suggest that an appreciable increase in solute solubility in the solid at the liquid-solid interface can produce a sizeable decrease in time t_f (Figure 4.14). It is conceivable that a large increase in interfacial curvature may enhance solute solubility and it is generally known that grain boundary curvature decreases with grain size [104].

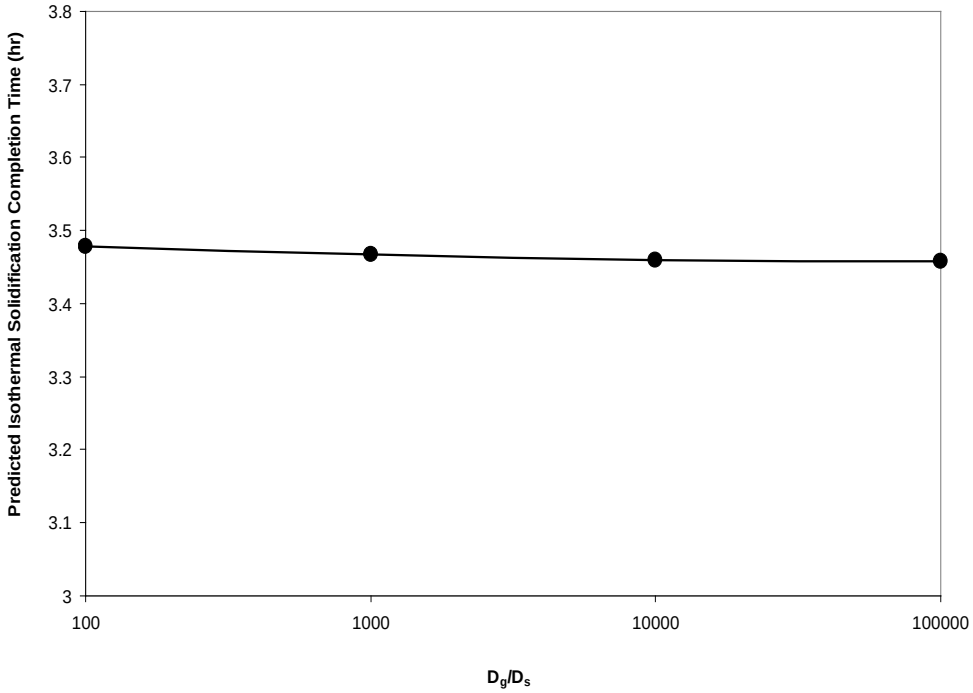

Figure 4. 12: Effect of D_g/D_s ratio on predicted isothermal solidification time t_f

.

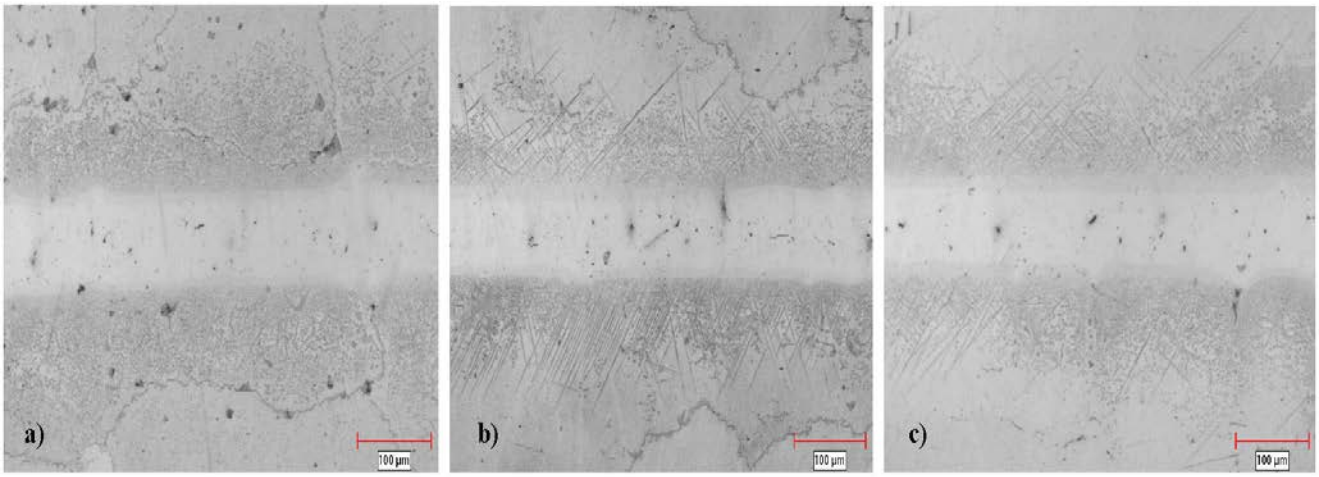

Figure 4. 13: Microstructure of TLP joints produced at 1100^{o}C for 3 hours in (a) Single Crystal (b) Directionally Solidified and (c) Equiaxed IN 738 superalloy substrates

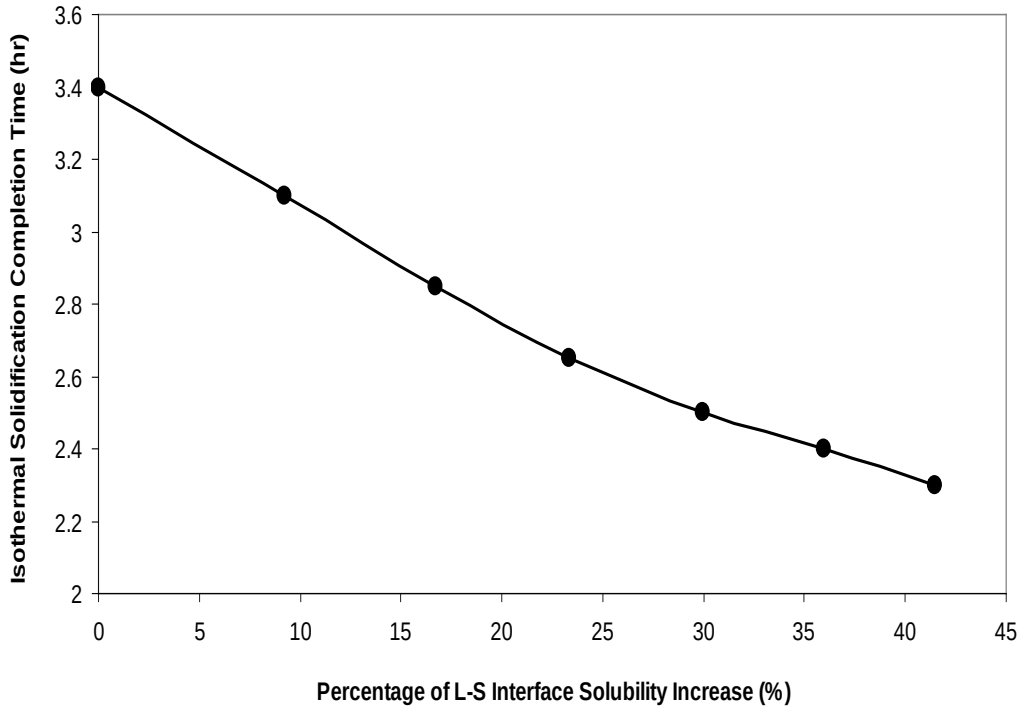

Figure 4. 14: Effect of increased L-S interface solubility on isothermal solidification completion time based on numerical simulations

Accordingly, if the grain size in polycrystalline solids is considerably reduced to a point where an appreciable increase in interfacial solute solubility occurs, due to increased interfacial curvature, then a significant reduction in t_f may ensue. However, this effect could become negligible as the curvature reduces with an increase in grain size, such that the presence or lack of grain boundaries in coarse grain materials, like cast alloys, may not have significant effect on t_f. The TLP bonding technique is commonly used to bond and repair difficult-to-weld cast alloys, particularly cast heat resistant nickel-base superalloys that are used at temperatures above 980^{o}C in aerospace and power generation applications. The recent trend to improve elevated temperature mechanical properties in these alloys involves minimizing grain boundaries through directional solidification manufacturing techniques to produce cast polycrystalline alloys with fewer grain boundaries and SX materials [105]. It has been suggested that the removal of grain boundaries from these materials can considerably increase t_f [100, 101], which can render the application of TLP bonding to these class of materials commercially unappealing. Conversely, however, the results of the new 2-D numerical model developed in this work, and verified experimentally, showed that the effect of grain boundaries on diffusion-controlled solidification during TLP bonding of this class of materials is negligible. Hence, with regard to t_f during TLP bonding, there is no major disincentive with the use of directional solidification casting techniques to produce cast polycrystalline and SX solids.

4.2 Numerical Simulation and Experimental Study to Reduce the Isothermal Solidification Completion Time during TLP Bonding of Single Crystals

4.2.1. Introduction

As previously discussed, an important parameter in the consideration of TLP bonding for commercial applications is the holding time (t_f) required to complete diffusional solidification, which is necessary to prevent the formation of non-equilibrium solidification products that degrade the properties of bonded materials. High temperature is often desired and required for diffusion brazing of SX superalloys not only with the aim to reduce t_f by increased diffusivity, but also because highly alloyed brazing interlayers suitable for these materials have high melting temperatures. In addition, increased temperature generally aids the homogenization of the joint composition and microstructure with the base material, which reduces possibility of formation of detrimental second phases during cooling from bonding temperature or service exposure [106]. Unfortunately t_f during high temperature TLP bonding of SX is typically very long, which often limits the commercial appeal of the technique for industrial applications. One factor that has been suggested as a likely cause of the long t_f in SX alloys is the absence of grain boundaries, since intergranular regions are generally known to be high atomic diffusivity paths, compared to bulk lattice diffusion. Nevertheless, as discussed in Section 4.1 of this thesis, this study has shown that long t_f in SX superalloys cannot be attributed to the grain boundary diffusion effect. The problem is further complicated when t_f exhibits an anomalous reverse behavior by increasing with temperature. The cause of this anomalous increase in t_f is not yet ascertained,

which is crucial to developing ways to minimize the processing time required to prevent formation of microconstituents that are detrimental to brazed joint properties. Hence, as the main objective of the present work, the newly developed numerical model is used to study and understand the cause of the reversed temperature dependence of t_f and how it can be minimized in SX materials. The results of the numerical analysis and experimental verification are presented and discussed in this section.

4.2.2 Numerical Analysis of the Cause of Prolonged Isothermal Solidification Completion Time and its Reversed Temperature Dependence.

In standard analytical TLP bonding models, it is generally assumed that during isothermal solidification, diffusion-controlled migration distance of a liquid-solid interface, J, follows a parabolic relationship with holding time, t, that is given by,

$$J = 2\varphi (t^{1/2}) \qquad (4.2.1)$$

where the parameter φ is known as the interface migration rate constant. The equation denotes a linear relationship between the thickness of the interlayer liquid phase and square root of holding time. It is, however, implicitly assumed in these models that the solid substrate is of infinite or semi-infinite thickness, which permits the use of error function solutions for the Ficks diffusion equation to represent solute distribution in the base material. This enables liquid-solid interfacial displacement to maintain its parabolic relationship with time during continual diffusion of the MPD solute into the base material, even as its concentration gradient in the solid is persistently

reduced. Predictions based on this approach have been previously found to reasonably correlate with some experimentally determined t_f in different alloy systems including in Ni-base superalloys [106, 107]. Nevertheless, a more careful study of the Ficks diffusion equation, on which the standard analytical models are based, suggests that the parabolic behavior with an invariant rate constant, φ, may not be generally applicable to all process conditions during TLP bonding. Whilst it is possible that a single rate constant can describe the isothermal solidification rate, as the solute concentration gradient, $(\partial C/\partial x)$, reduces with continous solute diffusion, for a certain time, this may however, cease to hold when $(\partial C/\partial x)$ falls below a critical value, $(\partial C/\partial x)_c$. This has not been often considered in reported diffusion brazing studies, but may result in significant ramifications as will be shortly discussed. The possible deviation phenomenon and its implications, which are not captured or predicted by standard analytical TLP bonding models, can be duly analyzed by the application of the fully implicit moving-mesh finite element numerical model developed in this work.

To illustrate and discuss the phenomenon, TLP bonding of Ni-base material with different gap sizes having an initial boron concentration of 0 at % with a Ni-B interlayer alloy containing 17 at% of B was numerically simulated at 1100 ^oC. Figures 4.15a and 4.15b show simulated plots of the thickness of residual interlayer liquid against the square root of time and the corresponding boron concentration profile in the base-metal after completion of diffusional solidification, respectively, for the different gap sizes.

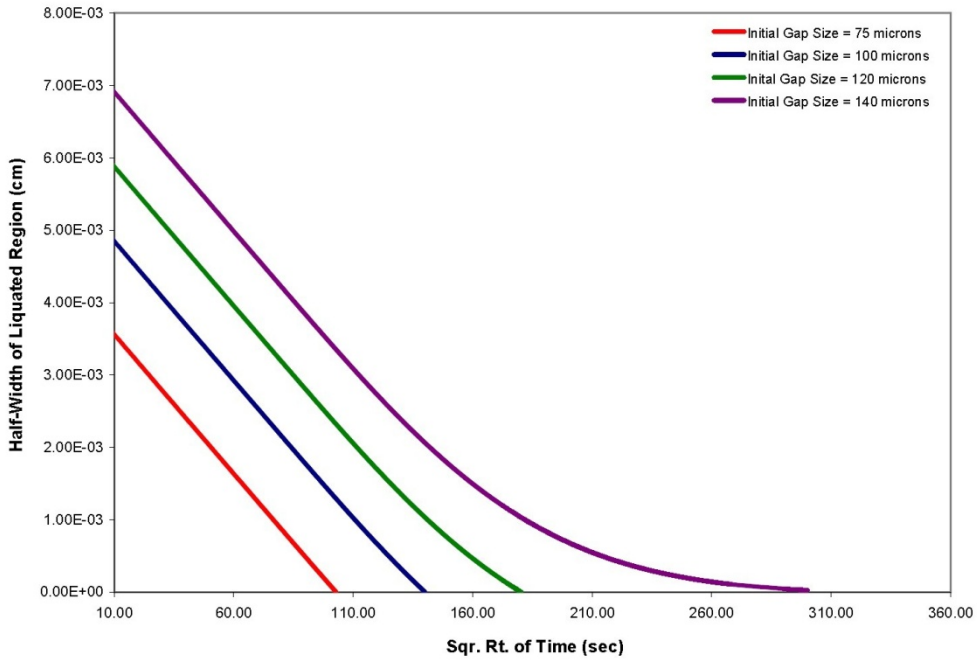

a)

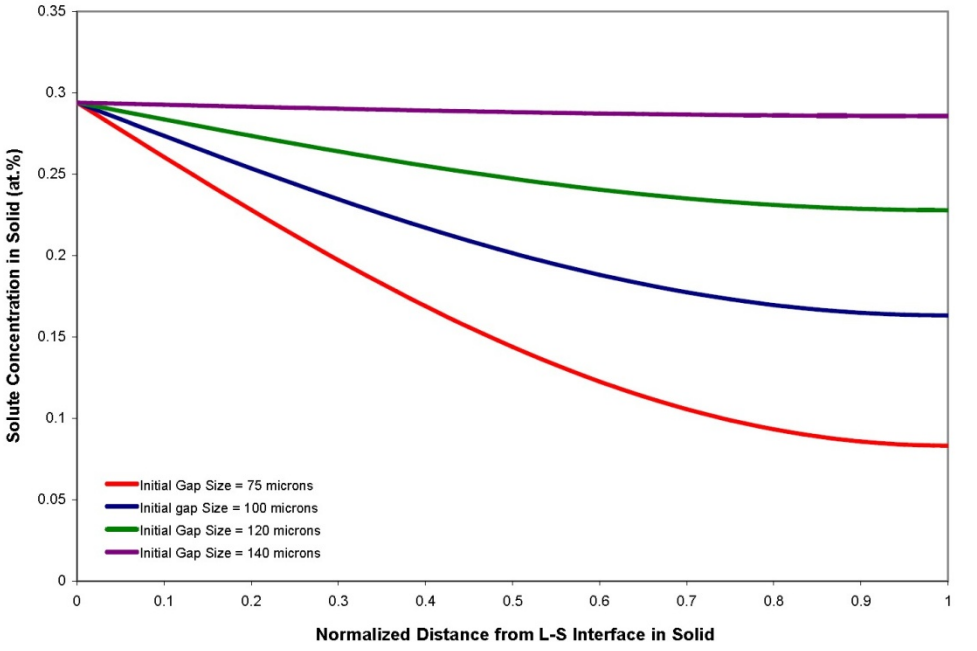

b)

Figure 4.15: Numerical simulation of the effect of initial gap (interlayer) size on a) isothermal solidification time predicted by the numerical simulation model and b) corresponding solute concentration gradient in bulk solid

As evident by the plots, a linear relationship exists between the residual liquid thickness and square root of time throughout the duration of holding time required to achieve complete diffusional solidification for initial gap sizes 75 and 100 μm. This is in agreement with the prediction of standard analytical models. However, an increase in the gap size to 120 μm and 140 μm produced a considerable deviation from the linear relationship at a later stage of the solidification. This deviation from the linear relationship can be related to the concomitant reduction of solute concentration gradient the falls below a critical level, $(\partial C/\partial x)_c$, in the substrate. This is contrary to analytical model predictions, where continual solute diffusion into the base-material has no effect on the parabolic relationship between the liquid-solid interface displacement and holding time. A review of the literature showed that occurrence of this deviation phenomenon which is predicted by the present numerical model can be supported by experimental data reported for both polycrystalline and SX alloys [108-110]. In addition, a similar deviation phenomenon is theoretically was predicted by Illingworth et al. [111] who used an implicit finite difference numerical scheme. The significance of this deviation phenomenon lies in the fact that once it commences, the rate constant, φ, used in analytical models, Equation 4.2.1, would cease to be valid as the diffusional solidification rate would be continually reduced, which in effect, can result in a considerable increase in t_f, including in SX materials.

Aside from the elongation of t_f, a possible consequence of the deviation phenomenon on the temperature dependence of t_f is vital. The rate of decrease of the diffusional solidification rate within the deviation zone, and thus the size of the zone which determines the extent of t_f , is dependent on the magnitude of $\partial C/\partial x$. . The gradient $\partial C/\partial x$ is influenced by the solubility of the diffusing solute in the solid substrate at a particular bonding temperature. As illustrated in Figure

4.16a, a decrease in solute solubility, which is boron in this case. from 0.29 to 0.27 at. % results in larger deviation zone and longer t_f due to an attendant depreciation in $\partial C/\partial x$ (Figure 4.16b). This is practically significant in situations where the solubility of a MPD solute reduces with an increase in temperature, for instance, above the eutectic temperatures in a number of interlayer alloy systems including the Ni-B system. Above any temperature where deviation from the parabolic rule occurs for a given gap size, a decrease in $\partial C/\partial x$, due to a reduction in solute solubility with an increase in temperature, will result in an enlarged deviation zone with concomitant exacerbated solidification rate reduction. This may lead to a situation, in which above a critical temperature, T_c, an anomalous increase in t_f occurs despite an increase in diffusion coefficient with temperature which is commonly expected to reduce t_f. It is interesting to find reported cases in the literature [106, 110], where the reversed temperature dependence of t_f which was experimentally observed also contain data that indicate occurrence of the deviation phenomenon at lower temperatures, even though the phenomenon was not identified as the cause. One of the reported cases involved diffusion brazing of new generation SX Ni-base superalloys with newly developed Ni-Ge interlayer alloys [110]. Identification of the deviation phenomenon as a cause of the reversed temperature dependence of t_f is not possible with commonly used analytical TLP bonding models. An appropriate computational numerical model, as done in this work, is required.

It is in order to clarify here that the concept of an increase in t_f with temperature due to the deviation phenomenon discussed in this work is fundamentally different from another concept discussed in the literature by which t_f can increase with temperature exclusively due to competition between solute solubility and diffusivity [94]. In the later, based on Ficks diffusion

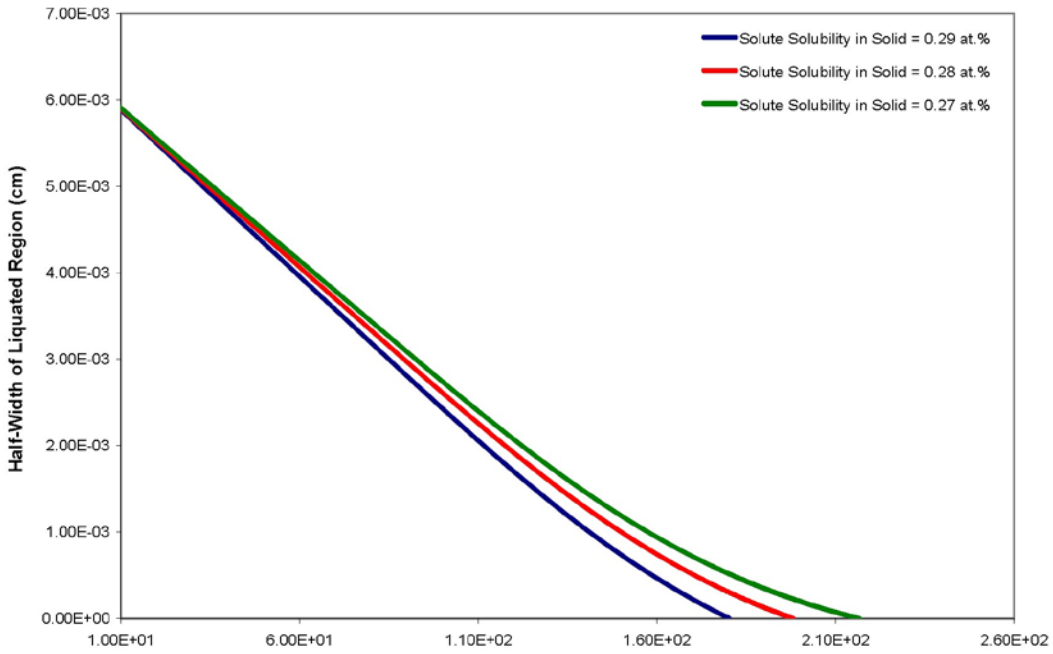

a)

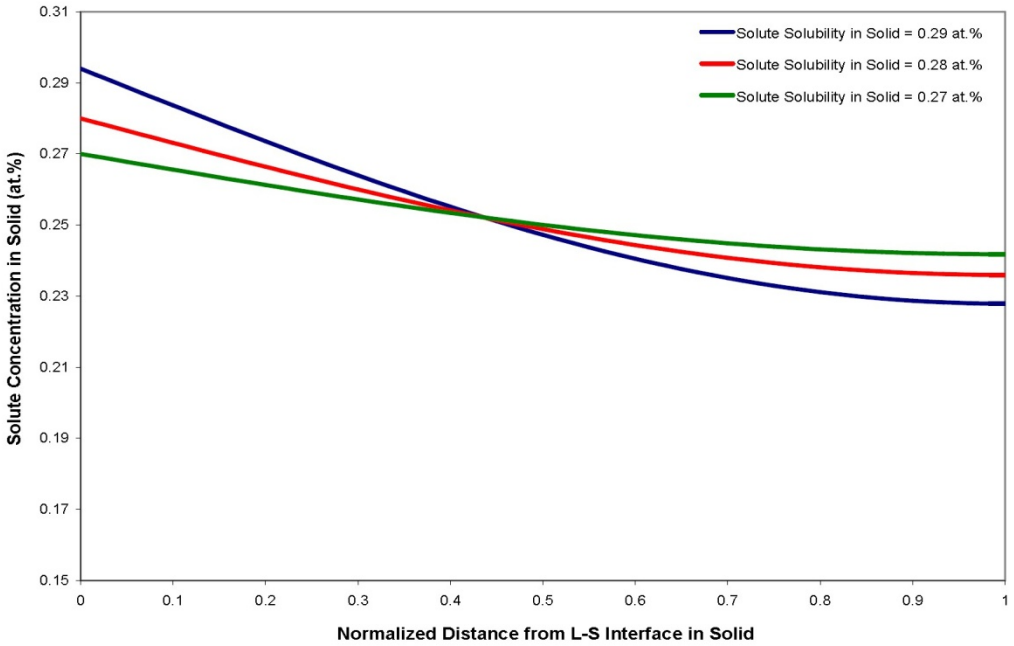

b)

Figure 4. 16: Numerical simulation of the effect of solute solubility in solid on a) isothermal solidification time predicted by the numerical simulation model and b) corresponding solute concentration gradient in bulk solid

equation and in the absence of deviation from the parabolic relationship, an increase in temperature can lead to a temperature where reduced solute solubility can override increased diffusivity and, thus, result in an increased t_f. This concept is the only type that is captured and predicted by standard analytical TLP bonding models [94]. Tuah-Poku et al. [94] used analytical solutions to Ficks second law of diffusion to derive the following expression;

$$t_f = \gamma' \cdot \left[\frac{\exp\left(Q/RT\right)}{\left(C^{\alpha L}\right)^2} \right] \tag{4.2.2}$$

where γ' is a constant and Q, R, T and $C^{\alpha L}$ are activation energy for diffusion, gas constant, temperature and solute solubility in the solid, respectively. They predicted that as temperature increases, t_f will decrease by the exponential term until a critical temperature T_c is reached where an associated reduction in $C^{\alpha L}$ becomes dominant and results in a longer t_f at higher temperature. A notable point is that the T_c determined by competition between an increasing diffusion coefficient exponential term and a decreasing $C^{\alpha L}$, is sensitive and dependent on the activation energy for diffusion. In a direct contrast, the occurrence of T_c by the deviation phenomenon discussed in this work, does not result from competition between diffusivity and solubility, and as such, is independent of the activation energy for diffusion. Numerical simulation showed that, for a given gap size, bonding temperature and filler composition, a change in diffusion coefficient does not have an effect in eliminating the occurrence of the deviation phenomenon, even though it caused reduction in t_f (Figure 4.17). The extent of deviation normally increases with decrease in solubility of the solute in the solid substrate, owing to the concomitant reduction in concentration gradient (Figure 4.15b). As previously stated, once the deviation phenomenon is initiated, a decrease in solute solubility with an increase in temperature would result in a more

pronounced deviation with an attendant increase in t_f. The prolongation effect of the deviation phenomenon on t_f with increased temperature could override the influence of increased diffusion coefficient at higher temperatures, such that t_f becomes longer at higher bonding temperatures compared to lower temperatures.

A tactical verifiable way of distinguishing the occurrences between these two concepts is by studying a plot of the variation of interlayer liquid thickness with holding time. Figure 4.18a shows a plot of half-width of interlayer liquid ($W_{1/2}$) against the square root of holding time ($t^{1/2}$) for a case where T_c is caused by competition between solute diffusivity and solubility, while Figure 4.18b represents a case where T_c is caused by the deviation phenomenon. As seen in Figure 4.18a, at temperatures above T_c where t_f is longer at any higher temperature, the thickness of the interlayer liquid is necessarily larger at the holding temperature T_h relative to a lower temperature T_l throughout the entire holding time period. However, as seen in Figure 4.18b, this is not always the case, at temperatures above T_c, it is possible to find a high holding temperature, T_h , at which t_f is longer relative to a lower temperature, T_l, even though the thickness of the interlayer liquid was smaller compared to at T_l over a certain range of holding time, Δt.

This tactful difference is due to the fact that the occurrence of the reversed temperature dependence of t_f in Figure 4.18b is caused by the deviation phenomenon as compared to the case in Figure 4.18a which is attributed to competition between diffusivity and solubility. A review of the literature showed that if the reported data are subjected to the criterion discussed, the observed increase in t_f with temperature can be explained by the deviation phenomenon and not

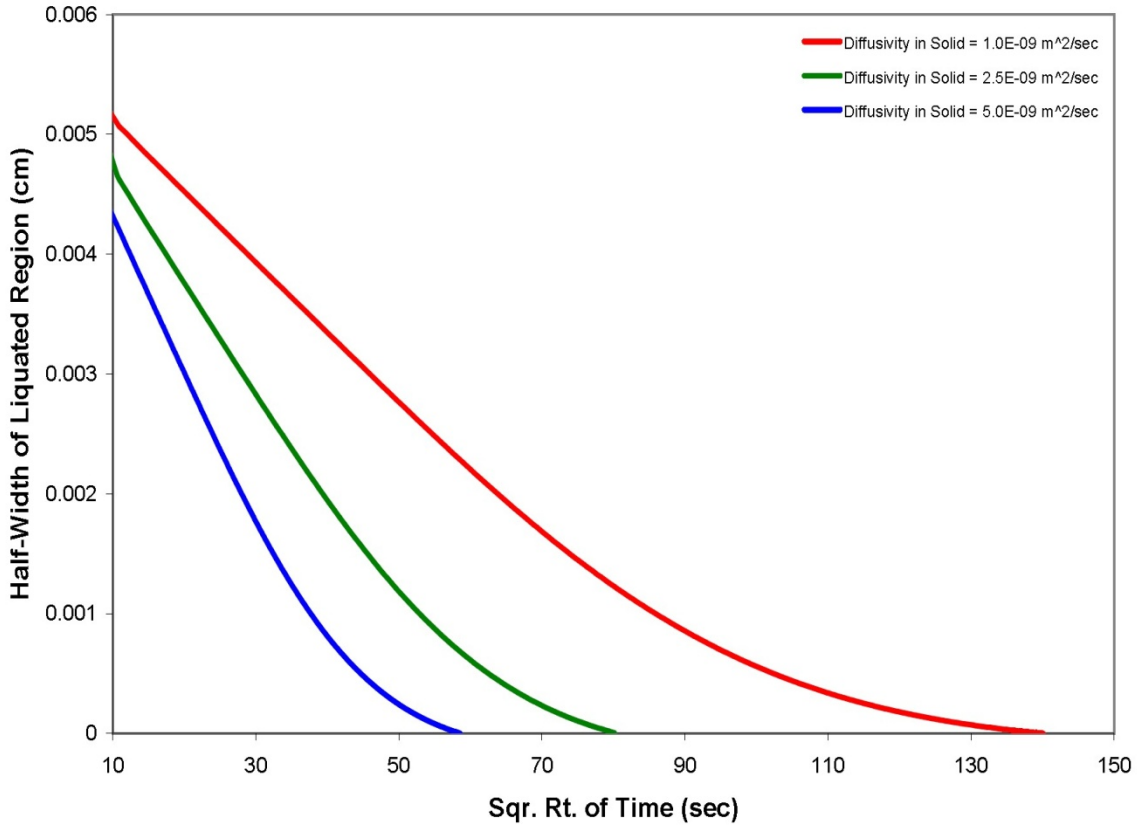

Figure 4. 17: Numerical simulation of the effect of solute diffusivity on deviation from parabolic law and isothermal solidification completion times

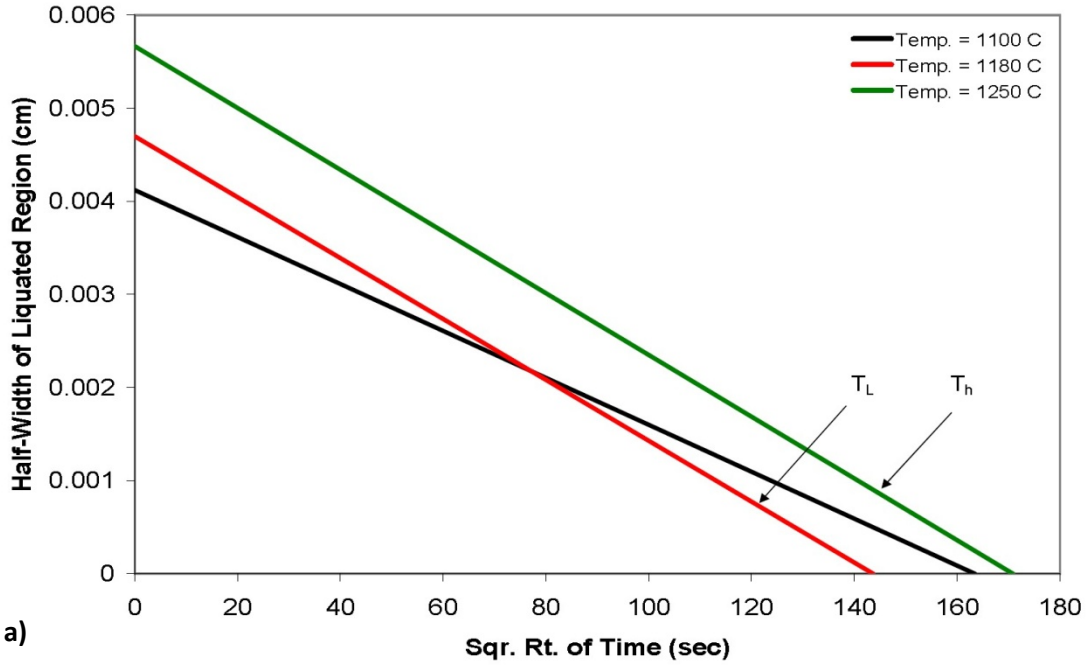

a)

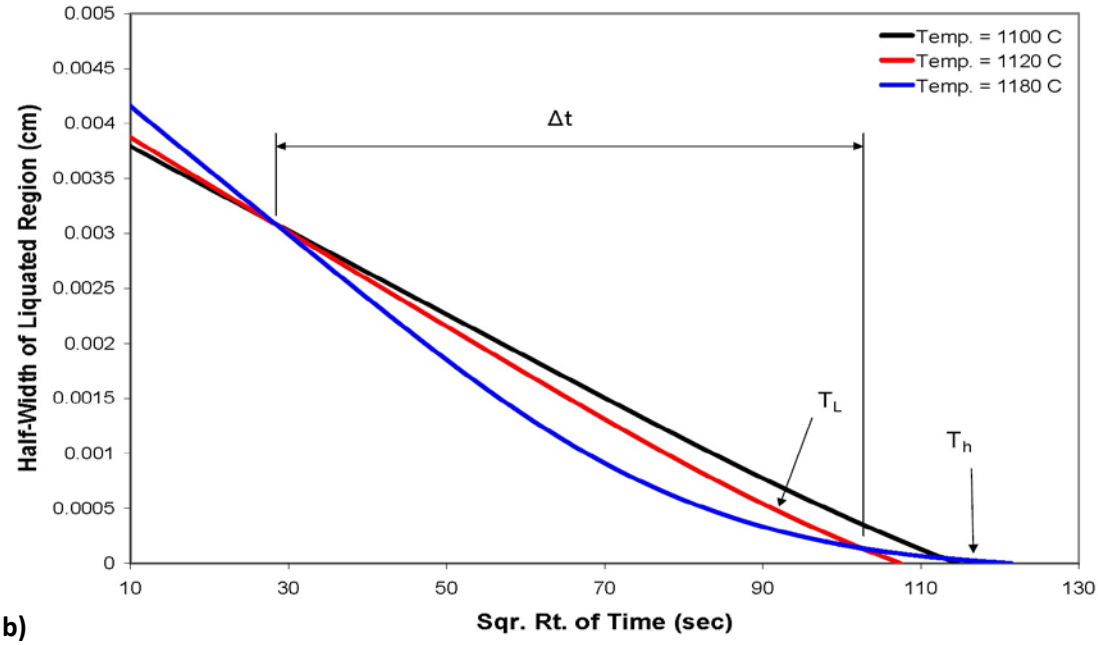

b)

Figure 4. 18: a) Predicted isothermal solidification times obtained by the conventional analytical model

b) Predicted isothermal solidification times obtained by the new finite element simulation model

the suggested reasons as given in the publications [106]. This further emphasizes that a primary cause of a long t_f during TLP bonding is due to the occurrence of the deviation from the parabolic rule which is illustrated in this study.

4.2.3 Experimental Verification of the Cause of Reversed Temperature Dependence of t_f

An experimental study was performed to verify which of the two concepts can explain the occurrence of the reversed temperature dependence of t_f in a common commercially used Ni-base SX superalloy CMSX-4. TLP bonding of the SX superalloy substrates, with an initial gap size of 80 µm, was performed in a vacuum brazing furnace with the use of a commercial Ni-Cr-B interlayer alloy, Metglass MBF-80, at temperatures ranging from 1070^{o}C to 1230^{o}C. It was observed that 16 hrs of holding time is insufficient to achieve complete isothermal solidification of the liquated insert at 1070^{o}C. An increase in the bonding temperature to 1180^{o}C, resulted in complete isothermal solidification within 16 hrs of holding time, producing a eutectic-free joint (Figures 4.19a). This shows that t_f decreases with temperature increase. However, with a further increase in temperature to 1230 ^{o}C, there was an increase in t_f , which indicates that the occurrence of reversed temperature dependence of t_f. The 16 hrs of holding time that resulted in complete isothermal solidification and produced a eutectic-free joint at 1180^{o}C was found to be inadequate to produce complete isothermal solidification at 1230^{o}C, resulting in eutectic formation within the joint produced at 1230^{o}C (Figure 4.19b). It was observed that even an increase in the holding time to 20 hrs is still insufficient to achieve complete isothermal solidification at the 1230^{o}C bonding temperature.

a)

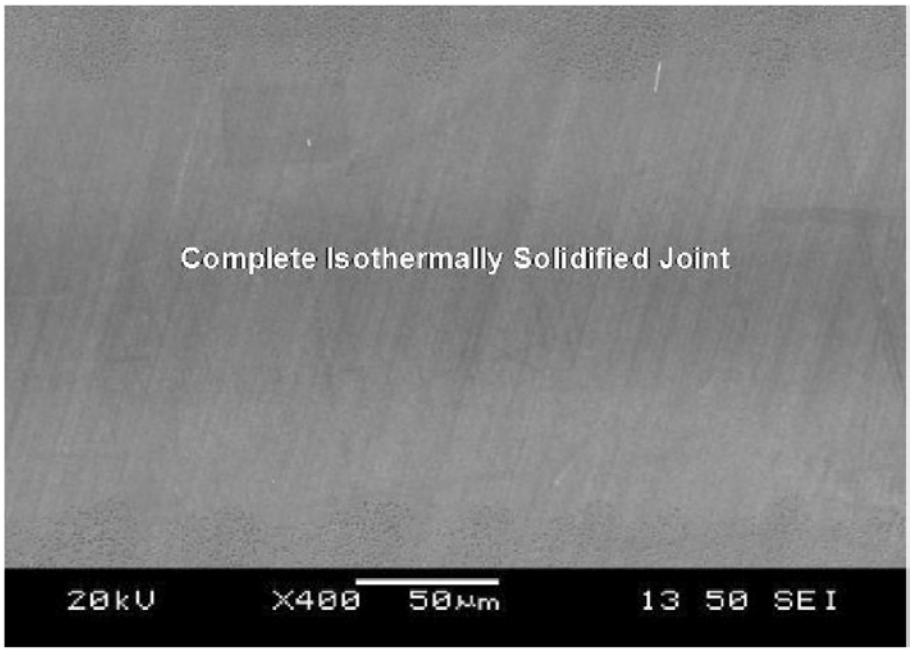

b)

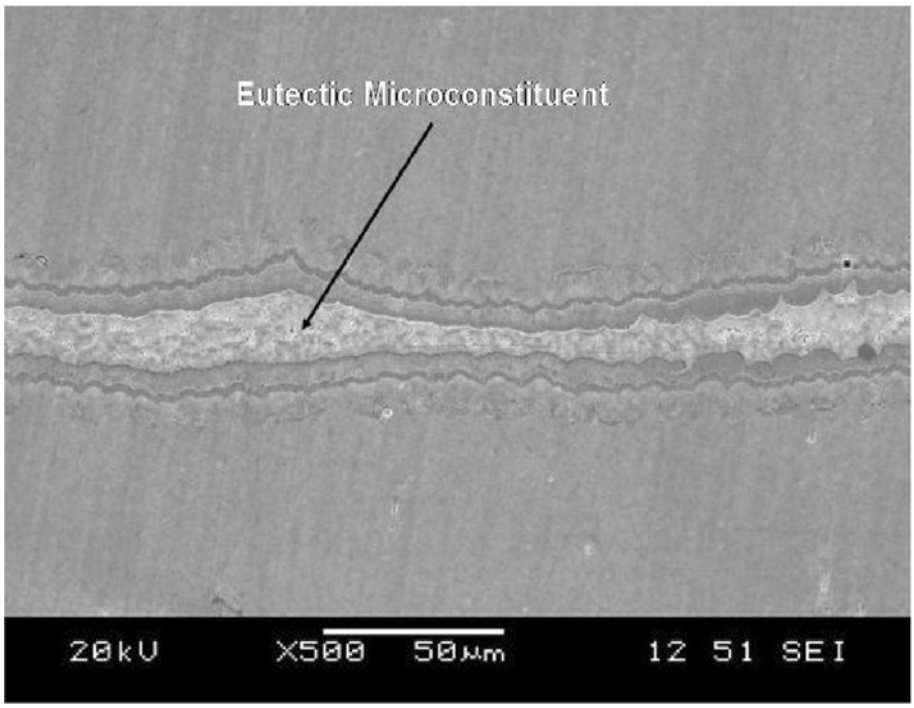

Figure 4. 19: Scanning electron microscopy of micrograph for CMSX4 showing a) Completely solidified TLP joint prepared at 1180 °C for 16 hours b) center line eutectic for TLP joint prepared at 1230 °C for 16 hours

Since t_f is longer at 1230^{o}C compared to that at 1180^{o}C, an attempt was made to examine if at any time during bonding, the thickness, J, of the interlayer liquid, which transforms into the centerline eutectic in the joint, was less at 1230^{o}C relative to that at 1180^{o}C. It was interesting to find that after 4 hrs of holding time, the average thickness of the centerline eutectic that was formed in the joint at 1230^{o}C (29 μm), is significantly less than the eutectic thickness formed in the joint at 1180^{o}C (42 μm). As discussed earlier, this behavior cannot be explained by the concept of competition between diffusivity and solubility of solutes but rather by the deviation phenomenon. Furthermore, according to the concept based on competition between solubility and diffusivity of solutes, for a given interlayer-base alloys system, the temperature, T_c, is constant and independent of the gap size. On the contrary, based on the deviation phenomenon, for a given interlayer-base alloys system, T_c is a variable that changes with the gap size. The increase in t_f which resulted from an increase in temperature from 1180^{o}C to 1230^{o}C observed in TLP bonding for a gap of 80 μm was not observed for 40 μm. Moreover, it should also be stated that the reversed temperature dependence of t_f was observed to occur irrespective of the thickness of the substrate material. The base-material thickness was increased from 6 mm to 21 mm and 30 mm, respectively, and the deviation phenomenon was observed to occur to a comparable degree for all the specimens, irrespective of the base-material thickness.

4.2.4 A Viable Approach to Reducing t_f and Preventing Stray Grain Formation during Bonding of Single Crystal Alloys.

The theoretical and experimental analyses in this study have shown that the primary cause of prolonged t_f during bonding at high temperatures is the reduction in the solute concentration

gradient within the substrate material below a critical level, $(\partial C/\partial x)_c$. As shown in Figure 4.20, a decrease in the extent of reduction in the solute concentration gradient can be achieved by reducing the initial concentration of the MPD solute in the interlayer material, C_{FI}. Based on this concept, it is possible to alleviate the problem of increases in t_f with increases in bonding temperature by limiting the extent of the reduction in the $\partial C/\partial x$, which, theoretically, can be done by reducing C_{FI}. Although the approach appears to be feasible, the practical challenge lies in the fact that most commercially available interlayer alloys are produced with fixed chemical compositions that have been optimized to achieve certain required characteristics such as the the shape, size and form of the interlayer material. Therefore, reducing C_{FI} to minimize t_f would benefit from any innovative way to achieve this goal without necessarily changing the initial composition of the interlayer alloys.

A possible way of doing this is by mixing a powder form of commercially available brazing alloy with that of a suitable alloy that is essentially free of the MPD element, hereafter referred to as gap-filler alloy, which can be the powder of the base-alloy. The powder mixture of a gap-filler alloy and a brazing alloy can then be used as the interlayer material for TLP bonding of SX alloys. This appears to be similar to the approach typically used during conventional wide-gap brazing, however, there is an important fundamental difference. It is generally known that during conventional wide-gap brazing, only limited melting of the gap-filler alloy occurs while the brazing alloy power melts at brazing temperature. This has, thus, constituted a major limitation to the application of this approach to SX substrates. The partially melted powder particles of the gap-filler alloy in the joint cause formation of stray grains in the joint region, which compromises the high temperature properties of bonded SX materials [19, 112].

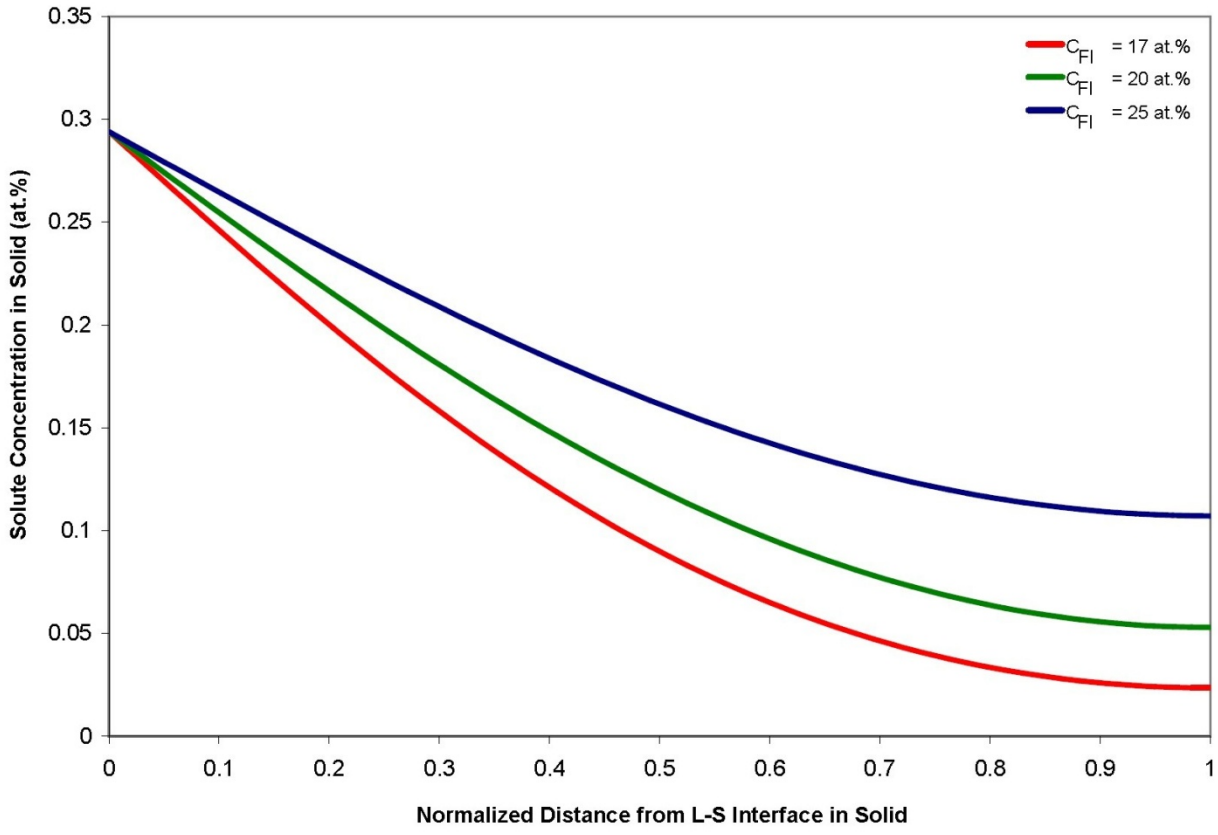

Figure 4. 20: Numerical simulation plot of the effect of the influence of initial concentration of MPD solute in interlayer material, C_{FI}, on solute concentration gradient in the base material

Understanding of the liquid phase dissolution of additive powder particles of gap-filler alloy by the molten brazing alloy, in a composite mixture of the two during TLP bonding, has been limited mainly due to the large number of process and microtructural parameters evolved that affect the final joint microstructure. Mathematical modeling of powder TLP bonding is also limited due to certain difficulties that can be summarized as follows:

- existing analytical models are not capable of simulating solid dissolution;
- the large number of powder particles mean that a large number of particle-liquid boundaries exist which need to be tracked to study the evolution of powder particles with time;
- at any time, a powder particle-liquid interface may break up, or join with neighboring interfaces. This poses severe difficulties when conventional interface-tracking methods are used;
- topological changes of the growing/dissolving powder particle pose difficulties where current numerical TLP bonding models can't handle; and
- the dissolution of powder occurs rapidly compared to the isothermal solidification stage. To capture the intricate changes of the powder particles, different time stepping scales are required.

To overcome these difficulties, a new approach based on the cellular automata method is used to model powder TLP bonding and coupled with the new finite element simulation model. The development of the cellular automata model used in this research is discussed in the following section. The output of the model is fed into the newly developed finite element model,

discussed in section 4.1, to estimate the processing time t_f when powder mixture of brazing alloy and gap-filler alloy is used as the interlayer material.

4.2.4.1 Mathematical Formulation of Cellular Automata Numerical Model

A two-dimensional domain Ω is discretized into separate cells. Each cell holds a finite number of data associated such as, temperature T, composition C, spin index S, phase index Φ, and solid-fraction *f*. The spin index S represents the crystallographic orientation of a powder particle, which is 0 in liquid and can be any integer number in a solid phase. The phase index Φ can either be 0 (liquid) or 1(solid). The solid fraction, *f*, in any given cell can vary from 0 to 1. A cell having an *f* value of 0 is a liquid cell, a value of 1 is solid, and cells having values $0 < f < 1$ define an interface cell.

The basic idea of the current model is to calculate the evolution of the solid fraction in each cell instead of directly tracking the interface motion between a powder particle and the liquid. This approach gives a good representation of the evolution of powder particles while avoiding having to explicitly track the powder particle-liquid interfaces and avoiding difficulties when topological changes occur and when interfaces break up or join together.

The liquid phase has an initial solute concentration C_F and the solid particles have an initial solute concentration C_m. Solute diffusion in the liquid phase is expressed by:

$$\frac{\partial C_L}{\partial t} = D_L\left(\frac{\partial^2 C}{\partial x^2} + \frac{\partial^2 C}{\partial y^2}\right) \tag{4.2.3}$$

Similarly, solute diffusion in the solid particles is expressed as:

$$\frac{\partial C_S}{\partial t} = D_S\left(\frac{\partial^2 C}{\partial x^2} + \frac{\partial^2 C}{\partial y^2}\right) \tag{4.2.4}$$

where D_s and D_L are the diffusivities in the solid and liquid cells, respectively. The increase in the solid fraction Δf_S is calculated using:

$$\Delta f_S = \frac{\Delta t}{\Delta X}\left(V_x + V_y - V_x V_y \frac{\Delta t}{\Delta X}\right) \tag{4.2.5}$$

where Δt is the time step, ΔX is the cell size, V_x and V_y represent the velocity of the interface cells in the x and y directions. These velocities are calculated using:

$$V_x = \left(\frac{1}{C_L^* - C_S^*}\right)\left\{-D_L \frac{\partial C_L}{\partial x} + D_S \frac{\partial C_S}{\partial x}\right\} \tag{4.2.6}$$

$$V_y = \left(\frac{1}{C_L^* - C_S^*}\right)\left\{-D_L \frac{\partial C_L}{\partial y} + D_S \frac{\partial C_S}{\partial y}\right\} \tag{4.2.7}$$

where C_L^* and C_S^* are the equilibrium liquidus and solidus concentrations at the interface cells, repectively, at the bonding temperature, T, which are assumed constant during the dissolution process. This assumption is justified due to the previous work done by Enomoto et al. [113], where they investigated the influence of solute concentration at curved interfaces on the growth and dissolution kinetics of spherical precipitates. They concluded that the dissolution time is not significantly influenced when interfacial solute concentration is curvature dependent except for cases where the initial particle size was extremely small (less than a few nanometers). This has been also experimentally validated in aluminum alloys by Tundal et al.

[114] and Vermolin et. al. [115]. In this study, since the average size of the powder particles used in the numerical simulations is more than 5μm, hence, it is reasonable to assume local equilibrium solidus and liquidus concentrations at the particle-liquid interfaces.

At any given time, curvature of the liquid-solid interface is calculated using the procedure proposed by Sasikumar et al. [116], where the number of cells in the extended neighborhood of the interface cell is counted. For example, a 7 x 7 square of cells, which yields a total area of $N_t = 49\Delta X^2$, is drawn around the cell of interest and the number of solid fraction, N_s, in the region is determined. The value for curvature κ can then be found from:

$$\kappa = \frac{1}{\Delta X}\left(1 - \frac{2N_s}{N_t}\right) \tag{4.2.8}$$

To calculate the concentrations in the liquid and solid, a typical cell-centered fully implicit transient finite volume method is used to solve equations 4.2.3 and 4.2.4. An identical square mesh was used for both the CA and the finite volume computations. Even though a fully implicit transient method is used to solve the concentration equations, there is still a critical time step that must not be exceeded to ensure that the interface velocity is not too high to cause instabilities in the CA solution. The critical time step is calculated from:

$$\Delta t = 0.25 \min\left(\frac{\Delta x}{V_n^{\max}}, \min\left(\frac{\Delta X^2}{D_L}, \frac{\Delta X^2}{D_S}\right)\right) \tag{4.2.9}$$

where $V_n^{\max}$ is the maximum velocity of the interface cells. The interface velocities and solute concentrations are calculated under the following assumptions:

1. the molar volume is assumed to be constant in both the liquid and solid;

2. the diffusivity of the MPD solute is independent of concentration;

3. the equilibrium concentrations at the powder particle-liquid interface are assumed constant and independent of the interface curvature; and

4. the dissolution process is assumed to occur at a constant temperature.

4.2.4.2 Implementation of the Cellular Automata Model

All cells are initially set to have a solid fraction of zero and random sites are chosen as seed sites. Each site is assigned a random spin index that represents the crystallographic orientation of a powder particle. Neighboring cells that have the same spin index belong to the same grain and, therefore, will not form a grain boundary. The seed sites and the immediate Von-Neumann neighbors are set to have a solid fraction of 1. A simple CA rule is applied to allow these seed sites to grow for some user specified CA steps until the desired initial powder-to-liquid ratio is obtained. Basically, a cell is chosen and if it is determined to be a solid cell, it remains unchanged. However, if it is a liquid cell, then the total number of solid cells in the immediate Moore-type neighborhood is counted. If the total is at least 3, the cell becomes a solid cell. This can be summarized in the following pseudo-code, where Z is the total number of cells and Z_{min} is the minimum number of neighbor cells, N, required for transformation:

if $\Phi_{i,j}^{t} = 0$

$$Z = \sum_{k=1}^{N} \left\{ \Phi_{i+1,j}^{t}, \Phi_{i-1,j}^{t}, \Phi_{i,j+1}^{t}, \Phi_{i,j-1}^{t}, \Phi_{i+1,j+1}^{t}, \Phi_{i+1,j-1}^{t}, \Phi_{i-1,j+1}^{t}, \Phi_{i-1,j-1}^{t} \right\}$$

if $Z \geq Z_{\min}$

$$\Phi_{i,j}^{t+\Delta t} = 1$$

else

$$\Phi_{i,j}^{t+\Delta t} = 0$$

end

end

To reduce the strong anisotropy, the above pseudo-code is modified by performing random scanning of cells. If a scanned cell is a solid interface cell, curvature is estimated based on an approach similar to Equation 4.2.8 by using a 5x5 cell template with the interface cell at the center. The total number of solid cells in the template is determined and if the sum is larger than or equal to 15, the cells in the Von-Neumann neighborhood turn to solid, otherwise, the solid cell remains unchanged.

So far, the resultant states of the cells only represent the *initial* powder particles and liquid before simulation is initiated. To start the simulation, interface cells are defined if a solid cell has at least one liquid neighbor cell. Initial solute concentrations in the solid particles and the liquid are subsequently defined and interface cells are assumed to be at the equilibrium liquidus and solidus concentrations. Since the initial distribution of the powder particles in the liquid is completely random, some particles may share a boundary. If any two particles have

different spin index S then the boundary cells are set to be the interface cells. However, if the two particles share the same spin index, they are considered as a single particle. The computational algorithm used for the model can be summarized as follows:

1. seed sites are randomly chosen and grown until the user specified powder-to-liquid ratio is achieved;

2. future solute concentrations in the liquid and solid phases are simultaneously calculated for one time step;

3. a cell is randomly chosen, and if it is determined to be liquid or solid then it is left unchanged. However, if it is an interface cell, interface cell velocities in the X and Y directions are calculated;

4. the change in solid fraction, Δf , is calculated to update the existing solid fraction in the interface cell;

5. if the new solid fraction in the interface cell is larger than 1, the solid fraction is set to 1 and the extra solid fraction is evenly distributed among identified neighboring liquid cells. The cells subsequently become interface cells, while interfacial curvature is calculated and the associated solute concentration is set at the equilibrium value. Likewise, if the solid fraction of the cell is less than 0, the solid fraction is reset to 0. The neighboring solid cells are then determined and the difference in solid fraction is evenly extracted from the neighboring cells;

6. cell spin index is updated depending on particle growth or dissolution. A dissolved solid cell has a spin index of zero;

7. steps 3-6 are repeated such that all the cells in the domain are scanned at least once. This randomized manner of scanning is necessary to reduce grid anisotropy that is typically associated with cellular automata models;

8. all data associated with each cell are updated and steps 2-7 are repeated for the next time step.

Due to the much smaller size of the powder particles compared to the base materials, and since the dissolution stage occurs quite rapidly, the computational mesh used for the cellular automata simulations were much finer than those used for the finite element analysis to capture the intricate topological changes of the powder particles. Additionally, the time steps used for the cellular automata simulations to predict dissolution of the powder particles were much smaller than those used for the finite element analysis to predict the diffussional-solidification kinetics. Both models are coupled by averaging the final solute concentrations in all liquid phase cells calculated after complete dissolution of the powder particles using the cellular automata model and then incorporated into the finite element simulation model to calculate the diffusion of solute from the liquid into the base materials and the migration of the liquid-bulk solid interfaces.

It is clear that this multi-scale approach allows the computational model to be capable of efficiently capturing the intricate and rapid topological changes of the small powder particles while also capturing the solute diffusion in the much larger bulk solids and the associated migration of liquid-bulk solid interfaces.

4.2.4.3 Application of the Cellular Automata Model

Based on the principle of TLP bonding, immediately after melting of the brazing alloy at the bonding temperature, rapid dissolution of the base material into the liquated brazing alloy occurs in order for the solid to dilute the solute concentration in the liquid and for both phases attain their equilibrium solute concentrations, which is also known as the equilibration process. The same equilibration process ensues when base alloy powder particles are surrounded by brazing alloy powder that has been liquated at the bonding temperature. Modeling of this equilibration process through base alloy dissolution by the analytical approach often involves non-trivial assumptions that could significantly affect the reliability of model predictions. One of these critical inherent assumptions is that solute diffusion into the base alloy does not occur during the equilibration process. This potentially consequential assumption is not included in the numerical simulation model developed and used in the present study, as simultaneous solid-state and liquid-state solute diffusion are allowed and captured by the model. Figure 4.21 shows solute distributions in the base alloy powder particles and surrounding liquid phase after some time during the equilibration process. Upon the completion of the equilibration process, particle dissolution by the surrounding liquid would cease and thermodynamically stable residual particles may exist within the liquid phase, due to incomplete particle dissolution. Isothermal solidification of the liquid starts subsequent to the equilibration stage and the residual un-dissolved powder particles, with random crystallographic orientations, would result in the formation of stray grains in the joint after the completion of isothermal solidification process, as shown in Figure 4.22.

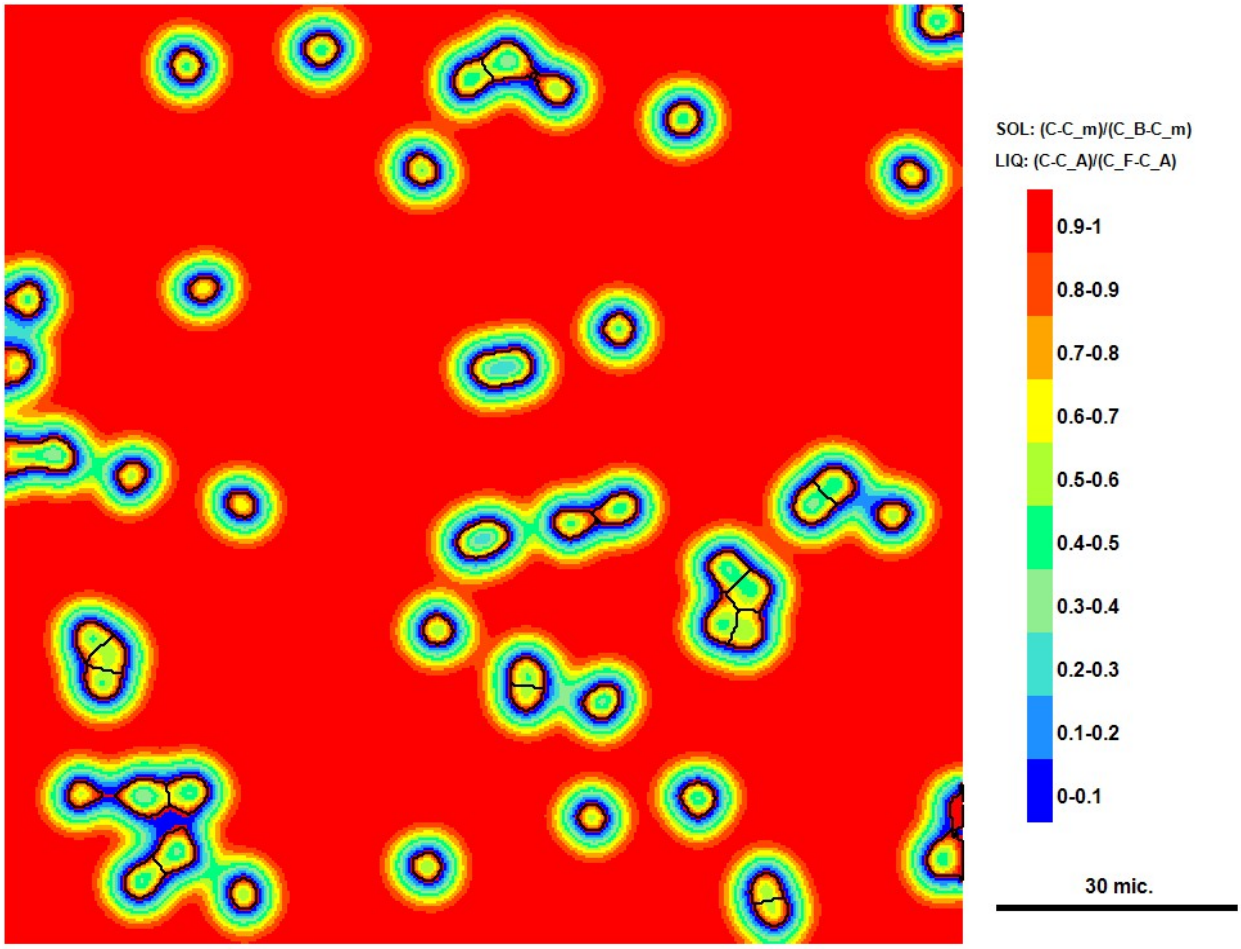

Figure 4. 21: Numerical simulation of MPD solute distribution after 60 time steps

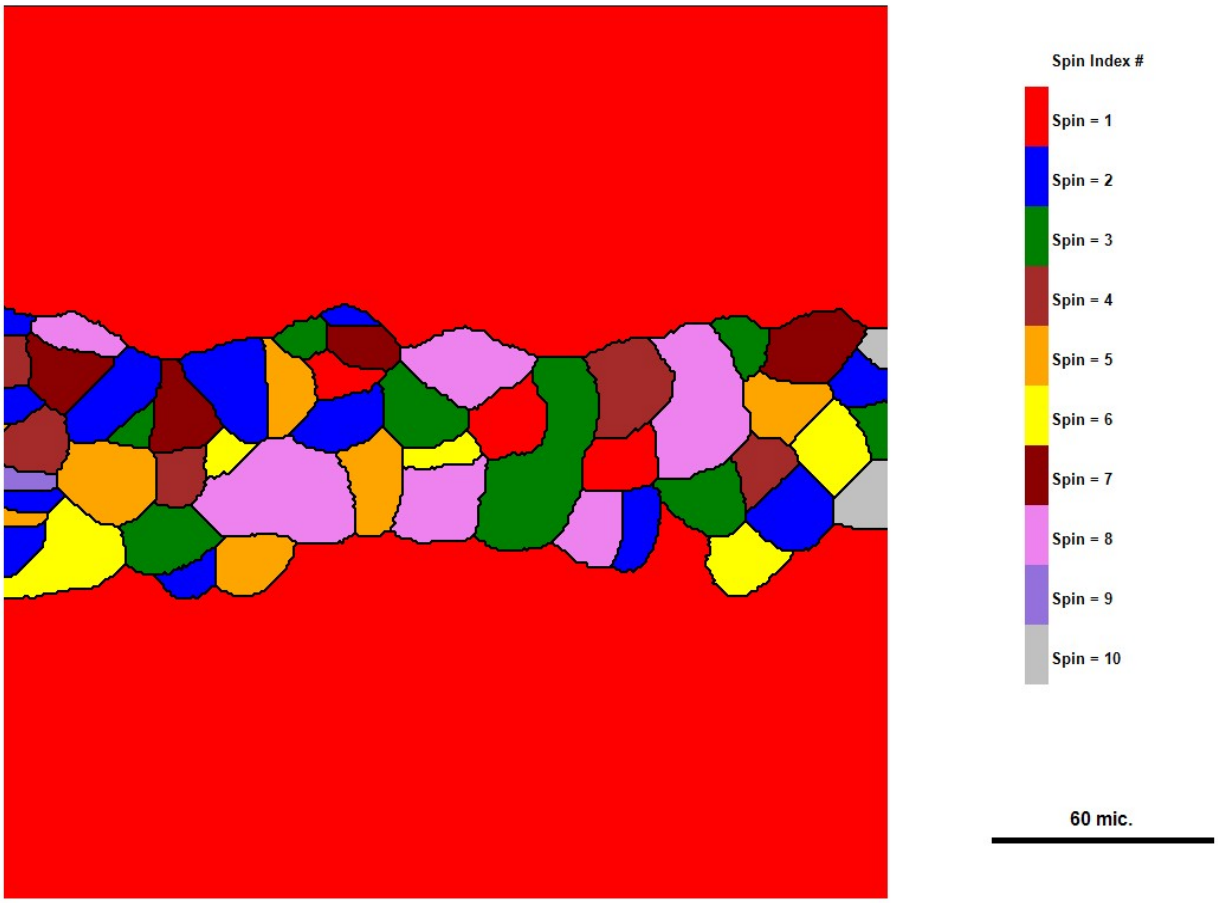

Figure 4. 22*:* Numerical simulation of joint showing stray grain formation between two single crystal base materials

Numerical calculations showed that the quantity of residual solid particles present after equilibration is dependent on a combination of (i) the ratio of the volume of brazing alloy powder particles to that of the gap-filler particles, $R_{B/G-F}$ (ii) temperature (iii) concentration of MPD in the brazing alloy, C_{FB} and (iv) the initial size of the gap-filler powder particles, P_s (Figure 4.23). As shown in Figure 4.24, for a given combination of temperature, C_{FB} and P_s, an increase in $R_{B/G-F}$ increases the extent of particle dissolution with concomitant reduction in residual solid particles and complete particle dissolution is possible when it rises above a critical value of $R_{B/G-F}$ i.e. $(R_{B/G-F})_c$. The $(R_{B/G-F})_c$ reduces with an increase in temperature and C_{FB} (Figures 4.25, 4.26) Preclusion of residual powder particles after the equilibration stage, through complete liquid phase dissolution, removes a critical cause of stray-grain formation in the joint region upon the completion of isothermal solidification. Accordingly, the simulation results that indicate the conditions that enable complete liquid phase dissolution suggest that it is possible to use a powder mixture of brazing alloy and additive gap-filler alloy as the interlayer material without stray-grain formation in joint between SX substrates (Figure 4.27). This is a scenario that had not been previously reported in the literature prior to this study. Prakash et al. [112] stated in the publication on "Advanced technologies for repair of SX turbine blades" that the use of powder mixture as interlayer material had not reported to produce stray-grain free joint in SX materials. Furthermore, complete melting of the powder mixture would result in reduced initial concentration of MPD solute in the interlayer liquid, $C_{FI,}$ (Figure 4.28) which is a necessary condition required to reduce the processing t_f including at high temperatures where the deviation from parabolic rule is active as proposed earlier.

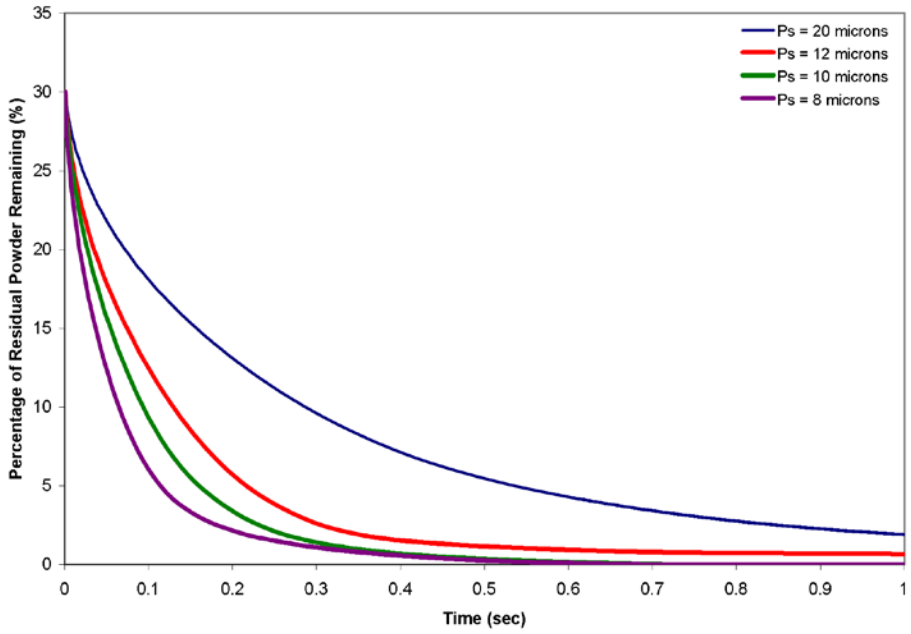

Figure 4. 23: Numerical simulation plot of the effect of P_s on residual powder remaining at the joint

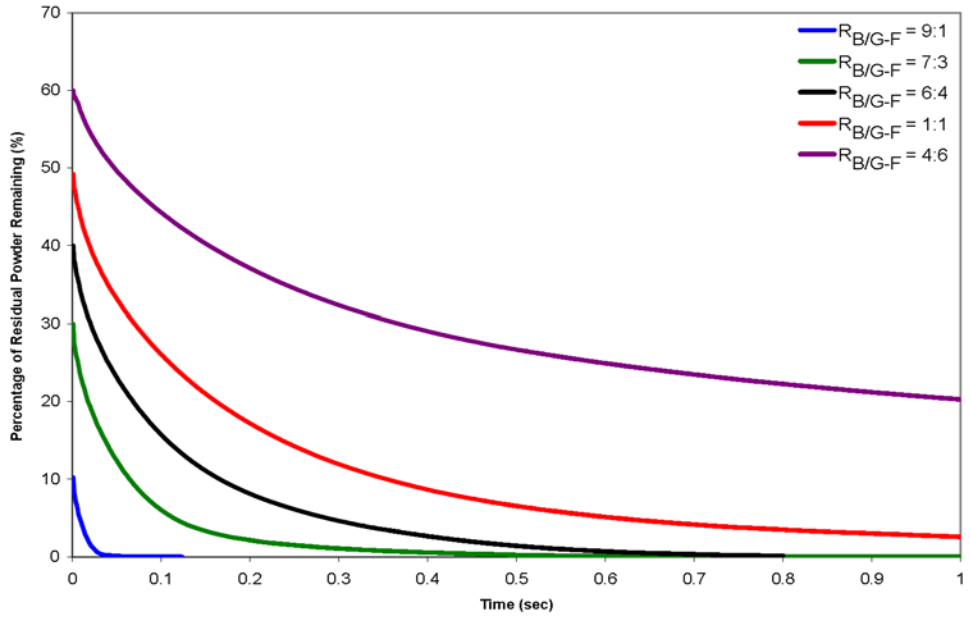

Figure 4. 24: Numerical simulation plot of the effect of $R_{B/G-F}$ on residual powder remaining at the joint

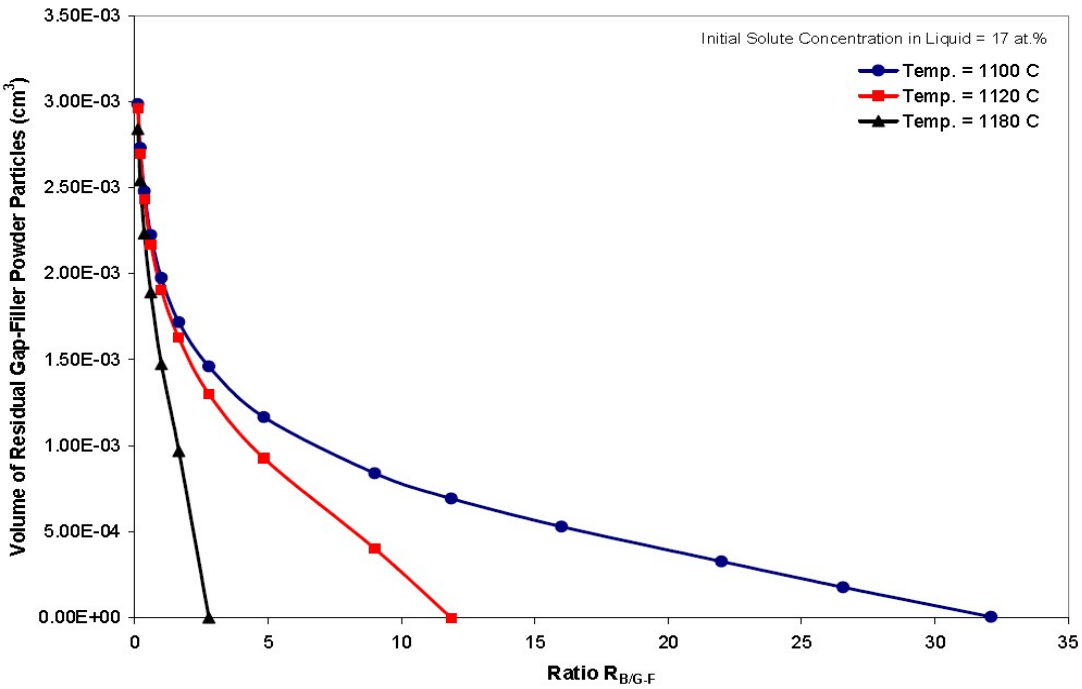

Figure 4. 25: Numerical simulation plot of the effect of Effect of temperature on critical ratio $R_{B/G-F}$

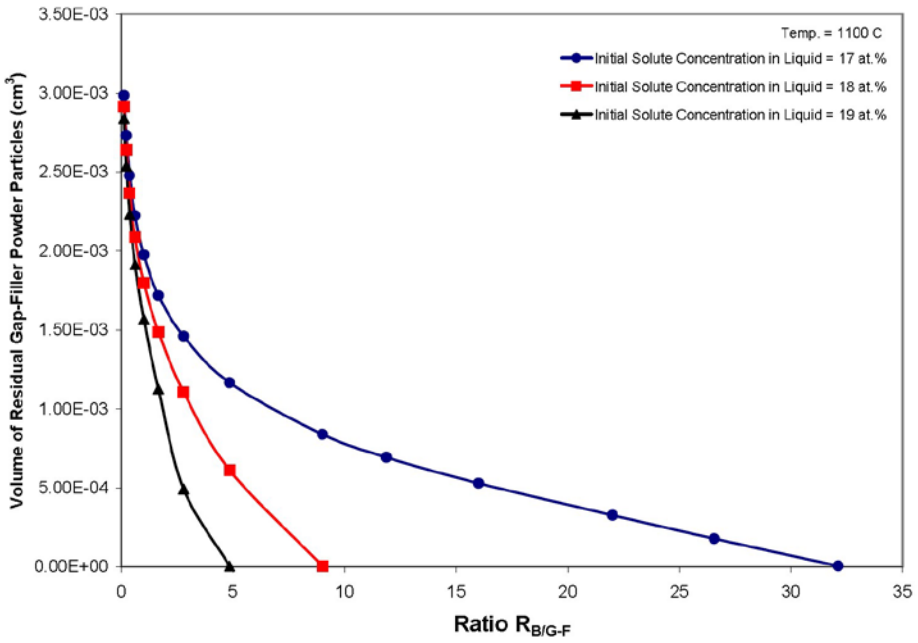

Figure 4. 26: Numerical simulation plot of the effect of initial solute concentration C_{FB} on critical ratio $R_{B/G-F}$

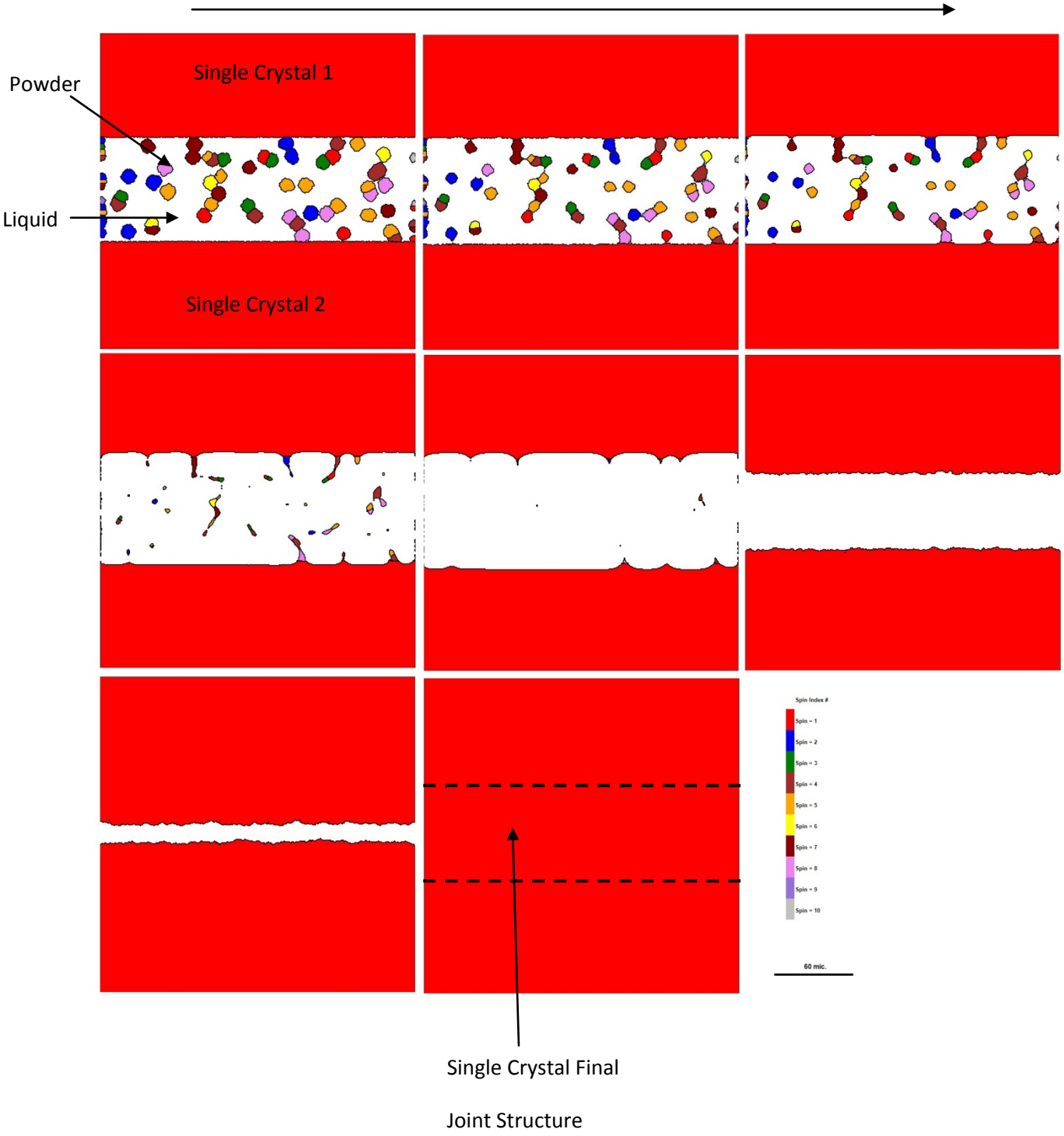

Figure 4. 27: Numerical simulation snapshots o f the joint region showing complete dissolution of powder particles and a single crystal final structure ($R_{B/G-F}$ = 7:3, Temp = 1200 ^{o}C)

TLP bonding experiments were performed to verify the prediction of the numerical model by using a powder mixture as the interlayer material and IN 738 superalloy as the base-material. The interlayer powder mixture consisted of a commercial Ni-Cr-B brazing powder, Nicrobraz 150, with 3.5 wt% boron content and IN 738 superalloy powder as the gap-filler alloy. The results showed that an $R_{B/G-F}$ of 1:1 resulted in partial melting of the gap-filler powder particles could at 1150^{o}C (Figure 4.29). A crystallographic orientation imaging microscopy (OIM) study of the residual powder particles showed the formation of high angle grain boundaries at the interface where adjacent particles with random orientation join during particle growth, which confirms the simulation result (Figure 4.30). An increase in the $R_{B/G-F}$ to 7:3 resulted in complete melting of the interlayer mixture at the same bonding temperature of 1150^{o}C (Figures 4.31a). The solidified microstructure of the $R_{B/G-F}$ of 7:3 interlayer material is free of the residual gap-filler powder, and instead, consists of a dendritic structure similar to that of completely melted 100% brazing filler alloy (Figure 4.31b). The completely liquated power mixture with $R_{B/G-F}$ of 7:3 produced a stray-grain-free isothermally solidified layer on top of the SX substrate (Figure 4.32a), which was processed at 1150^{o}C for 18 hrs. In contrast, however, the incompletely melted mixture $R_{B/G-F}$ of 1:1 resulted in formation of stray-grains within the isothermally solidified region processed at 1150^{o}C for 18 hrs (Figure 4.32b). Electron backscatter diffraction based OIM showed that the character of most of the grain boundaries in the $R_{B/G-F}$ of 1:1 deposit are high angle grain boundaries with coincident site lattice "$\sum$" values greater than 29 (Figures 4.33a and 4.33b).

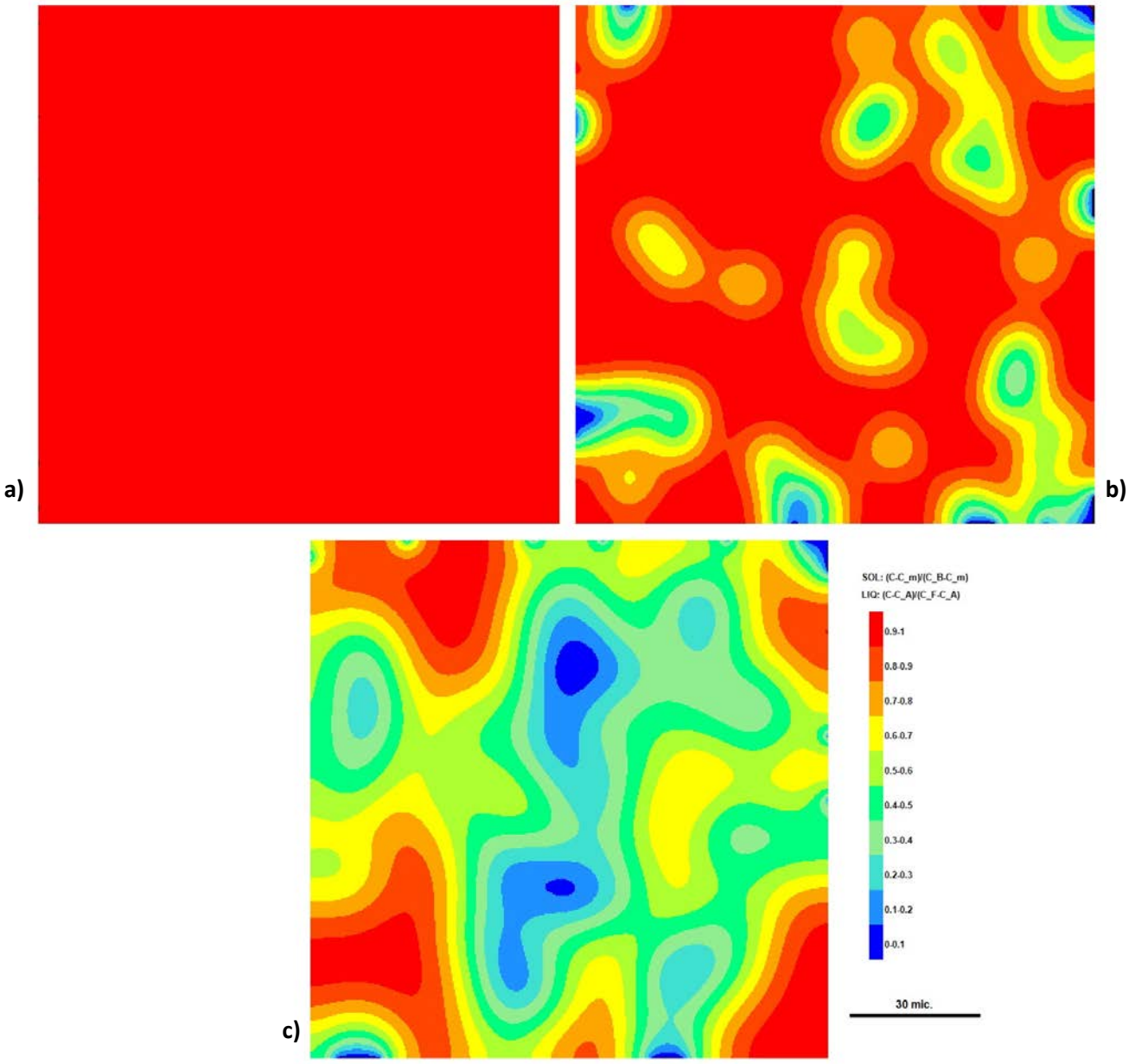

Figure 4. 28: Numerical simulation results showing the MPD solute distribution in the liquid right after complete dissolution of the powder particles for a) Powder-Free Liquid b) $R_{B\text{-}G/F}$ = 9:1 c) $R_{B\text{-}G/F}$ = 7:3

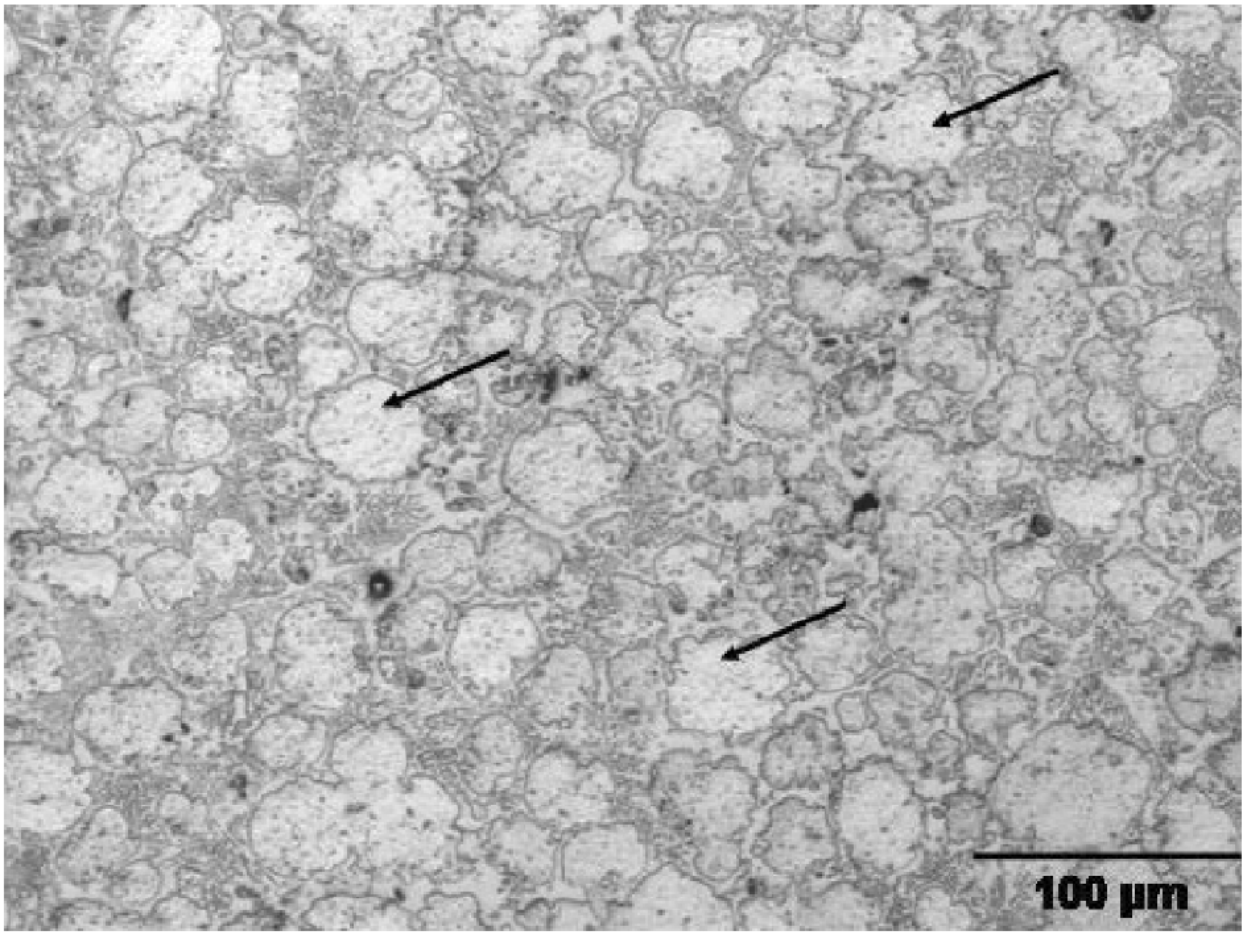

Figure 4. 29: Partial melting of gap-filler powder particles for $R_{B/G-F}$ of 1:1 at 1150^{o}C where the arrows show residual gap-filler powder particles

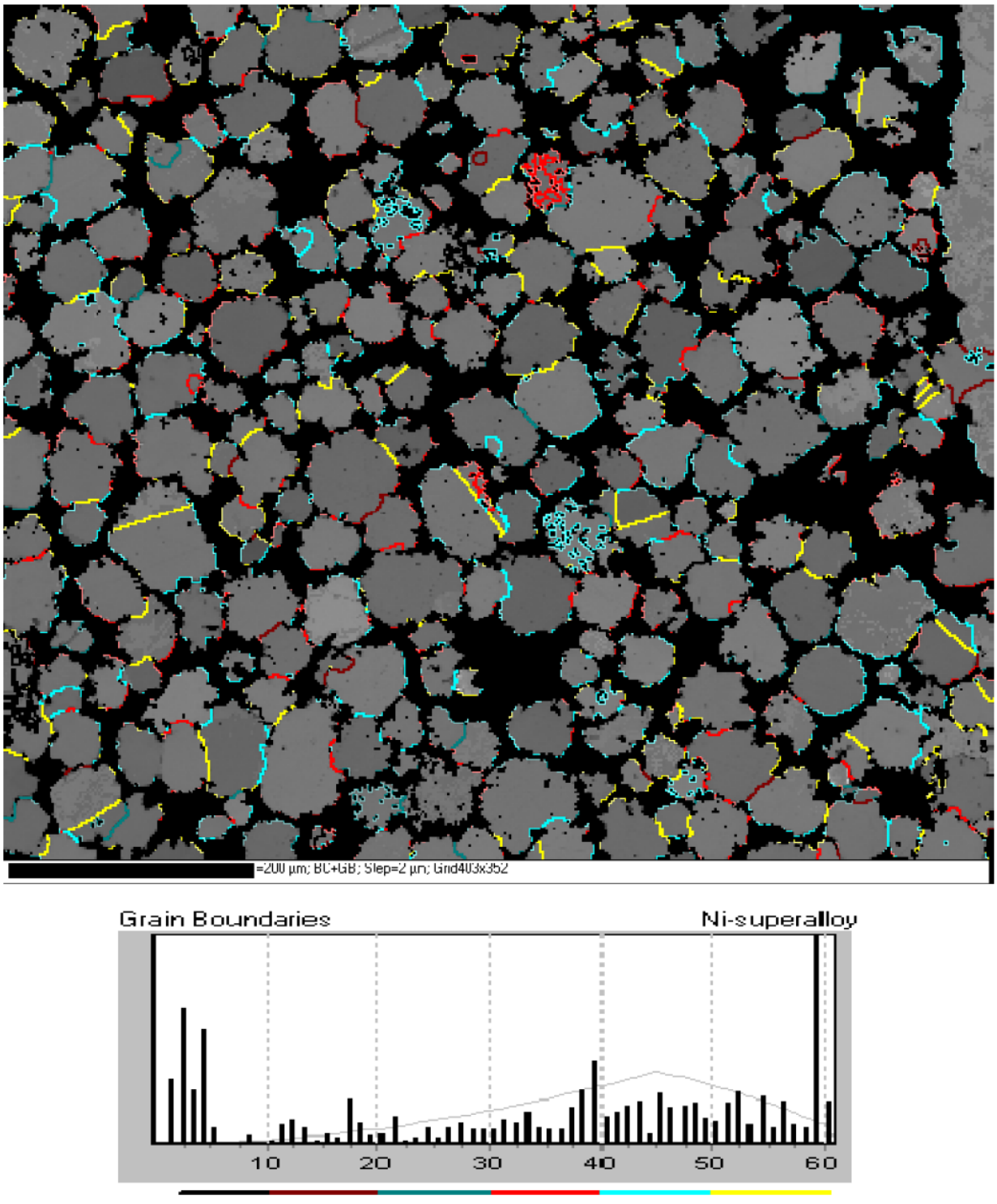

Figure 4. 30: Crystallographic orientation imaging microscopy (OIM) of the residual powder particles for $R_{B/G-F}$ of 1:1 at 1150^{o}C showing the formation of high angle grain boundaries shown in Figure 4.29

a)

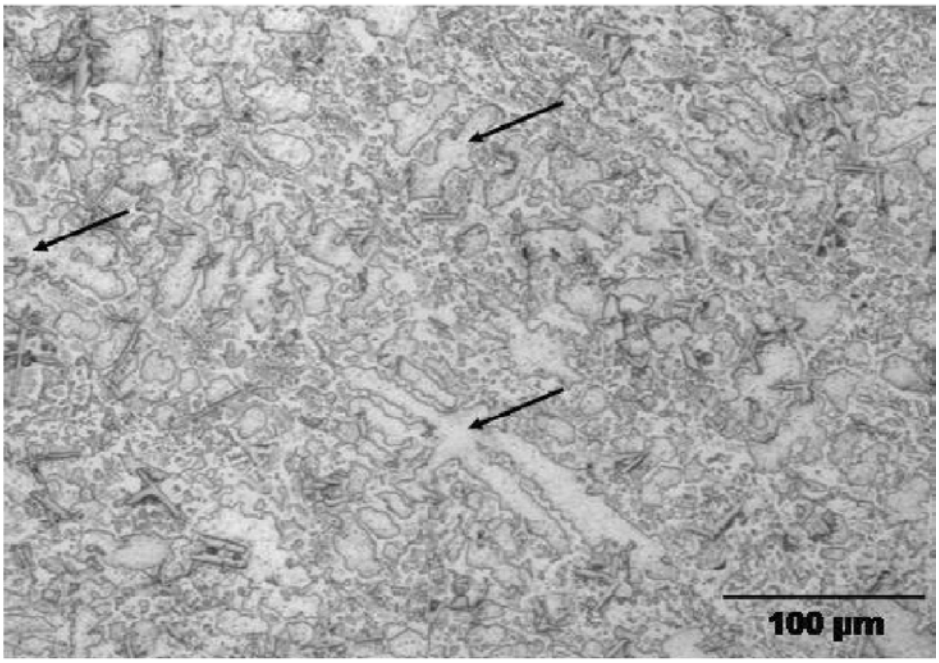

b)

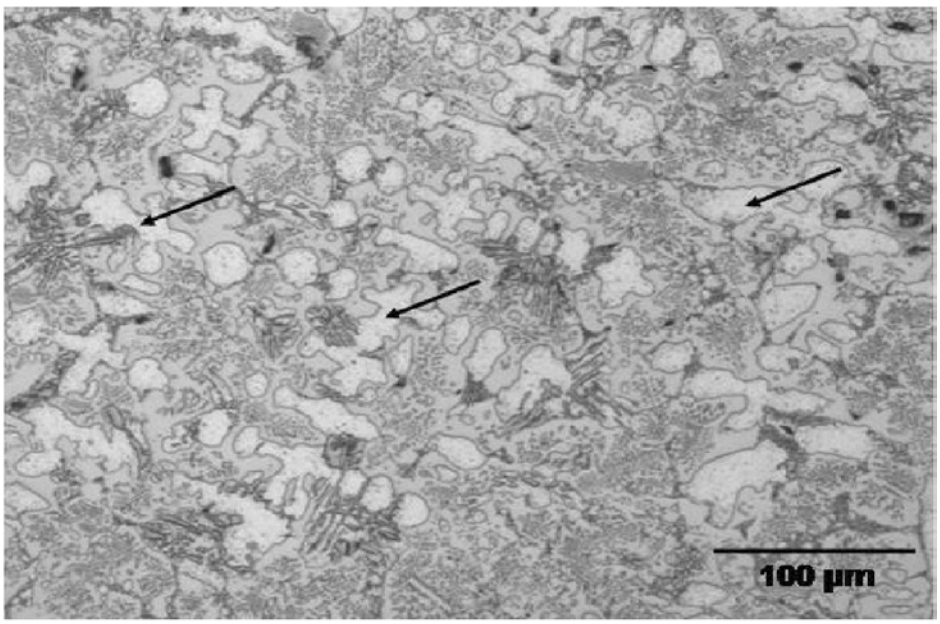

Figure 4. 31: a) Microstructure of completely melted interlayer mixture with an $R_{B/G-F}$ of 7:3 at 1150 ^{o}C. b) Microstructure of completely melted 100% brazing alloy that was free of gap-filler powder particles (the arrows show solidified dendrites)

a)

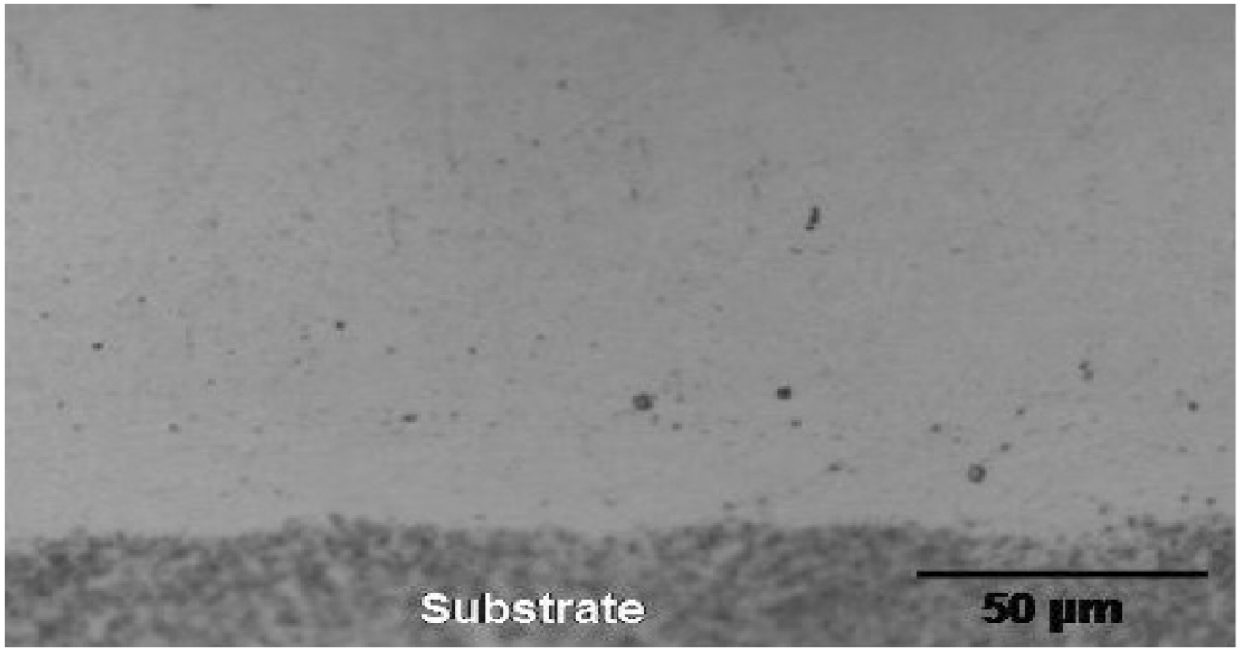

b)

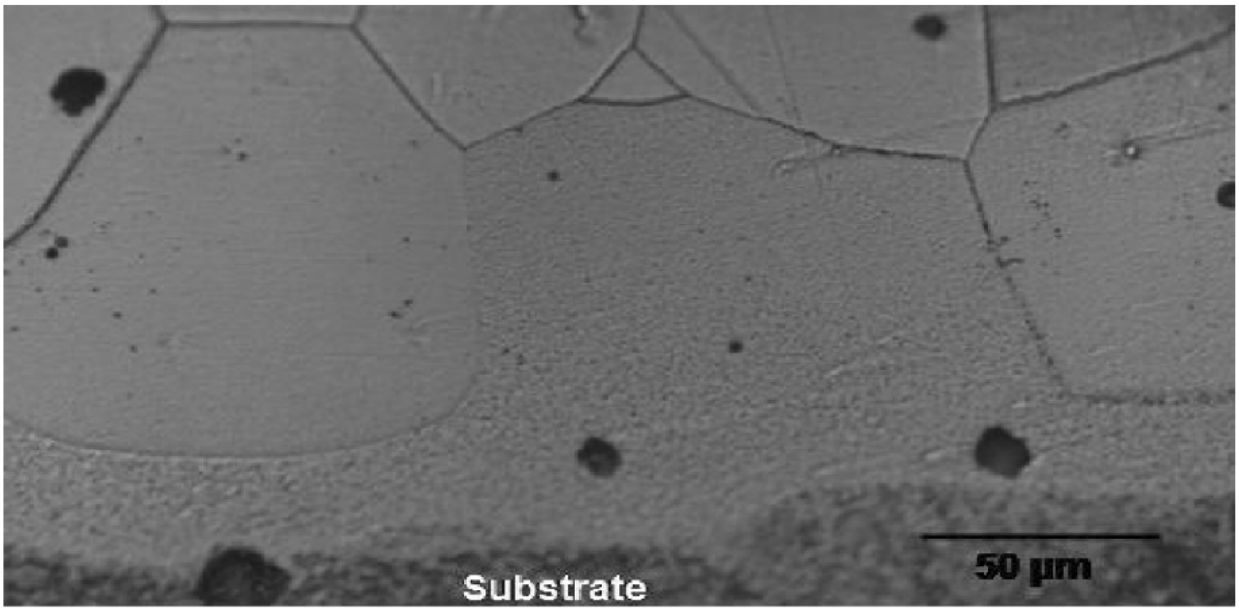

Figure 4. 32: a) Stray-grain free solidified layer produced on single-crystal substrate produced with use of powder mixture with an $R_{B/G-F}$ of 7:3 at 1150 ^{o}C. b) Solidified interlayer containing stray grains on single-crystal substrate produced with use of powder mixture of an $R_{B/G-F}$ of 1:1 at 1150 ^{o}C

a)

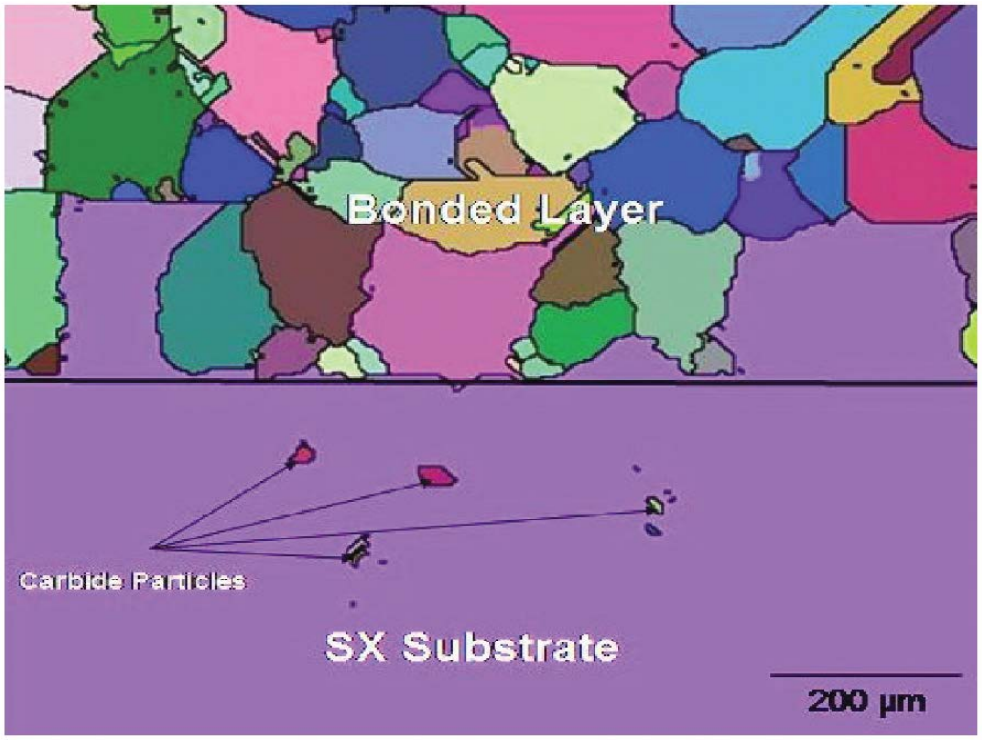

b)

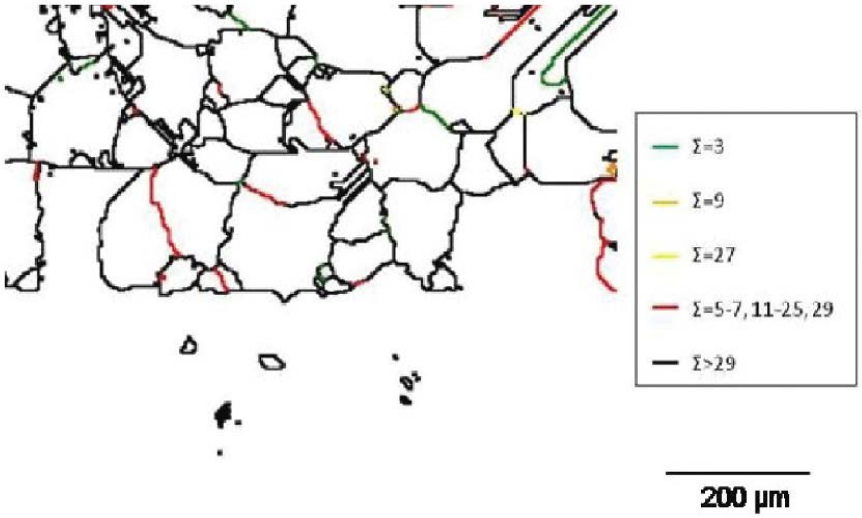

Figure 4. 33 a) Orientation imaging microscopy micrograph showing formation of stray-grains produced on single-crystal interlayer using powder mixture of an $R_{B/G-F}$ of 1:1 at 1150 °C b) Orientation imaging microscopy micrograph showing distribution of coincident site lattice "∑" of grain boundaries in the bonded layer produced using powder mixture with an $R_{B/G-F}$ of 1:1 at 1150 °C

OIM analysis of randomly chosen six points; 1, 2 & 3 in the single crystal substrate, and, 4, 5 & 6 in the bonded layer, made with powder mixture with $R_{B/G-F}$ of 7:3, as shown in Figure 4.34, was performed to evaluate crystallographic alignment between the substrate and the bonded layer. Stereographic inverse pole figures along three orientations; the plane of the bonded layer (XO), the surface of the specimen (ZO) and the plane perpendicular to the bonded layer and the specimen surface are shown in Figure 4.35. The analysis shows that for all the directions XO, YO and ZO, the six points were projected at nearly the same location within the stereographic inverse pole figures. In addition, the {100}, {110} and {111} stereographic pole figures that include all the analyzed six points are shown in Figure 4.36. Moreover, the measured mis-orientation angle between points 1 and 4, for example, was found to be less than 1^{o}. The OIM results, confirm epitaxial solidification of the completely melted powder mixture with an $R_{B/G-F}$ of 7:3 at $1150^{o}C$, which resulted in a stray-grain-free isothermally solidified bonded layer. Similarly, OIM mapping confirmed formation of a joint exhibiting matching crystallographic orientation with the base-material, when the power mixture with an $R_{B/G-F}$ of 7:3 was used as the interlayer material at $1150^{o}C$ (Figure 4.37). An increase in the bonding temperature from $1150^{o}C$ to $1180^{o}C$ resulted in complete melting of the mixture with an $R_{B/G-F}$ of 1:1. The results corroborate the numerical analysis of liquid phase dissolution behavior of the gap-filler powder particles.

In order to investigate the possibility of reducing t_f by using the powder mixture as an interlayer material, TLP bonding of IN 738 superalloy was performed at $1200^{o}C$, which is above the temperature where elongation of t_f occurs in the alloy due to its reversed temperature dependence [112].

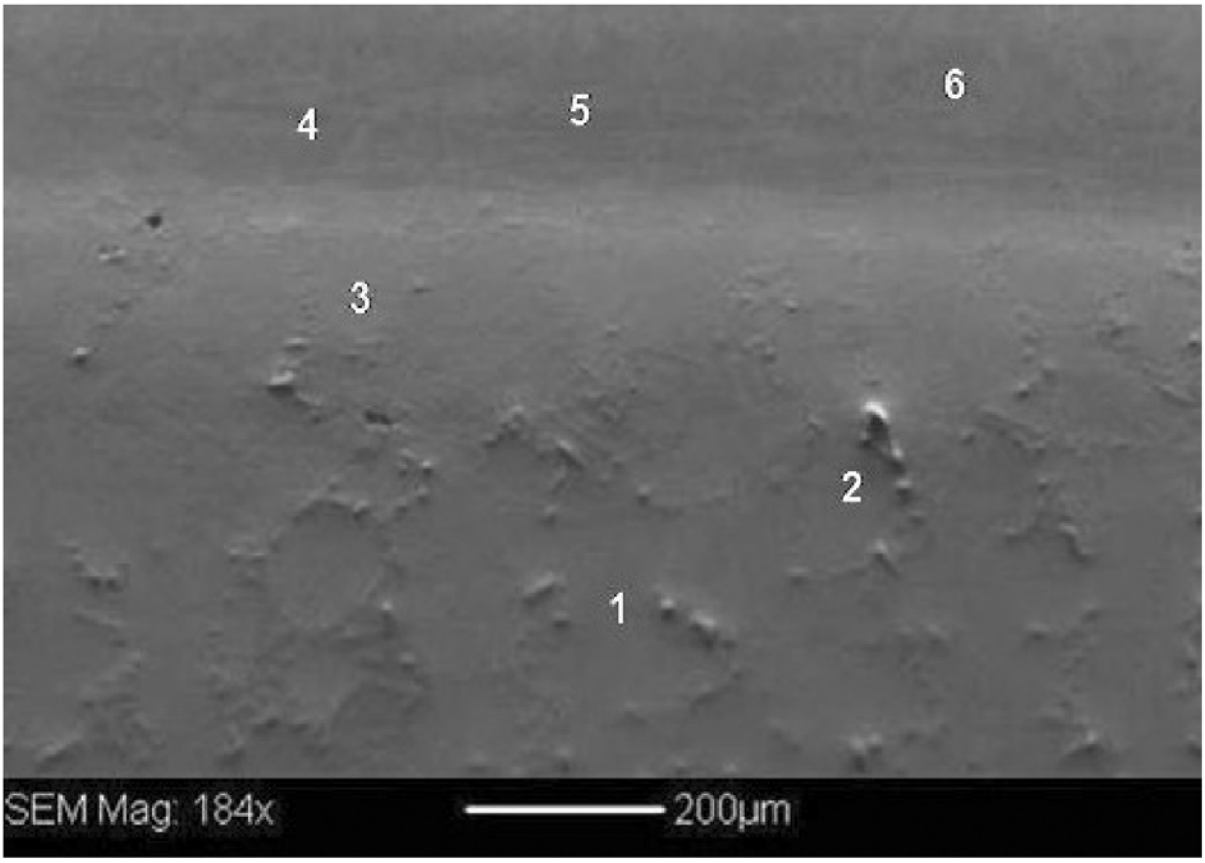

Figure 4. 34: Scanning electron micrograph showing the locations in SX IN738 substrate and bonded layer produced with powder mixture of an $R_{B/G-F}$ of 7:3 at 1150 ^{o}C analyzed by OIM

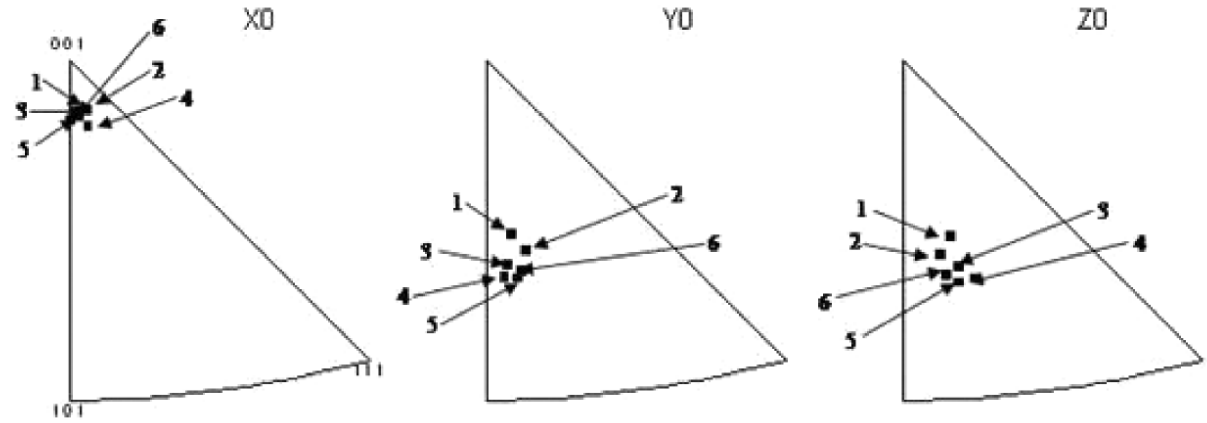

Figure 4. 35: Stereographic inverse pole figures showing the analyzed data points for the locations shown in Figure 4.34

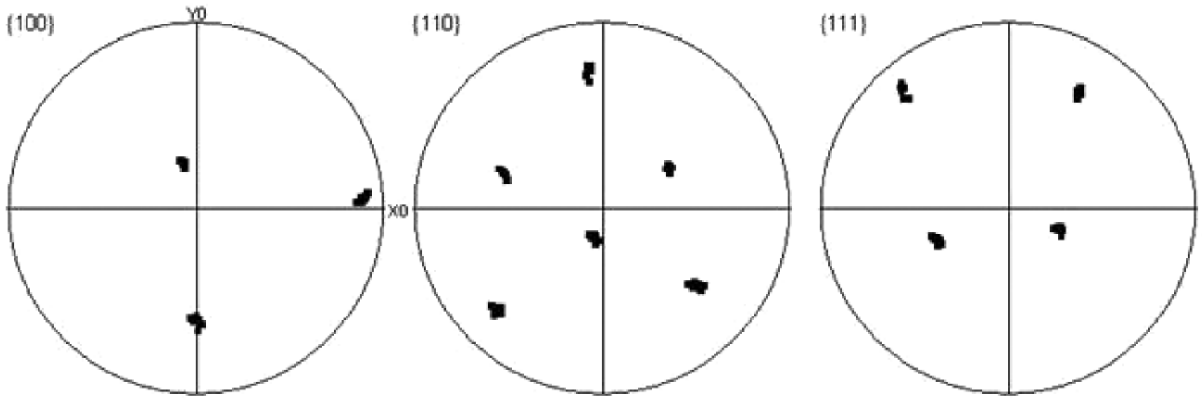

Figure 4. 36: {100}, {110} and {111} stereographic pole figures of the analyzed locations shown in Figure 4.34

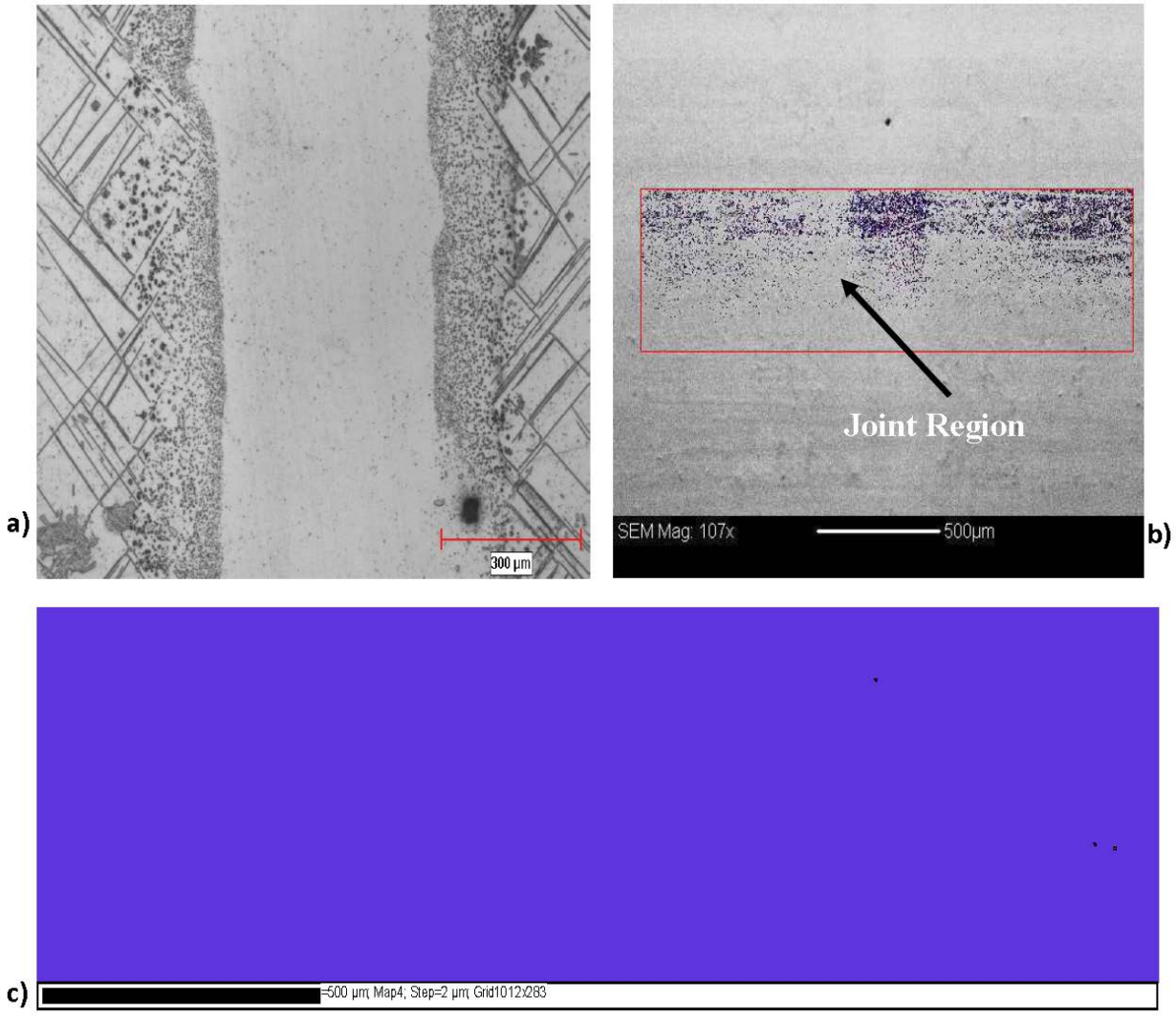

Figure 4. 37: a) SEM micrograph of an etched specimen showing a stray-grain-free joint produced using powder mixture interlayer with an $R_{B/G-F}$ of 7:3 at 1150 ^{o}C in SX IN 738 superalloy base-material. b) SEM micrograph of polished OIM specimen showing the region where OIM mapping was performed on the specimen shown in (a). c) OIM map showing matching crystallographic orientation between the joint and the base-material with the use of powder mixture interlayer material.

Two types of interlayer materials were used for the experiment, (i) interlayer powder mixture with $R_{B/G-F}$ of 1:1 and (ii) 100% of the Ni-Cr-B brazing alloy without the gap-filler alloy. The experimental study showed that up to 30 - 40% reduction in t_f can be achieved with the use of the powder mixture interlayer. The results showed that while 12 hrs of holding time was insufficient to produce a eutectic-free joint through complete isothermal solidification with 100% brazing alloy (Figure 4.38a), 7 hrs of holding time achieved this with the use of the powder mixture interlayer with $R_{B/G-F}$ of 1:1 (Figure 4.38b). To the best of the authors' knowledge, this novel approach of utilizing powder mixture interlayer to minimize t_f without the formation of stray grains has not been previously reported in the literature. Aside from reducing t_f, as predicted by the numerical model, another advantage of using the powder mixture as interlayer material is that it reduces undesirable liquid phase dissolution of substrate material during bonding, which is often referred to as base-material erosion (Figure 4.39). Experimental observations in SX IN 738 and SX CMSX-4 superalloys showed that depending on process parameters, up to 30% reduction in substrate erosion can be achieved by using the powder mixture interlayer. Therefore, the application of the power mixture as interlayer material for TLP bonding of SX materials, shown possible by the theoretical and experimental analyses in this research, is not only beneficial with respect to minimizing $t_{f,}$ but it also reduces substrate erosion, and it enables desirable enrichment of the joint region with gap-filler alloying elements.

a)

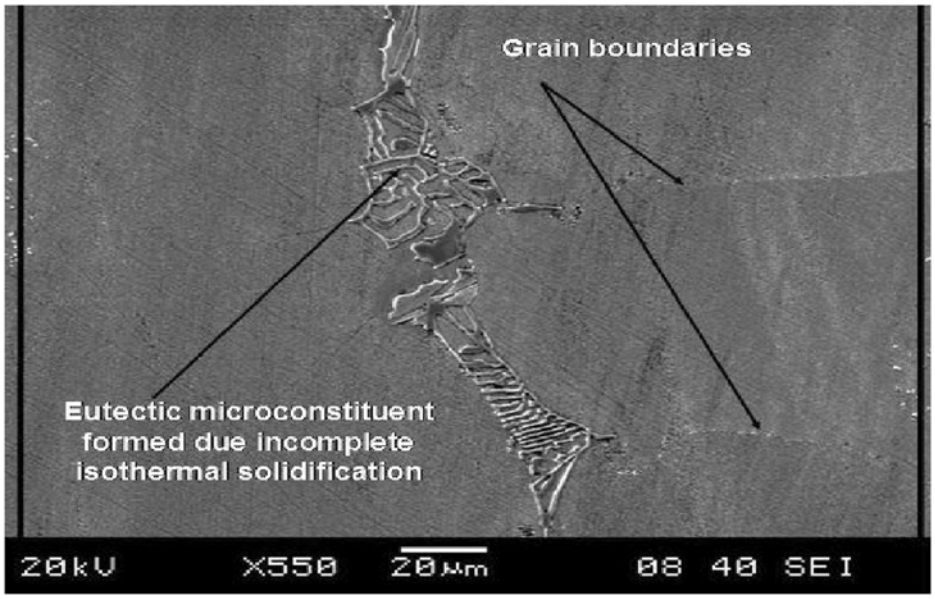

b)

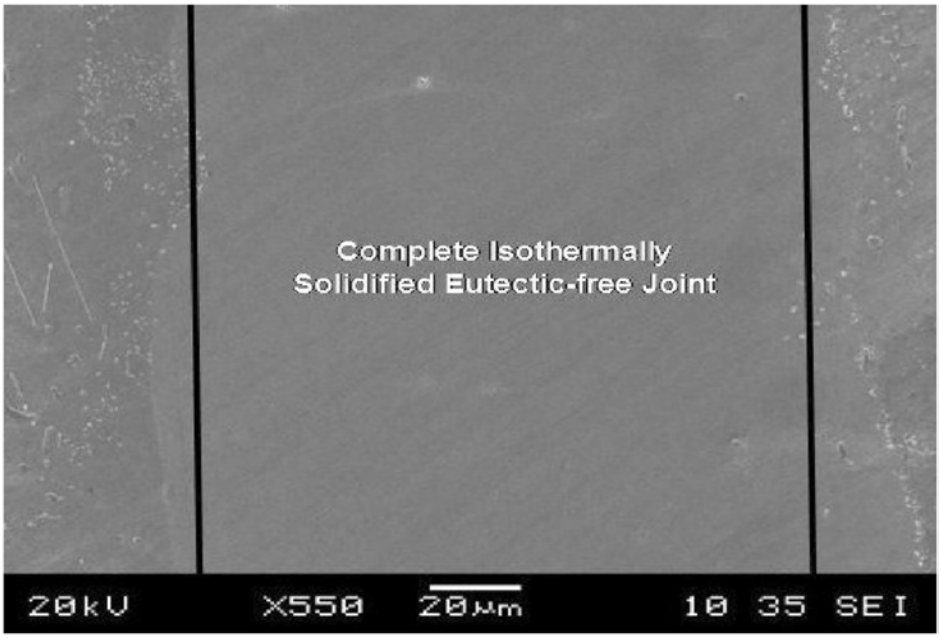

Figure 4. 38: a) Scanning electron microscopy micrograph of the joint produced using 100% brazing filler alloy for 12 h holding time at 1200 ^{o}C. b) Scanning electron microscopy micrograph of the joint produced using interlayer powder mixture with an $R_{B/G-F}$ of 1:1 for a 7h holding time at 1200 ^{o}C

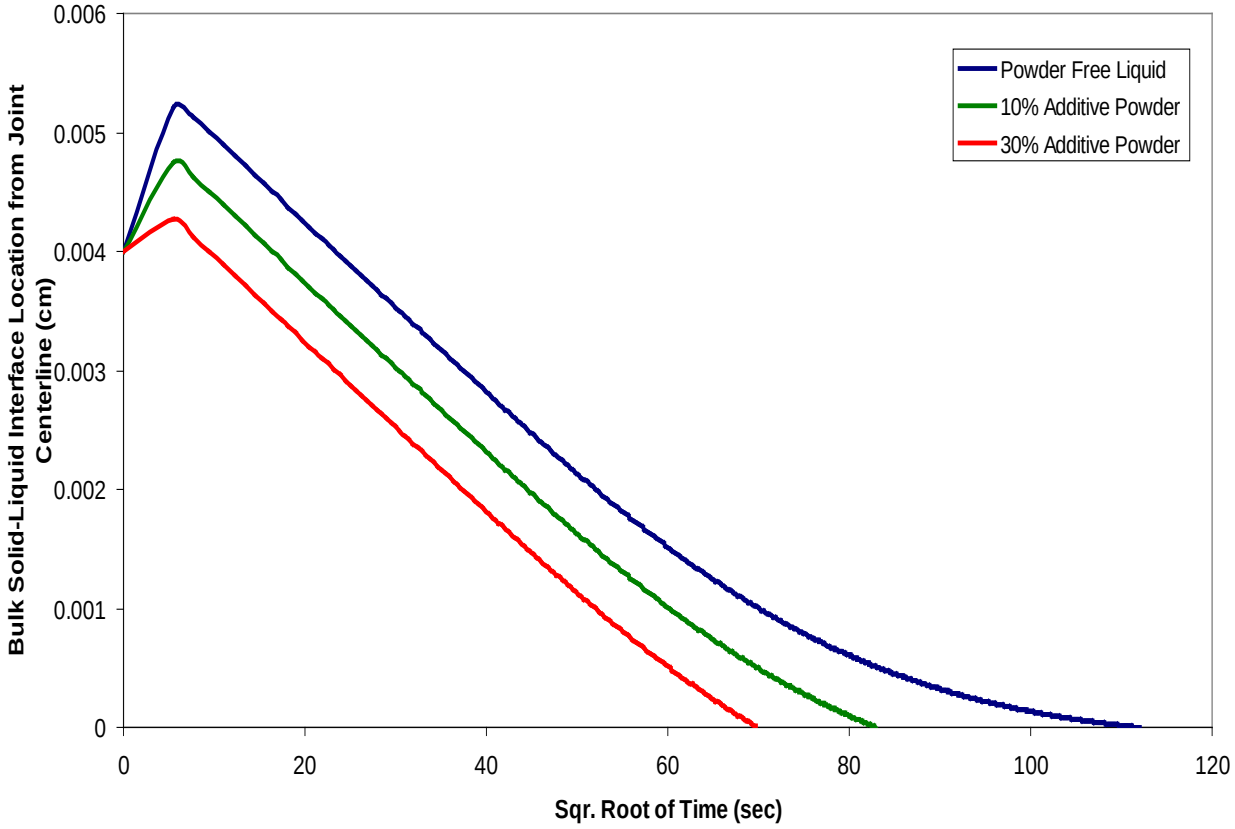

Figure 4. 39: Numerical simulation results showing the effects of powder mixture interlayer on base-material erosion and isothermal solidification completion time

4.3 Application of the New Numerical Model to TLP Bonding of a Ni_3Al-Based Intermetallic Material and TLP Bonding of Dissimilar Materials

4.3.1 Introduction

Conventional heat-resistant structural materials such as Ni-base superalloys that are used in aerospace and power generation gas turbines have nearly reached their upper temperature limit of application and, as such, research has been focused on alternative materials that are lighter and stronger, and have a higher temperature capability than the superalloys. Intermetallic-based alloys and compounds, such as, Ni aluminides, have evolved as prime alternate materials in this regard, and have been the subject of intense study for the past few decades. Welding is generally desired as a joining technique in the fabrication of turbine components and repair of service-damaged turbine parts. A substantial body of research on the fusion welding of intermetallics [117-121] has shown that while high-energy beam-welding techniques such as electron-beam and laser-beam welding are attractive for joining these materials, their application is severely limited by the high susceptibility of the materials to cracking during welding. TLP bonding is being considered as potential alternative for the successful joining and repairing of components made from intermetallics materials.

Among the most investigated various intermetallics for commercial applications are the Ni_3Al-based alloys. A directionally solidified Ni_3Al-based alloy IC 6, with chemical composition of Ni-

15.9Al-7.78Mo (at.%), has been developed at the Beijing Institute of Aeronautical Materials as a high-temperature structural material for manufacturing advanced jet-engine components. It has been successfully tested as turbine-vane material in two different types of aero-engines [122]. It exhibits superior creep-rupture resistance properties, and can withstand higher temperatures (1050-1100^{o}C) than the majority of the currently used Ni-base superalloys. Applicability of the new numerical model developed in this work to understand TLP bonding behavior in this alloy was investigated and the results are presented and discussed in the first part of this section of the thesis (in sub-section 4.3.2).

In addition, a major attractive potential of the TLP bonding process is its capability to produce high performance joints in dissimilar materials, if properly optimized [119]. Despite the potential for joining dissimilar alloys, optimization of the process is presently limited. This is largely due to the lack of appropriate theoretical models for simulating and understanding the complicated influence of a number of interdependent variables. Most of the theoretical simulation models available in the literature on TLP bonding necessarily assume symmetry and similar material properties between two adjacent solid substrates, which are, thus, unsuitable for studying dissimilar alloys with different solute diffusivity, solubility and grain boundary distribution. The unavailability of suitable models has limited the understanding of TLP bonding of dissimilar materials. Therefore, the versatile 2-D numerical simulation model, without inherent symmetry assumption, developed in this research was used to study and understand the influence of material and process variables on the kinetics of diffusional solidification, which controls the formation of deleterious eutectic, during TLP bonding of dissimilar alloys. The results of the dissimilar bonding are presented and discussed in this section of the thesis (in sub-section 4.3.3.)

4.3.2 TLP Bonding of SX Intermetallic Alloy IC 6

4.3.2.1 Microstructure of TLP Joint in Bonded SX Alloy IC 6

Figure 4.40 shows the microstructure of a TLP joint prepared at 1100 ^{o}C for 30 mins in a boron-free (BF) alloy IC 6. A continuous eutectic microconstituent can be observed along the centerline region of the joint. Scanning electron microscopy semi-quantitative EDS compositional analysis indicated that the eutectic consisted of nickel rich boride phase, chromium rich boride phase and nickel-base constituent similar to isothermally solidified pro-eutectic constituent. During TLP bonding, the filler alloy melts and rapidly attains equilibrium with the solid substrate. Inter-diffusion of alloying elements between the base material and the liquid subsequently increases the melting point of the liquated insert and, thus, results in its isothermal solidification. As isothermal solidification progressed, the volume of the liquid decreases and the solid-liquid interface recedes toward the center of the joint. Insufficient holding time for boron diffusion to achieve complete isothermal solidification would result in residual liquid transforming into centerline eutectic microconstituent.

A schematic is shown for the liquidus projection of the nickel rich portion of Ni-Cr-B ternary phase diagram according to Villars et al. [123] in Figure 4.41. According to the diagram, while Ni rich and Cr rich borides are possible products of univariant eutectic-type reactions, the lowest solidification temperature in the system is at point E_2 on the diagram, where solidification terminates by an invariant ternary eutectic reaction producing Ni rich boride phase, Cr rich boride phase and Ni rich solid solution.

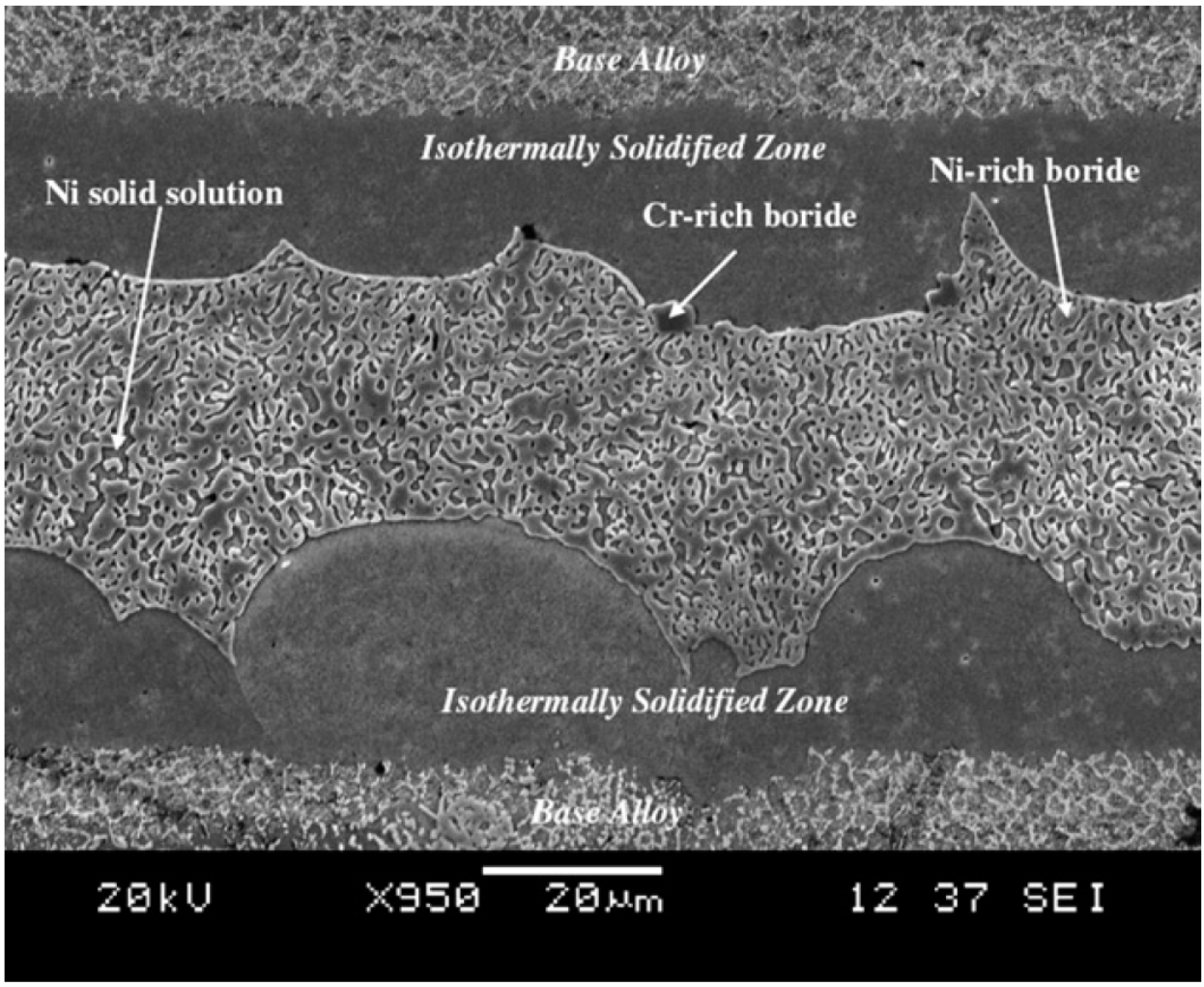

Figure 4. 40: Micrograph of a joint prepared at 1100 ^{o}C for 30 min in BF alloy IC6 showing presence of centerline eutectic microconstituent

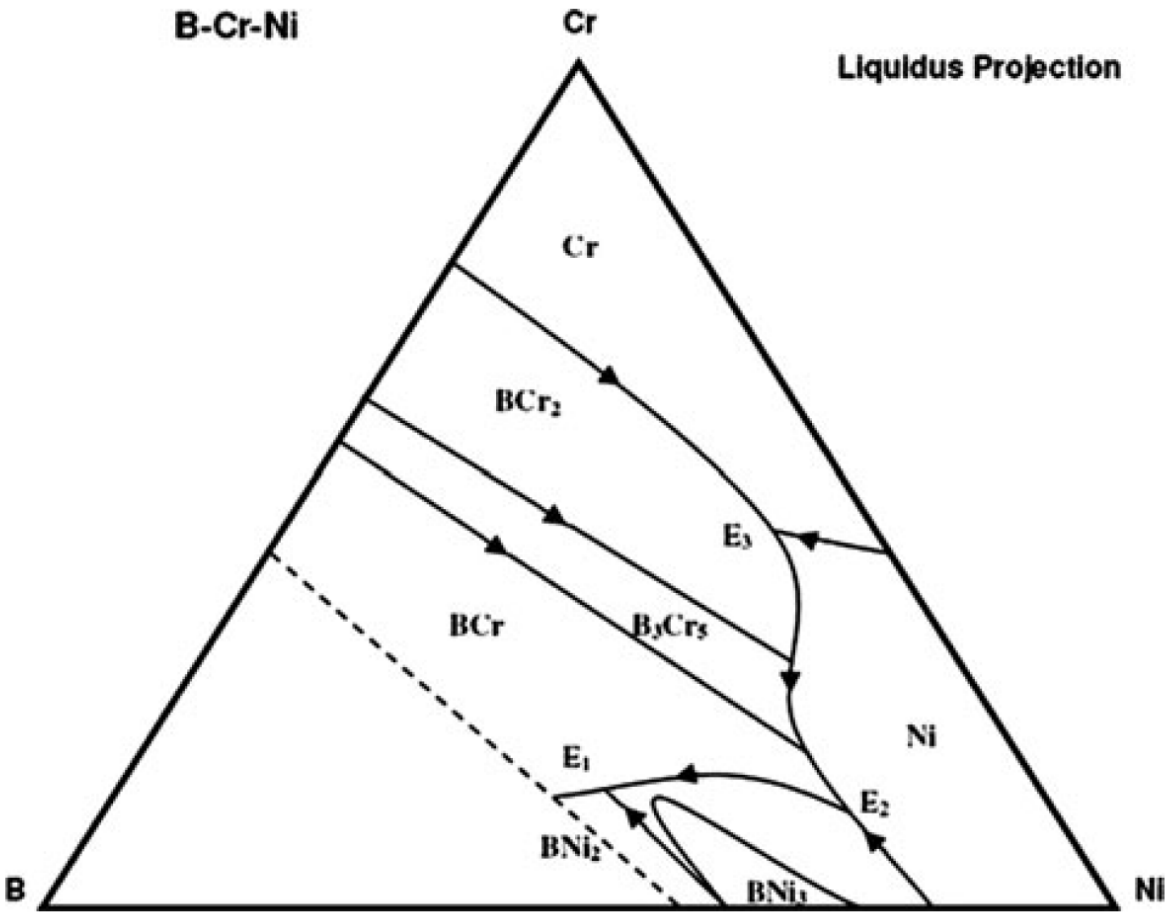

Figure 4. 41: Schematic projection of Ni-Cr-B ternary system [123]

The terminal solidification temperature is below the bonding temperature used in the present work. Moreover, the solidification transformation behavior of residual liquid during diffusion bonding of Ni using a Ni-B-Cr ternary filler alloy was studied and modeled numerically using Scheil simulation by Ohsasa et al. [124]. A ternary centerline eutectic, consisting of Ni base solid solution phase (γ), Ni boride (Ni_3B) and Cr boride (CrB), was found in bonded specimens. Their simulation results showed that during solidification of the residual liquid in a sample held at 1100°C, the Ni-rich γ phase formed as the primary phase, followed by the eutectic reaction $L \rightarrow \gamma + Ni_3B$ at 1042°C. Solidification was reported to be completed with a ternary eutectic reaction $L \rightarrow \gamma + Ni_3B + CrB$ at 997°C. A detailed transmission electron microscopy study performed to confirm the nature of the eutectic formed in the alloy IC 6 showed that it consisted of γ, M_3B_2 and $M_{23}B_6$ [125]. The centerline eutectic is generally known to be deleterious to both mechanical and corrosion properties of TLP bonded materials. Based on the principle of TLP bonding, it is possible to prevent the formation of deleterious centerline eutectic by using sufficient holding time t_f to achieve complete isothermal solidification of the liquated insert.

The present numerical model was used to estimate the time t_f required to prevent the formation of centerline in an 80 μm gap size joint at 1100^{o}C bonding temperature. The predicted time was 3.38 h and experimental verification showed that a 3 hrs holding time resulted in eutectic-free joint in alloy IC 6 (Figure 4.42), which confirmed the prediction of the numerical model.

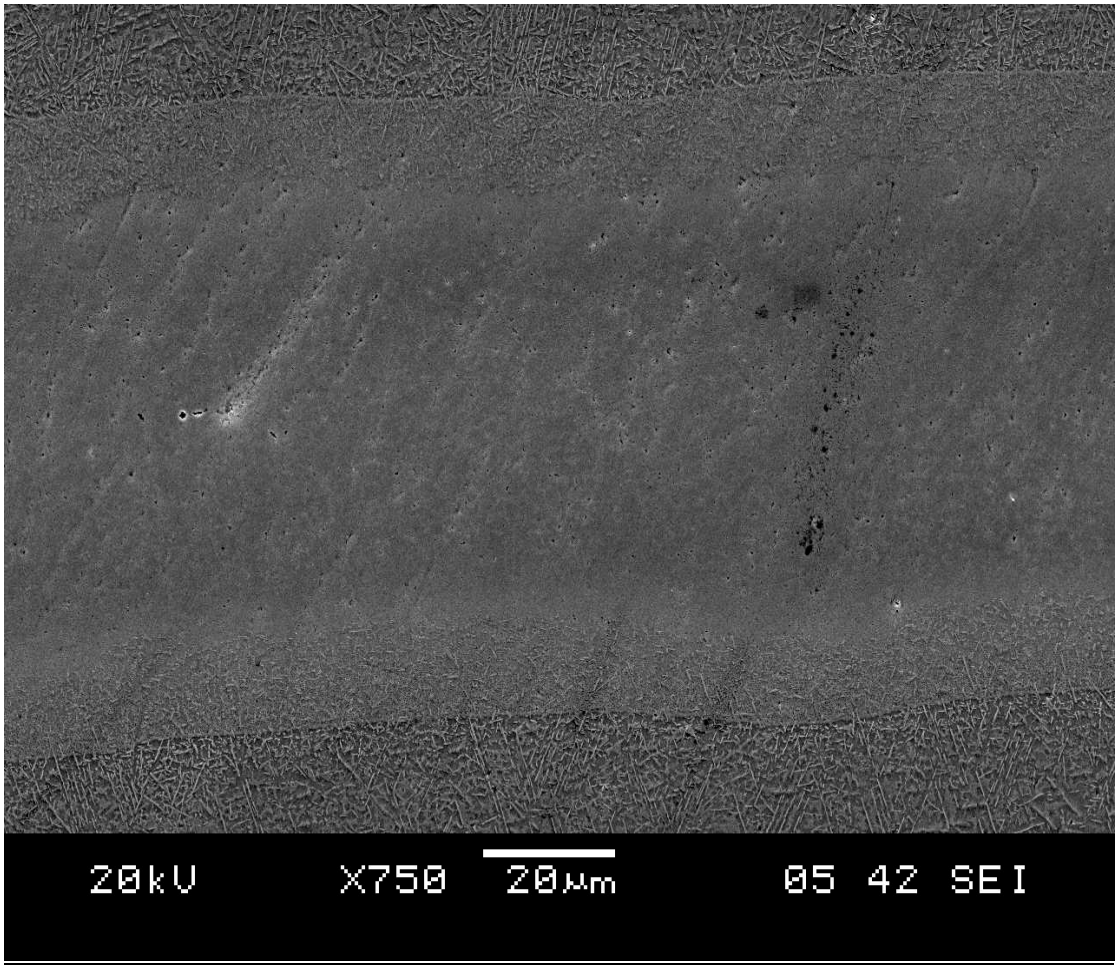

Figure 4. 42: Micrograph of a joint prepared at 1100 ^{o}C for 3 h showing complete isothermal solidification in BF alloy IC6

4.3.2.2 Effect of Boron Addition on t_f in SX alloy IC 6

The addition of boron to Ni_3Al-based intermetallics, including alloy IC 6, is often desired to improve their high temperature creep properties. A review of the literature showed that very limited studies have been reported on the influence of base-material chemical composition on time t_f. According to current TLP bonding diffusion-based mathematical models, boron addition is beneficial for enhancing high temperature performance of Ni_3Al-based intermetallics; it will, however, render the application of TLP bonding for joining of materials unattractive, due to prohibitively long time t_f required to produce a reliable TLP joint. To investigate the influence of boron addition on the rate of isothermal solidification, and thus, on t_f, a numerical simulation of Ni base materials with 0 and 0.05 at% of initial boron concentration, C_m, was performed at 1100^{o}C for a gap size of 80 μm and the result is presented in Figure 4.43a. From the predicted behavior on the plot, a slight addition of 0.05 at% boron would cause a considerable reduction in the rate of isothermal solidification such that the time, t_f, required to prevent formation of centerline eutectic by complete solidification increases by a nearly a twofold value (3.5 vrs. 6.3 hrs). The rate reduction is attributable to a decrease in boron concentration gradient in the base-material due to the initial addition of 0.05 at% boron (Figure 4.43b). As discussed in section 4.1 diffusion controlled isothermal solidification rate during TLP bonding is not only dependent on diffusion coefficient, but also on concentration gradient in the base-material which is influenced by the initial solute concentration. To experimentally verify the validity of the theoretical model prediction, with regard to the effect of boron addition on t_f, a boron-bearing (BB) SX alloy IC 6 was TLP bonded and the results were compared with those obtained with boron-free (BF) SX alloy IC 6.

a)

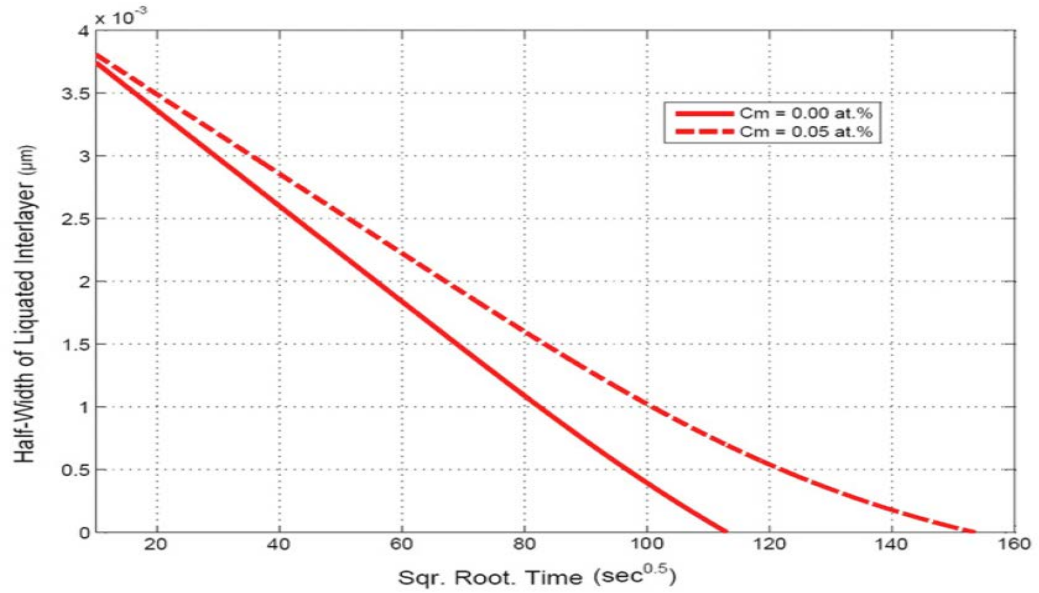

b)

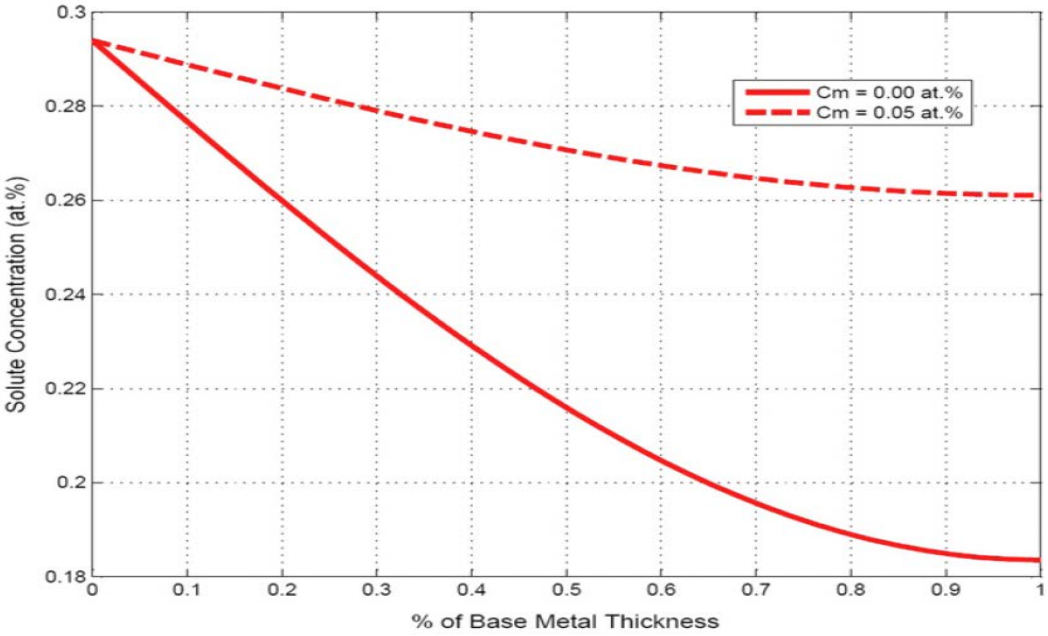

Figure 4. 43: a) Numerically simulated plot of variation of half-width of liquated interlayer with square root of holding time in boron-free and boron-bearing base material at 1100 ^{o}C. b) Numerically simulated plot for concentration profile of boron in boron-free and boron-bearing base materials after bonding at 1100 ^{o}C

In the experimental observation for the BB alloy IC 6 with an addition of 1.18 at% boron (more than 20 times the boron content used in the simulation, which was .05 st.%) significantly departed from the theoretical prediction, as the centerline eutectic widths and complete isothermal solidification times are comparable in the BB and BF alloy IC 6. The deviation from the mathematical model prediction can be understood by the boron distribution during the directional solidification of the cast BB alloy IC 6. An important event that takes place during solidification of alloy castings is the elemental microsegregation between solidified dendrites and the interdendritic liquid. The ratio of dendrite core solute concentration to that of the liquid phase yields the elemental partitioning coefficient, k, which describes the extent and direction of microsegregation of a particular element. Values of k that are less than unity indicate that the dendrite cores are depleted in a particular alloying element relative to interdendritic regions, while values higher than unity indicate dendrite enrichment. An increase in the concentration of alloying elements with $k < 1$ generally reduces the final solidification temperature [126]. Secondary solidification microconstituents form in interdendritic regions when the primary solidification phase can no longer accommodate the composition imposed on it by microsegregation-induced enrichment of the liquid. Formation of such second phase particles is thermodynamically and structurally favored to relieve the interdendritic liquid supersaturation. The binary Ni-B phase diagram indicates that the equilibrium value of k for B in Ni is significantly smaller than one [127] and an experimental study has also showed that Mo, which is known to have high affinity for B, also exhibits k value less than unity in alloy IC 6 [117]. Preferential microsegregation of Mo and B into the liquid during directional solidification of alloy IC 6 ingot casting has been reported to result in the formation of Mo-rich boride particles in isolated interdendritic regions by terminal solidification reaction [128]. Interdendritic second

phase particles that include Mo and B rich particles were also observed in the cast base-alloy used in the present work (Figure 4.44a). The Application of LA-ICP-MS to evaluate the concentration profile of boron in the BB alloy IC 6 confirms depletion of the main matrix of the alloy and its concomitant partitioning into second phase particles (isolated high peaks in Figure 4.44b). Therefore, even though 1.18 at% boron was added to BB alloy IC 6, a general depletion of the alloy in boron, owing to its microsegregation into isolated boride particles, can essentially cause the concentration gradient of boron in the alloy during TLP bonding to be considerably higher than that predicted by theoretical models which assume a uniform boron distribution. This would explain the present experimental result in which the theoretically predicted prolonged isothermal solidification completion time, t_f, in the BB alloy relative to the BF alloy, due to reduced concentration gradients, was not observed. This work, thus, shows that with the addition of boron to improve high temperature properties of a Ni_3Al-based intermetallic alloy IC 6, TLP bonding can still be applied to join the boron-bearing alloy without adversely affecting the time required to achieve reliable joint. Furthermore, applicability of a major theoretical result of the new numerical model developed in this work, possibility of exploiting the benefits of using powder mixture of brazing alloy gap-filler alloy as interlayer material without stray-grain formation, to the SX IC 6 intermetallic material was experimentally verified. The result showed that similar to the case in nickel-base superalloys, powder mixture interlayer material can be used to produced stray-grain free joint and without deleterious eutectic microconstituent, in agreement with the model prediction. Figure 4.45 shows a stray-grain-free joint produced in SX alloy IC 6 with the use of powder mixture interlayer with $R_{B/G-F}$ of 7:3 at 1150 ^oC.

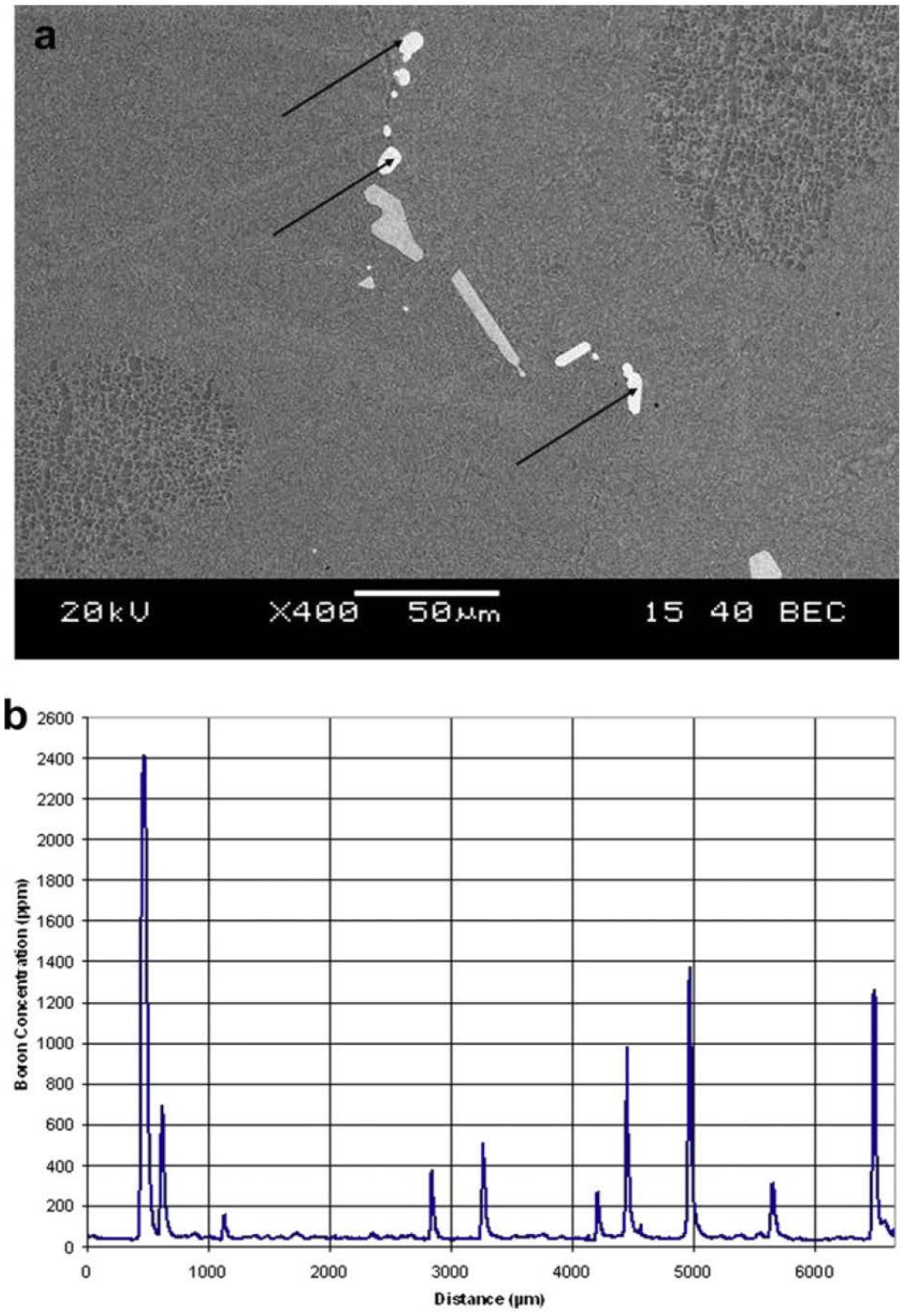

Figure 4. 44: a) SEM backscatter electron image of interdendritic Mo-B rich particles in the cast base alloy. b) Boron concentration profile in as-cast BB alloy IC6 determined by LA-ICP-MS

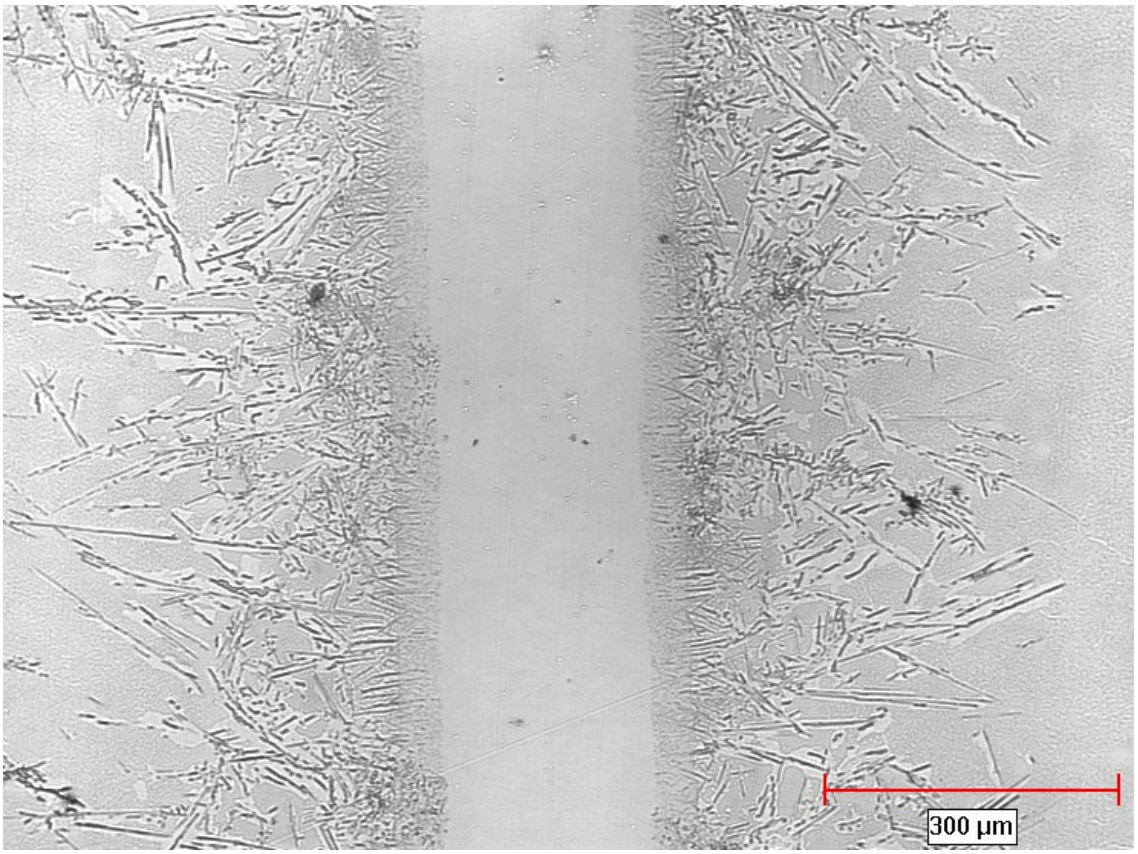

Figure 4. 45: Optical micrograph of showing a stray-grain-free joint produced using powder mixture interlayer with an $R_{B/G-F}$ of 7:3 at 1150 ^{o}C in SX IC 6 intermetallic base-material.

4.3.3 TLP Bonding of Dissimilar Materials

4.3.3.1 Asymmetric Diffusional Solidification during TLP Bonding of Dissimilar Materials

Initial experimental study to verify the applicability of the non-symmetry 2-D numerical model developed in this work to the TLP bonding of dissimilar alloys was performed by using the SX CMSX-4 and IN 738 as the base materials. A preliminary experiment was performed to determine the t_f required to achieve complete isothermal solidification during TLP bonding if IN 738 to IN 738 and CMSX-4 to CMSX-4 by following a similar procedure reported by Nakao et al. [29]. The experimentally determined values of t_f for each of the bonding couples were inserted into the newly developed numerical simulation model to determine the values of apparent activation energy for the diffusion of the MPD solute, boron, in the alloys during joining. The values, 226 kJ/mole in IN 738 and 243 kJ/mole in CMSX-4, are within the range of activation energy values reported in similar Ni-base superalloys in the literature [129]. The activation energy values were subsequently used for the numerical simulation for TLP bonding of dissimilar base materials, IN 738 and CMSX-4. The numerically calculated time required to achieve complete isothermal solidification during the TLP bonding of an 80 μm gap between IN 738 to CMSX-4 was found to be 6.2 hrs and 4.8 hrs at 1100 ^{o}C and 1130 ^{o}C, respectively. The experimental results showed that diffusional solidification of the liquated insert was completed between 6 and 7 hours at 1100 ^{o}C (Figure 4.46) and between 5 and 5.5 hrs at 1130 ^{o}C (Figure 4.47), which are in reasonable agreement with the predicted values 6.2 and 4.8 hrs respectively. The results, thus, indicate that the new numerical model reasonably captures the diffusional solidification kinetics during the TLP bonding of dissimilar materials.

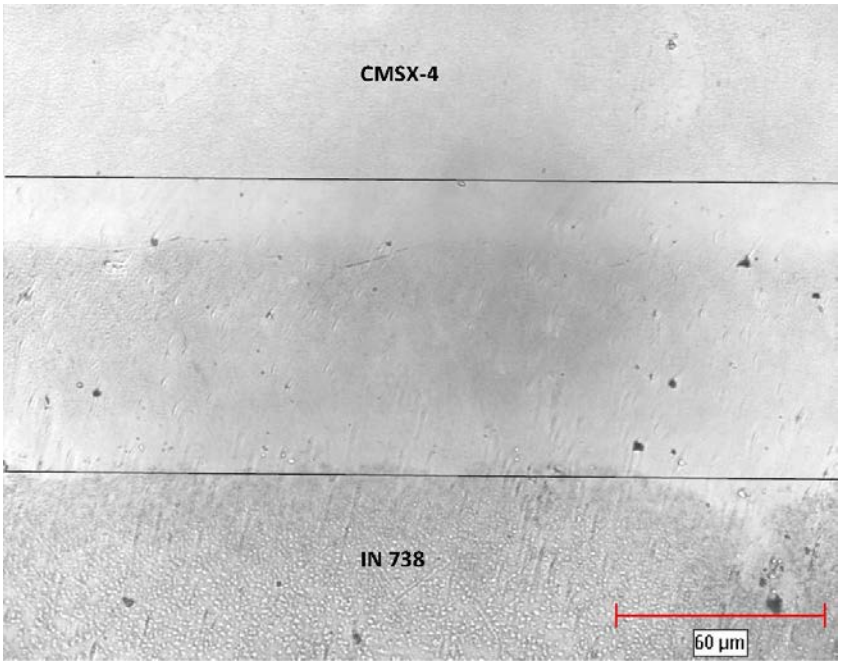

Figure 4. 46: Micrograph of a joint between polycrystalline IN 738 and single crystal CMSX-4 prepared at 1100^{o}C for 7 hours

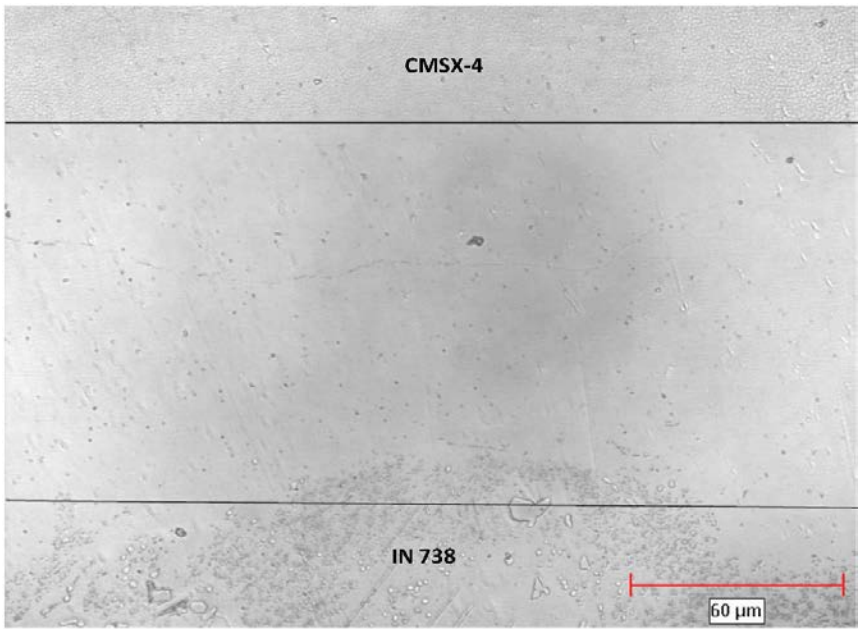

Figure 4. 47: Micrograph of a joint between polycrystalline IN 738 and single crystal CMSX-4 prepared at 1130^{o}C for 5.5 hours

Figure 4.48 shows a SEM micrograph of a joint between a polycrystalline IN 738 and SX CMSX-4 prepared at 1150 ^{o}C for 1 hour, which is shorter than the time required to achieve complete isothermal solidification. A eutectic product formed in the joint due to on-cooling non-equilibrium solidification of the residual interlayer liquid present within the joint after the 1 hour holding time. The eutectic consisted of Ni-rich boride phases, Cr-rich boride phases and Ni-base microconstituent (Table 4.2 & Figure 4.49), which are comparable to those reported in other TLP joints of Ni-base superalloys [125, 130].

As we reported in the other superalloy TLP joints, boron was detected in the chromium-rich and nickel-rich borides observed in the present work, but not quantified due to the inherent limitation of the SEM-EDS in quantifying light elements with sufficient accuracy. The eutectic that is formed during the TLP bonding of similar types of superalloy substrates is generally located at the centerline region of the joint. In contrast, however, the eutectic observed in the present work between the dissimilar base-alloys is located away from the joint centerline region, considerably closer to the CMSX-4 and at a farther distance from the IN 738 substrate (Figure 4.49). A similar observation of the non-symmetrical distribution of the residual interlayer liquid, which transforms to a eutectic product, has been reported in TLP joints between dissimilar superalloys polycrystalline M963 and SX DD98 [100]. The irregular distribution of the interlayer liquid was reported to produce a non-uniform precipitation of the main strengthening phase of the alloys, γ' precipitates, within the joint region. The behavior was attributed to presence of grain boundaries in the polycrystalline substrate M963 and the lack of intergranular regions in the single crystal substrate DD98.

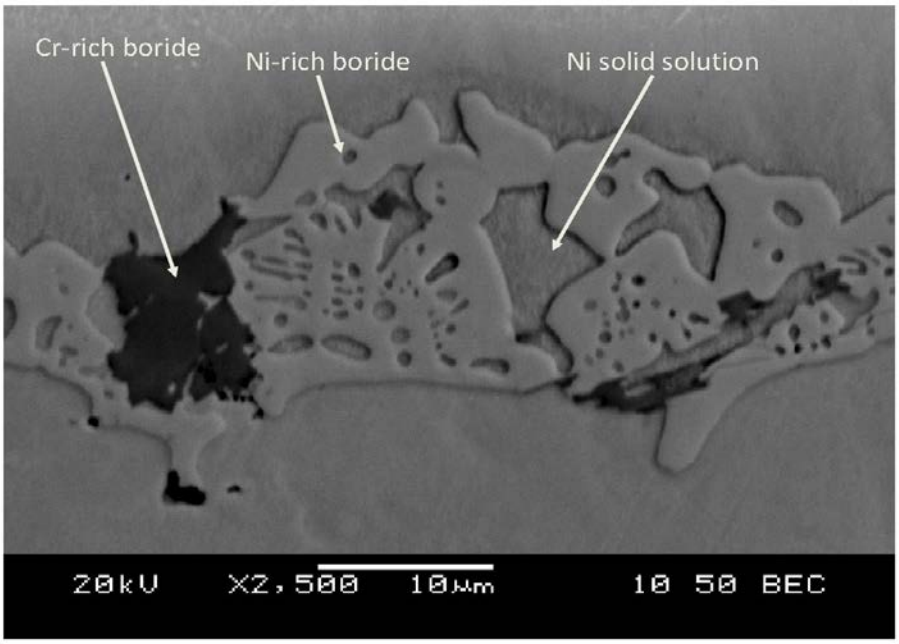

Figure 4. 48: Energy Dispersive Spectroscopy (EDS) micrograph of a joint between polycrystalline IN 738 and single crystal CMSX-4 prepared at 1150^{o}C for 1 hour

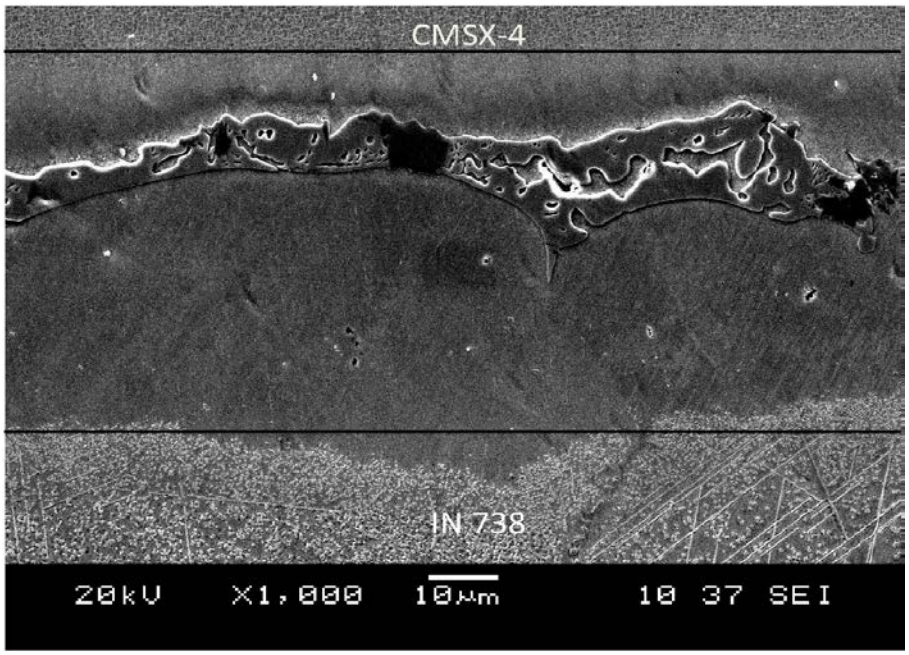

Figure 4. 49: Scanning Electron Microscopy (SEM) micrograph of a joint between polycrystalline IN 738 and single crystal CMSX-4 prepared at 1150^{o}C for 1 hour

Table 4. 2: SEM-EDS semi-quantitative analysis of phases present in within the TLP joint eutectic

	Composition (wt%)					
Phase	Cr	Si	Co	Ti	Al	Ni
Cr-rich boride	65.38	---	0.56	0.27	0.94	32.85
Ni-rich boride	9.95	0.77	2.08	1.57	0.60	85.03
Ni-solid solution	15.43	1.29	2.31	---	0.57	80.40

Nevertheless, it has been recognized that the influence of grain boundaries on diffusion controlled migration of liquid-solid interfaces during TLP bonding cannot be merely attributed to high intergranular diffusivity [95].

The influence of enhanced grain boundary diffusion on the distribution of interlayer liquid between the polycrystalline and SX substrates during TLP bonding of dissimilar materials was simulated with the use of a new 2-D numerical model. The ratio of the grain boundary diffusion coefficient, D_{GB}, to that of the bulk solid lattice, D_S, is about $\leq 10^3$ within the temperature range $T > 0.75\ T_m$ (where T_m is the equilibrium melting temperature in K) [103]. The TLP bonding temperatures are typically higher than $0.75\ T_m$. The effect of increase in the ratio D_{GB}/D_S on the extent of liquid-solid interface displacement during TLP bonding of polycrystal Ni (grain size of 200 μm) to SX Ni with the same value of D_S was numerically simulated. As shown in Figure 4.50, an increase in the intergranular diffusivity did not exact any significant effect on the diffusion-controlled migration of the liquid-solid interface and the residual interlayer liquid was essentially symmetrically distributed between the adjacent solids. In contrast, however, for a set of SX substrates, with different D_S values, D_{S1} and D_{S2} in the adjacent solids, variation in the ratio D_{S1}/D_{S2}, resulted in non-symmetrical distribution of the interlayer liquid (Figure 4.51).

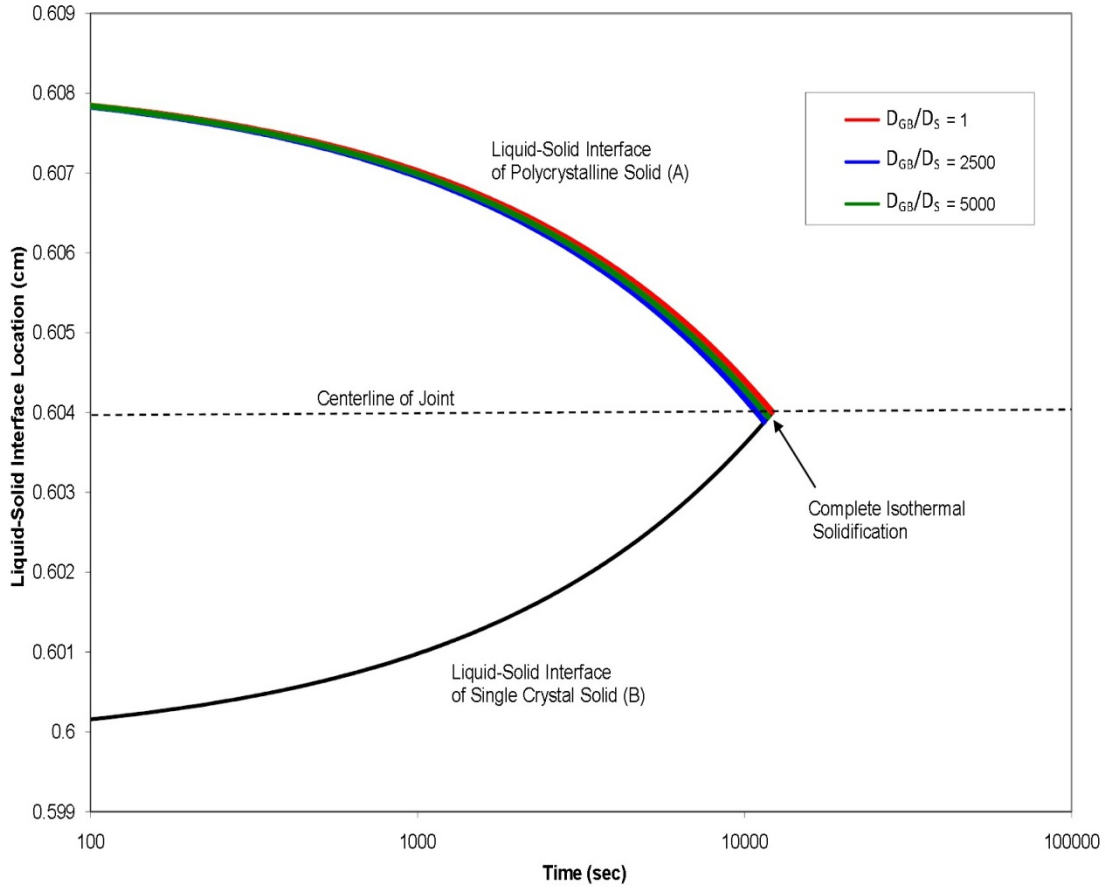

Figure 4. 50: Numerical simulation results of the effect of D_{GB}/D_S Ratio on isothermal solidification completion time and migration rate of the liquid-solid interfaces

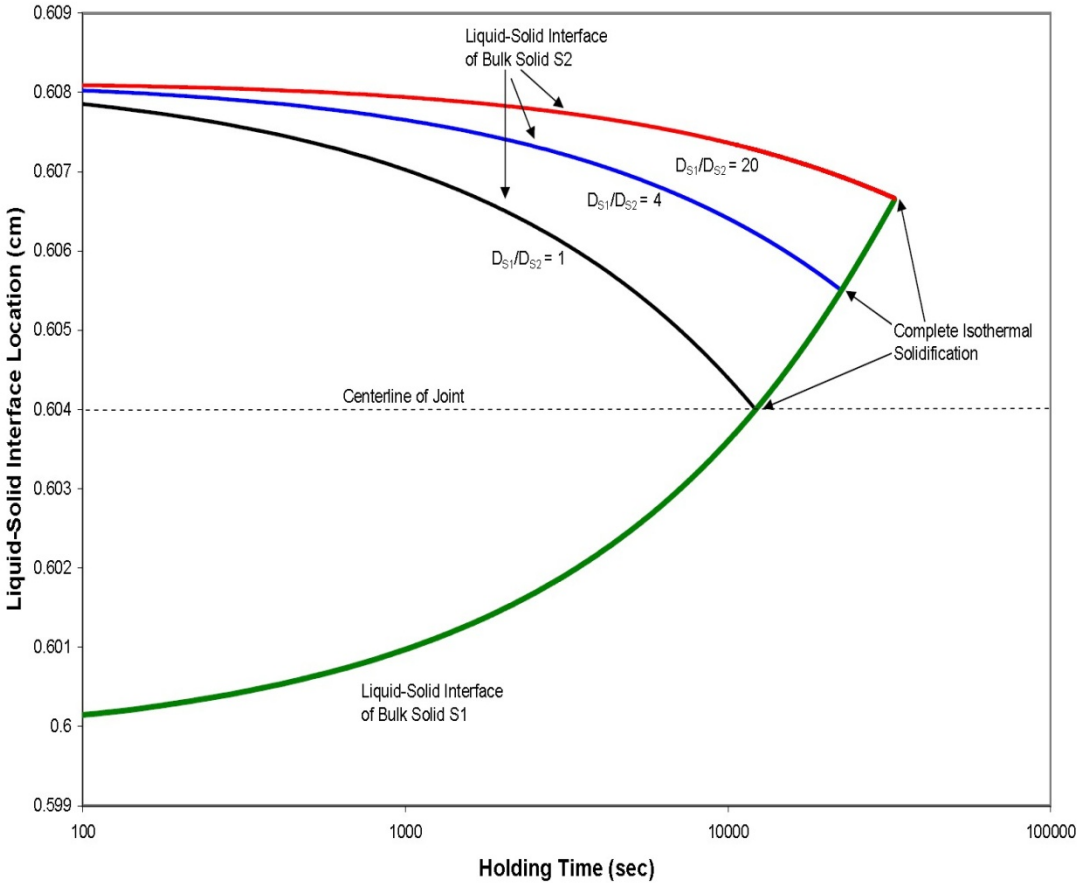

Figure 4. 51: Numerical simulation results of the effect of D_{S1}/D_{S2} ratio on isothermal solidification completion time and migration rate of the liquid-solid interfaces

The numerical calculations showed that instead of enhanced intergranular diffusivity, the asymmetric diffusional solidification behavior can be attributed to the difference between the lattice diffusion coefficients of the MPD solute in the dissimilar base-alloys. The analysis indicates that in contrast to previous assumptions, instead of the presence or lack of grain boundaries, the non-symmetrical distribution of the interlayer liquid is caused by difference in the values of D_S in the adjacent solid substrates. In order to experimentally verify this prediction, TLP bonding was performed between SX IN 738 and SX CMSX-4. Despite the absence of grain boundaries in both single crystal substrates, the disparity in D_S in the dissimilar base-alloys resulted in a non-symmetrically distributed eutectic within the joint region (Figure 4.52). This confirmed the model prediction and showed that asymmetric behavior in diffusional solidification is mainly attributable mainly to a mismatch between the lattice diffusion coefficients in adjacent dissimilar alloys.

Aside from the effect on the resultant joint microstructure, the disparity in lattice solute diffusion can also have a significant effect on t_f. Coupling a base-alloy with a higher D_S to another alloy with a lower D_S value can significantly reduce the t_f compared to the case where the adjacent substrates are of the same alloy with a lower D_S value. This is demonstrated in the case of coupling IN 738 to CMSX-4, where a t_f of about 6 hrs for dissimilar joining at 1100^{o}C was significantly shorter than a t_f of about 12 hrs that is required to join CMSX-4 to CMSX-4 with the same gap size at 1100^{o}C. The t_f required to join IN 738 to IN 738 at the same temperature and gap size was about 3.5 hrs.

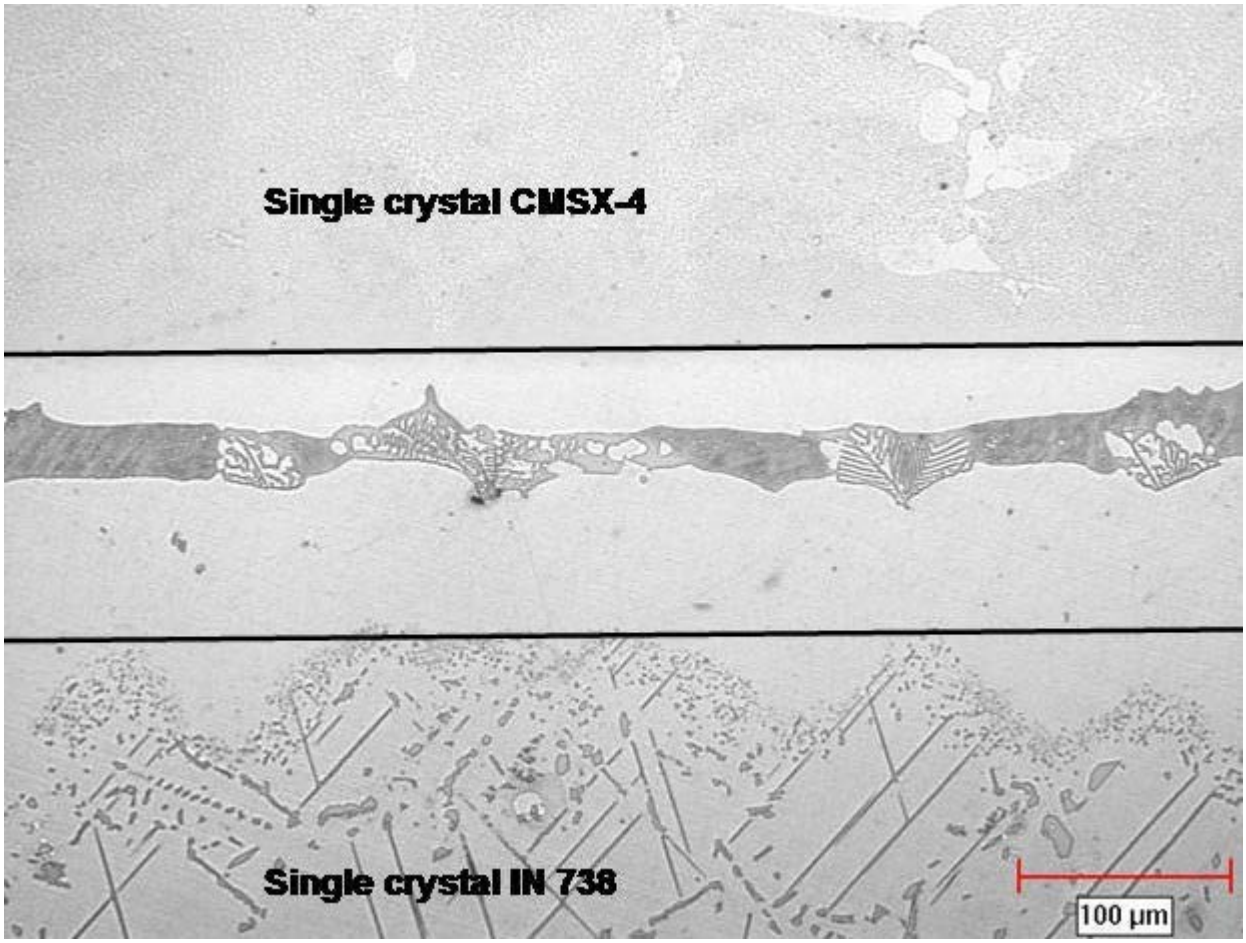

Figure 4. 52: Optical microscopy micrograph of a joint between single crystal IN 738 and single crystal CMSX-4 prepared at 1230 ^{o}C

4.3.3.2 Influence of Solute Solubility on Time t_f during Dissimilar Bonding.

As previously stated, t_f is dependent on a number of material and process variables in a manner that may not be intuitively predicted. The use of an appropriate simulation model is, thus, necessary to gain an adequate understanding of the factors that influence diffusional solidification kinetics during bonding and their interdependence. Similar to joining similar base materials, the anomalous reversed temperature dependence of t_f was also observed during bonding of dissimilar base materials. Experiments showed that an increase in t_f occurs with an increase in temperature during TLP bonding of dissimilar superalloys, IN 738 and CMSX-4 superalloys. For an 80 μm initial gap size between the alloys, as stated earlier, complete isothermal solidification was observed to occur between 6 and 7 hrs at 1100^{o}C bonding temperature (Figure 4.46). An increase in the temperature to 1200^{o}C, however, resulted in a eutectic-free joint after 5-hours of holding time due to the enhanced diffusion which resulted in complete isothermal solidification (Figure 4.53). However, with a further increase in the temperature to 1230^{o}C, a 5 hour holding time was inadequate to achieve complete isothermal solidification, which resulted in eutectic formation within the joint (Figure 4.54). The results showed that t_f initially reduced with an increase in temperature from 1100^{o}C to 1200^{o}C and subsequently increased with an increase in temperature from 1200^{o}C to 1230^{o}C. This type of behavior during TLP bonding of dissimilar materials has not been previously reported in the literature.

As elucidated by numerical analyses and discussed in section 4.2.2 of this thesis the anomalous increase in the processing time t_f with bonding temperature is attributable to deviation from parabolic migration liquid-solid interface with time, which cannot be explained by analytical

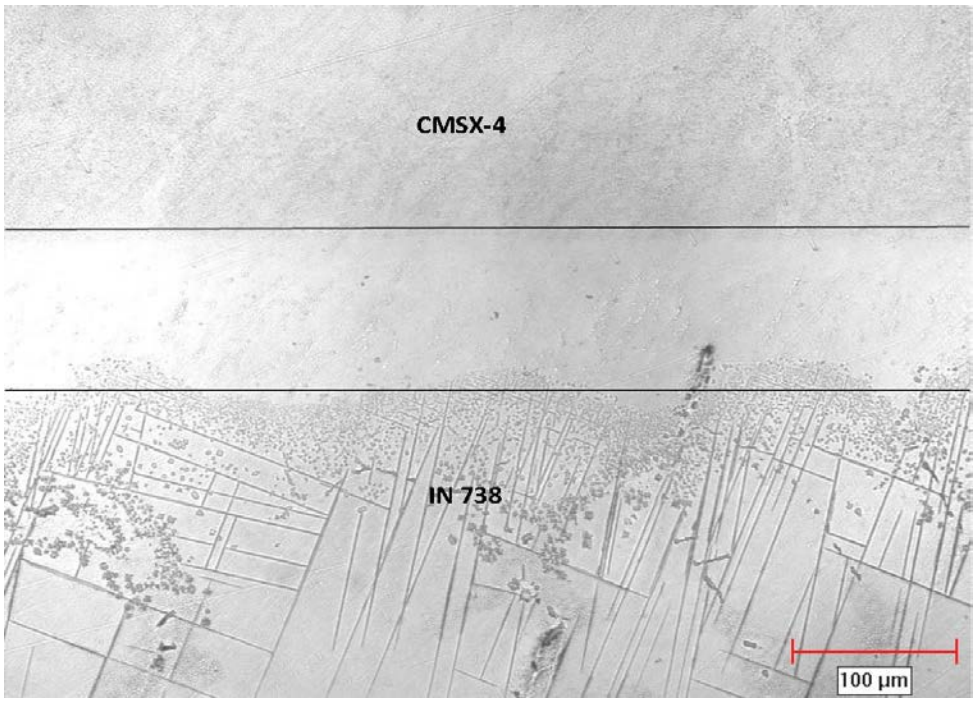

Figure 4. 53: Micrograph of a joint between polycrystalline IN 738 and single crystal CMSX-4 prepared at 1200°C for 5 hours.

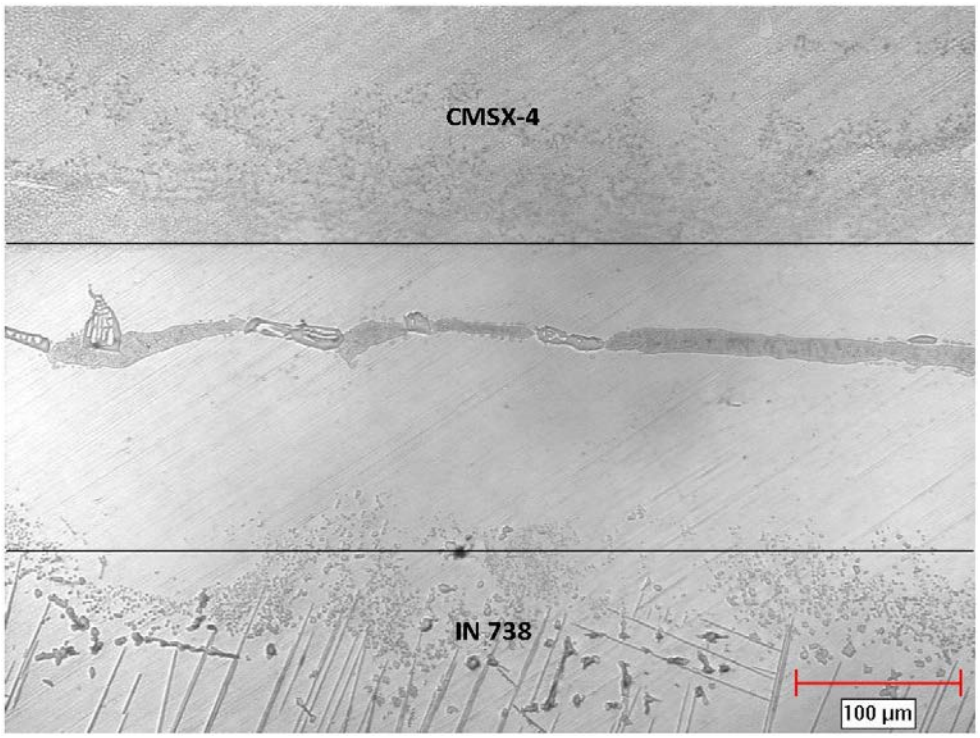

Figure 4. 54: Micrograph of a joint between polycrystalline IN 738 and single crystal CMSX-4 prepared at 1230°C for hours.

TLP bonding models. Consequently, a possible way to prevent or minimize the undesirable increase in t_f at temperatures above T_c during TLP bonding of dissimilar alloys could involve joining a material with another type that has a higher solubility or better capability of accommodating the diffusing MPD solute. The capability of solute accommodation of the base-alloy can be enhanced by depletion of the solute content in the substrate matrix through the formation of solute-rich second phase precipitates. Mo is known to have a high affinity for boron and several Mo-rich borides, such as M_3B_2 and M_5B_3 form in Ni-base alloys [125, 131]. To experimentally investigate the possibility of reducing t_f by this approach, a nickel-base alloy, IC 6, containing 14wt% of Mo, was joined to IN 738, which contains 1.9wt% Mo, by TLP bonding. At 1100^{o}C, the t_f for bonding IC-6 to IC-6 was experimentally observed to be comparable to that required to join IN 738 to IN 738, which is about 3.5 hours for an initial gap size of 80 μm. An increase in t_f was observed when the bonding temperature was increased to 1230 ^{o}C during the joining of IN 738 to IN 738. A holding time of 5 hours was found to be insufficient to achieve complete isothermal solidification in the IN 738 – IN 738 joint at 1230 ^{o}C. In contrast, however, a 5-hours holding time was adequate to achieve complete isothermal solidification when IN 738 was joined to alloy IC-6 at 1230 ^{o}C (Figure 4.55).

The reduction in t_f observed by coupling IC-6 to IN 738, at a temperature above T_c in the latter, may not be attributable to a higher solute diffusivity in IC-6 compared to IN 738, as t_f is comparable in both alloys at lower bonding temperatures. Moreover, as stated earlier, an increase in t_f with temperature due to the phenomenon of deviation from the parabolic rule, is independent of solute diffusivity. The enhanced capability to accommodate boron in the alloy IC 6 could be responsible for the reduced t_f at 1230^{o}C.

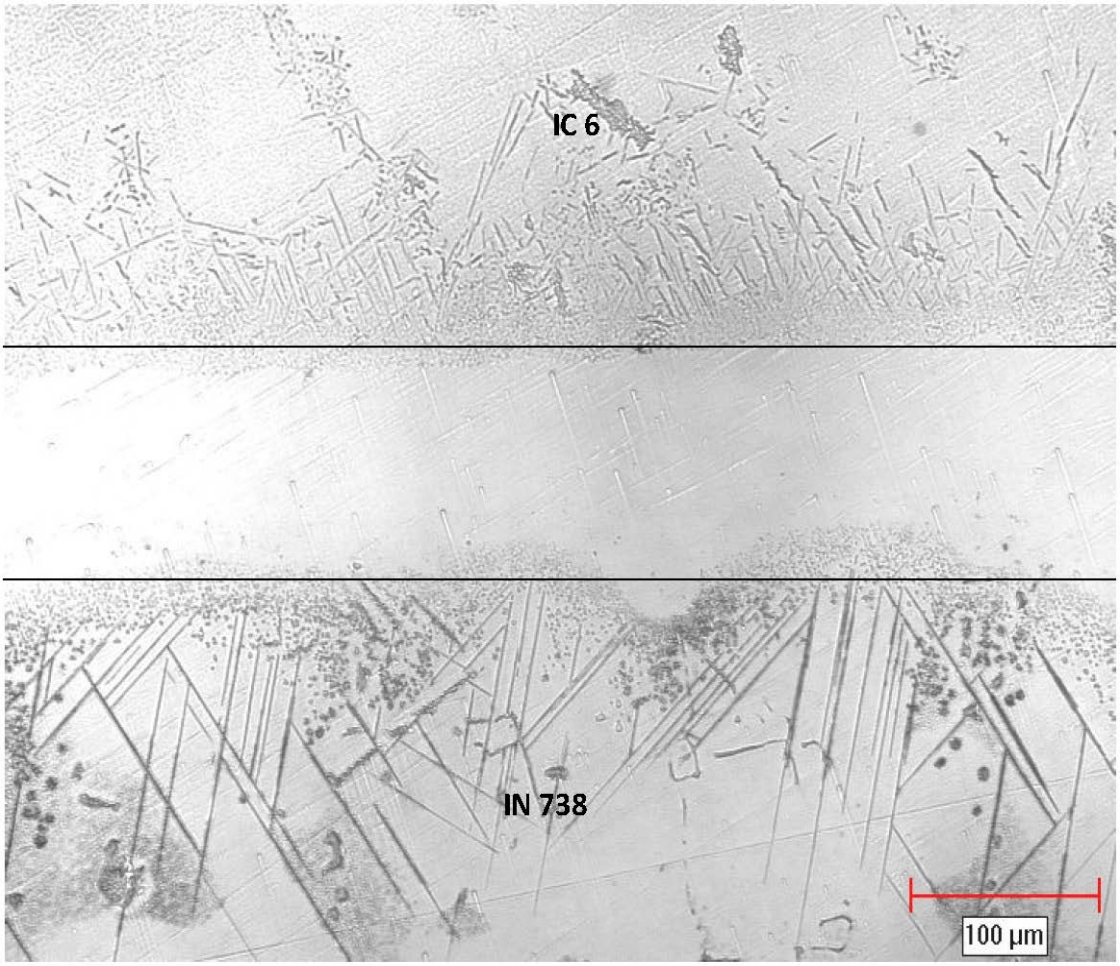

Figure 4. 55: Micrograph of joint between IN 738 and IC-6 showing the formation of second phase precipitates in substrate region adjacent to the joint

Microstructural study of the joint between IN 738 and IC 6 showed the formation of second phase precipitates that are rich in Mo and B within the substrate region that is adjacent to the TLP joint in both IN 738 and IC 6 (Figure 4.52). Similar formation of the second phase precipitates have been observed in IN 738 to IN 738 and IC-6 to IC-6 joints and the precipitates were confirmed by detailed transmission electron microscopy to be rich in Mo and B [125]. Therefore, a higher capability of the alloy IC 6, which is richer in Mo, in accommodating the diffusing boron atoms from the interlayer liquid, through the extensive formation of Mo-rich borides, appears to have curtailed an increase in t_f with temperature, which is in agreement with the numerical model prediction.

CHAPTER 5: SUMMARY AND CONCLUSIONS

5.1 Development of 2-D TLP Bonding Numerical Model and Investigation of the Effect of Grain Boundaries on Bonding Kinetics

A new 2-D, fully implicit, moving-mesh finite element simulation model has been developed and used to study the influence of grain boundaries in polycrystalline solids on diffusion-controlled solidification during TLP bonding. Major results and conclusions are summarized as follows:

1. the model was found to conserve solute in space and time and its calculated solutions are unconditionally stable and in good agreement with the experimental results;
2. numerical simulations by the model and experimental verification showed that enhanced diffusivity along grain boundary regions cannot be solely used to explain the influence of grain boundaries on the rate of diffusional solidification during TLP bonding;
3. instead, the numerical calculations confirmed that the mechanism by which grain boundaries can influence TLP bonding kinetics is through grain boundary grooving, which is influenced by liquid-solid interfacial energy, grain boundary energy and grain boundary diffusivity;
4. nevertheless, even with the occurrence of grain boundary grooving, the study shows that the effect of grain boundaries on the time required to achieve complete diffusional solidification is negligible in cast Ni-based superalloys; and
5. Contrary to previous assumptions, in cast Ni-base superalloys, reducing the number of grain boundaries by directional solidification casting techniques would not prohibitively

prolong the t_f required to achieve complete isothermal solidification during TLP bonding.

5.2 Numerical Simulation and Experimental Study to Reduce Isothermal Solidification Completion Time during TLP Bonding of Single Crystals

The new finite element numerical simulation model, coupled with experimental verification, was used to study the underlying cause of elongation of processing time t_f and its reversed temperature dependence during TLP bonding of SX Ni-base superalloys. The key results and conclusions are summarized as follows;

1. In contrast to previous assumptions, the elongation of t_f and its anomalous increase with temperature above a critical temperature T_c cannot be explained by competition between solubility and diffusivity of solutes as suggested by standard analytical TLP bonding models;

2. instead, departure from parabolic diffusion-controlled migration of liquid-solid interface with holding time was found to be the fundamental phenomenon responsible for (1);

3. numerical calculations showed that a possible way of reducing the effect of the deviation phenomenon on the elongation of t_f is by reducing the initial concentration of the MPD solute in the interlayer material;

4. a numerical modeling program based on cellular automata method was developed and coupled with the finite element simulation model to study the possibility of using a mixture of brazing alloy and base alloy powders as interlayer material to reduce the solute concentrations in the interlayer, C_{FI}, and, thus, t_f while avoiding stray-grain formation in joints between SX substrates;

5. a theoretical analysis showed that through the proper selection of (i) the ratio of the volume of brazing alloy powder particles to that of the gap-filler particles, $R_{B/G-F}$ (ii) bonding temperature (iii) concentration of MPD in the brazing alloy, C_{FB} and (iv) initial size of the gap-filler powder particles, P_s, it is possible to use the powder mixture to prevent stray-grain formation and reduce t_f ;

6. the prediction of the model was experimentally validated. A powder mixture of brazing and base alloys was used as the interlayer material to produce stray-grain-free joints between SX superalloy substrates, an approach which has not been found or reported for SXs in the literature.

7. the powder mixture used as interlayer material was also experimentally observed to significantly reduce processing time t_f at temperatures where deviation from parabolic phenomenon was active.

8. the powder mixture approach elucidated in this work is beneficial for SX materials not only with respect to minimizing $t_{f,}$ but also reducing undesirable liquid phase dissolution of the substrate material, which is also known as erosion, and enabling desirable enrichment of the joint region with gap-filler alloying elements.

5.3 Application of the New Numerical Model to TLP Bonding of a Ni_3Al-Based Intermetallic Material and Dissimilar Materials

5.3.1 TLP bonding of Ni_3Al-Based Intermetallic Alloy IC 6

The new numerical simulation model developed in this work has been applied to understand the TLP bonding behavior in another type of new generation heat resistant aerospace material, Ni_3Al-based intermetallic alloy IC 6. The key results and conclusions are summarized as follows:

1. the time required to prevent formation of deleterious centerline eutectic through complete isothermal solidification during TLP bonding of SX intermetallic alloy IC 6 was found to be in good agreement with the value calculated by the numerical model developed in this work;

2. it was observed that boron addition to alloy IC 6 did not excessively extend the time required to achieve complete isothermal solidification during joining, compared to boron-free alloy; and

3. the behavior in (2) can be explained by the partitioning behavior of boron atoms into interdendritic particles during directional solidification of the cast alloy IC 6,

4. furthermore, experimental observation confirmed the applicability of a major theoretical prediction of the new numerical model to the Ni_3Al-based intermetallic alloy IC 6, in that, stray-grain-free joint was produced in the material by using the beneficial powder mixture interlayer approach.

5.3.2 Asymmetric Diffusional Solidification during TLP Bonding of Dissimilar Materials

The non-symmetry aspect inherent in the new numerical simulation model was exploited to study asymmetric diffusional solidification behavior during TLP bonding of dissimilar alloys. Major results and conclusions are summarized as follows:

1. in contrast to previous suggestions in the literature, the present study showed that asymmetric distribution of residual interlayer liquid during TLP bonding of dissimilar alloys, polycrystalline and single crystal superalloys, is attributable to mismatch between lattice diffusion coefficients in the alloys irrespective of enhanced intergranular diffusivity;

2. numerical calculations show that, similar to the case of joining similar substrates, departure from diffusion-controlled parabolic displacement of the liquid-solid interface with holding time can cause an increase in the processing time t_f required to produce reliable eutectic-free joint between dissimilar alloys; and

3. a possible way to curtail such undesirable occurrences, which is independent of solute diffusivity, involves coupling a material with another type that exhibits a higher capability of accommodating the diffusing MPD solute.

CHAPTER 6: SUGGESTIONS FOR FUTURE WORK

The theoretical and experimental work performed in this study has shown that it is possible to use powder mixture of brazing and base alloys as interlayer material for TLP bonding of SX superalloys. Aside from the fact that the approach minimizes the processing time required to produce reliable high temperature joint free of eutectic microconstituents, which has been recognized to be deleterious to mechanical properties, it also enriches the joint region with base material alloying elements that are critical to high temperature performance. This could be crucial with regard to new generation SX Ni-base superalloys that contain vital alloying heavy elements like Re, Ta, W and Ru, but which slowly diffuse in Ni. Inclusion of base alloy powder particles containing these elements, as additive gap-filler in the interlayer material, could have significant impact on high temperature mechanical properties of bonded materials. It is suggested that relevant high temperature testing of mechanical properties like creep, low cycle fatigue and thermo-mechanical fatigue of single crystal materials bonded with the use of the composite powder mixture be performed to evaluate the extent of benefits, with regard to mechanical performance, offered by this joining technique.

Likewise, this study shows that while the use of a composite powder mixture as the interlayer material in TLP bonding can produce stray-grain free joints between SX substrates, the approach can also be used to produce polycrystalline joint, depending on the choice of processing parameters, which is relevant when joining conventional polycrystalline base materials. The size of the grains in the joint region subsequent to complete isothermal solidification of the liquated insert may be required to be comparable to that of the base materials in order to enable an optimum high temperature load bearing performance. The final

grain size in the joint would be dependent on a variety of factors including, (i) bonding temperature, (ii) type and concentration of MPD solute in the brazing alloy powder, (iii) volume ratio of the brazing alloy powder to the base alloy powder, (iv) size of powder particles in the composite interlayers, (v) total time spent at the bonding temperature both prior and after complete isothermal solidification (vi) grain size of the base material and (vii) application of post bond heat treatment. A methodical numerical modeling simulation and experimental study of how all these factors concurrently and cumulatively control final grain size and the influence of resultant grain size and structure on various relevant high temperature mechanical properties are recommended. It is envisaged that with these suggestions, the potential benefits of utilizing a composite powder mixture of brazing and base alloys as the interlayer material during the TLP bonding of SX and heat resistant polycrystalline alloys in structural engineering can be maximized for industrial applications.

The coupled cellular automata and finite element simulation models developed in this work permitted the study of a number of important aspects in TLP bonding that could not have been studied with existing analytical and numerical TLP bonding models. It allowed for a more realistic modeling of the process with a decreased number of assumptions used in the calculations. Further development of the model can be done by incorporating higher level systems, such as studying the effect of secondary MPD solute in the interlayer on the time required to achieve complete base-alloy dissolution and isothermal solidification. The multi-scale approach used in this work using by coupling the cellular automata and finite element methods can be further developed to allow for predicting not only the microstructural evolution at the joint but also predict its mechanical properties, such as stress distributions at the bonded

joint and extent of deformation under axial loading, thermal stress, creep and fatigue loading. The multi-scale approach can also be further developed to use atomistic simulation techniques such as molecular dynamics, density functional theory, lattice Boltzmann methods to predict the diffusional properties of the MPD solutes at grain boundaries at an atomic scale during TLP bonding. This will enable the estimation of diffusion parameters required for the micro- and meso-scale simulations with a greater level of accuracy.

REFERENCES

[1] Beiber G.C., Hihalisin R.J, 2nd International Conference on the Strength of Metals and Alloys, Asilomer, ASM, Vol.4 (1966) pg. 1031.

[2] Duvall D.S., Oczarski W. A., Weld. J., Vol. 46, No. 9 (1967) pg. 423

[3] Duvall D.S. Owczarski W.A., Paulonis D.F., Weld. J., Vol. 53, No. 4 (1974) pg. 203-214

[4] Abdelfatah M., Ojo O.A. , Met. and Mat. Trans. A, Vol. 40A (2009) pg. 377-385

[5] Reed R., "The Superalloys: Fundamentals and Applications", Cambridge Press, UK (2006) pg. 34-54, 121-130

[6] Sims C., Stoloff N., Hagel W., "Super Alloys II", John Wiley & SOns, New York (1987) pg. 97-118

[7] Jena A.K. Chturvedi M.C., J. Mat. Sci., Vol.19 (1984) pg. 3121

[8] Chen Q. Z., Knowles D.M., Acta Mat., Vol. 50 (2002) pg. 1095-1112

[9] Reed R.C., Jackson M.P., Na Y.S., Met. and Mat. Trans A, Vol 30A (1999) pg 521-533

[10] Oynszko A, Kubiak K., Sieniawski J., JAMME, Vol. 32 (2009) pg.(66-69)

[11] Kear B.H., Pircey B.J., Trans. Met. Soc. AIME, Vol 239 (1967) pg. 1209-1218

[12] Kou S., “Welding Metallurgy”, 2nd ed., Wiley & Sons Inc., USA, 2003, pg. 3 - 32

[13] Owczarski W.A., Duvall D. S., Sullivan C.P., Weld. J., Vol 44 (1966) pg. 145-s

[14] Heafkens M.H. , Matthey G.H., Weld. J., Vol 61 (1982) pg. 25

[15] Ojo O.A., Richards N.L. Chaturvedi M.C., Scripta Mat., Vol. 50 (2004) pg. 641-646

[16] Schwartz M., “Brazing”, 2nd ed., ASM International, USA (2003) pg. 4–61, 341

[17] Jacobson D.M., Humpston G., “Principles of Brazing”, ASM International (2005) pg. 3– 45

[18] Donachie M.J., Donachie S.J., “Superalloys – A Technical Guide”, 2nd ed., ASM International (2002)

[19] Gale W.F., Butts D.A. Sci Tech.W. J., Vol. 9, No.4 (2004) pg. 283-300

[20] Kotval P.S., Venables J.D., Calder R.W., Met. Trans., Vol. 3 (1972) p. 453

[21] Huang J., Dong Y., Wan. Y., Zhao X., Zhang H., Mat. Proc. Tech., Vol.190 (2007) pg. 312-316

[22] Wu. X.W., Chandel R.S., Seow H.P., Li H., Mat. Proc. Tech., Vol. 113 (2001) pg. 215-221

[23] Zhuang W.D., Eager T.W., Sci. Tech. W. J., Vol. 5 (2000) pg. 125-135

[24] Tuah-Poku I., Dollar M., Massalski T. B., Metall. Trans., Vol. 19A (1988) pg. 675– 686

[25] MacDonald W.D., Eager T.W., Annu. Rev. Mater. Sci., Vol. 22 (1992) pg. 23–46

[26] Niemann J. T., Garret R. A., Weld. J., Vol. 52 (1974) pg. 175-184

[27] Zhou Y., Gale W.F., North T.H., Inter. Mat. Rev., Vol. 40, No. 5, (1995) pg. 181–196

[28] Nakao Y., Nishimoto K., Shinozaki K,, Kang C., International Institute for Welding, Document no. IA-334-86-OE, UK, (1986)

[29] Nakao Y., Nishimoto K., Shinozaki K,, Kang C., Schweissen und Scneiden Germany, Vol. 44, No.2 (1992), pg. 87

[30] Gale W.F., Wallach E.R., Met. Trans., Vol. 22 A (1991) pg. 2451 – 2457

[31] Zhou Y., J. Mat. Sci. Let., Vol. 20 (2001) pg. 841-844

[32] Tuah-Poku I., Dollar M., Massalski T.B., Metall. Trans., Vol 19A (1988) pg. 675

[33] Lesoult G., Center for Joining of Materials Report, Carnegie Mellon University, Pittsburgh, PA (1976)

[34] Sakamoto A., Fujiwara C., Hattori T. Sakai S., Weld. J., Vol. 68 (1989) pg. 63

[35] Ramirez J., Liu S., Weld. J., Vol. 71 (1992) pg. 365s

[36] Illingworth T.C., Golosnoy I.O., Gergely V., Clyne T.W., J. Mat. Sci., Vol 40, 2005, pg. 2505 – 2511

[37] Zhou Y., North T.H., Mater. Sci. Eng., Vol. 1, No. 4 (2003), p. 505

[38] H. Nakagawa, C. H. Lee, Metall. Trans. A, Vol 22, No 2, 1991, pg. 543-555

[39] Watanabe T., Mat. Sci. Eng., Vol 11 (1984), pg. 47-84

[40] Watanabe. T, Mat. Sci. Eng., Vol. 166A (1993) pg. 11-28

[41] Harrison L.G., Trans. Faraday. Soc., Vol 57 (1961) pg. 1191

[42] Hart E.W., Acta. Metall., Vol 5 (1957) pg. 597

[43] Fisher J.C., J. Appl. Phys., Vol. 22 (1951) pg. 74

[44] Lidiard A.B., Tharmalingam K., Disc. Faraday Soc., Vol.28 (1959) pg. 64

[45] Peterson N.L., Int. Met. Rev., Vol. 28 (1983) pg. 65-91

[46] Hillert M., Purdy GR. , Acta Metall, Vol. 26 (1978) pg. 330-340

[47] Ping D.H., Gu Y.F., Cui C.Y., Harada H., Mat. Sci. Eng A, Vol. 456 (2007) pg. 99-102

[48] Mullins W.W., J. Appl. Phy. Vol. Vol. 28 (1957) pg. 333

[49] Allen B.C., Trans AIME, Vol. 236 (1966) pg. 915-924

[50] Saida K., Zhou Y., North T. H., Journal of Materials Science, Vol. 28 (1993) pg. 6427-6432

[51] North T.H., Ikeutch K., Zhou Y., Kokawa H., TMS Symposium (1991) pg. 83-91

[52] Tuah-Poku I., Dollar M. Massalski T.B., IBID, Vol 19A (1988) pg. 675

[53] Kokawa H., Lee C.H., North T.H., Metall. Trans., Vol 22A (1991) pg. 1627

[54] Crank J. The Mathematics of Diffusion, Oxford University Press, Oxford (1975)

[55] Javierre E., Vuik C., Vermolen F.J., Van der Zwaag S, J. Comp. Appl. Math., Vol.192 (2006) pg. 445-459

[56] Sethian J.A., Osher S., J. Comp. Phys., Vol 79 (1988) pg. 1-21

[57] Sethian J.A. Level Set Methods and Fast Marching Methods, Cambridge University Press, New York (1999)

[58] Tan L., Zabaras N, J. Comp. Phys., Vol. 211 (2006) pg. 36-63

[59] Tan L., Zabaras N, J. Comp. Phys., Vol. 226 (2007) pg. 131-155

[60] Javierre E., Vuik C., Vermolen F.J., Segal A., J. Comp. Phys. Vol. 224 (2007) pg. 222-240

[61] Li. C, Xu C., Gui C., Fox M., IEEE Trans Image Proc., Vol. 19, No. 12 (2010) pg. 3243-3254

[62] Janssens K., Raabe D., Kozeschnik E., Miodownik M, Nestler B., Computational Materials Engineering, Elsevier Publishing, UK (2007)

[63] Caginalp G., Phys. Rev. A, Vol. 39 (1989) pg. 5887

[64] Karma A., Phys. Rev. Lett., Vol. 87 (2001) pg. 1-4

[65] Provatas N., Goldfield N., Dantzig J., Phys. Rev. Lett., Vol. 80 (1998) pg. 3308-3311

[66] Ulam S., Proc. Int. Congr. Math., Vol. 2 (1952) pg. 264-275

[67] Wolfram S., Physica 10D (1984) pg. 1-35

[68] Li Y., Xu Q., Baicheng L., Tsinghua Sci. Tech., Vol. 11, No.5 (2006) pg. 495-500

[69] Raghavan S., Sahay S., Mat. Sci. Eng. A, Vol. 445 (2007) pg. 203-209

[70] Janssens K. Math. Comp. Sim., Vol. 80 (2010) pg. 1361-1381

[71] Rappaz M. Gandin C., Acta Metall. Mat., Vol 41, No. 2 (1993) pg. 345-360

[72] Gandin C., Rappaz M., Acta Mater., Vol. 45, No. 5 (1997) pg. 2187-2195

[73] Krane M., Johnson D., Raghava S., Appl. Math. Mod., Vol. 33 (2009) pg. 2234-2247

[74] Schonfisch B., BioSystems, Vol. 41 (1997) pg. 29-41

[75] Potts R.B., Proc. Comb. Phil. Soc., Vol. 48 (1952) pg. 106

[76] Anderson M. P., Grest G. S., Srolovitz D. J., Scripta Met., Vol. 19 (1985) pg. 225-230

[77] Ivasishin O.M., Shechenko S.V., Vailiev N.L., Semiatin S.L., Mat. Sci. Eng. A, Vol. 433 (2006) pg. 216-232

[78] Fjeldberg E., Marthinsen K., Comp. Mat. Sci, Vol. 48 (2010) pg. 267-281

[79] Harris R., Grant M., J. Phys. A, Vol. 23 (1990) pg. L567-L571

[80] Jorgenson L., Harris R., Mat. Sci. Eng. A, Vol.173 (1993) pg. 89-92

[81] Plapp M., Karma A., J. Comp. Phys., Vol. 165 (2000) pg. 592-619

[82] Zhou Y. North T.H. Mod. Sim. Mater. Sci. Eng., Vol. 1 No. 4 (1993) pg. 505

[83] Nakagawa H., Lee C. H., Metall. Trans. A, Vol 22, No 2 (1991) pg. 543-555

[84] Cain S. R., Wilcox J. R., Venkatraman R., Acta Mat., Vol 45, No. 2 (1997) pg. 701

[85] Shinmura T., Ohsasa K., Narita, Mat. Trans. JIM, Vol. 42, No. 2 (2001) pg. 292

[86] Tanzilli R.A., Heckel R.W., Trans. A.I.M.E. Vol. 242, 1968, p. 2312

[87] Illingworth T.C., Golosnoy I.O., Gregely V., Clyne T.W., J. Mat. Sci., Vol 40 (2005) pg. 2505-2511

[88] Zhou Y., North T.H. Acta Metall. Mater., Vol 42 No. 3 (1994) pg. 1025-1029

[89] Brener E.A., Temkin D. E., Acta Mater., Vol. 50 (2002) pg. 1707-1716

[90] Yang F., Comp. Mat. Sci., Vol. 7 (1997) pg. 279-284

[91] Mullins W.W., J. Appl. Phy. Vol. 28 (1957) pg. 333

[92] H. J. Vogel and L. Ratke, Acta Metall. Mater., Vol 39, 1991, pg. 641

[93] Bokstein B.S., Klinger L.M., Apikhtina I.V., Vol. A203 (1995) pg. 373-376

[94] Tuah-Poku I., Dollar M., Massalski T. B., Metall. Trans. (1988) Vol. 19A, p. 675– 686

[95] Ikeuchi K., Zhou Y., Kokawa H., North T. H., Metall. Trans. A, Vol. 23A (1992) pg. 2905

[96] Hutton D. V., Fundamentals of Finite Element Analysis, McGraw-Hill, 2000

[97] Patel P. D., AIAA Journal, Vol. 6 (1968) pg. 2454

[98] Swalin R. A., Thermodynamics of Solids, Hohn Wiley & Sons Inc., New York, NY, (1962) pg. 180-187

[99] Shewmon P.G., Physical Metallurgy, R. W. Cahn ed., North-Holland Publishing Co., New York, NY (1970) pg. 303-306

[100] Liu W., Jin T., Sun X. F., Guo Y., Guan H. R. , Hu Z. Q., Scripta Mater. Vol. 48 (2003) pg 1283-1288

[101] W. D. MacDonald and T. W. Eagar, Metall. & Mater. Tran. A. Vol. 29A (1998) pg 315–325

[102] Kokawa H., Lee C. H. and North T. H., Metall. Trans. A, Vol. 22A (1991) pg 1627-1631

[103] Peterson N. L., Int. Met. Rev., Vol. 28 (1983) pg. 65-91

[104] Patterson B. R. and Liu Y., Metall. Tran. A, Vol. 23A (1992) pg 2481 – 2482

[105] Gell M., Duhl D. N., Gupta D. K. and Sheffler K. D., J. Met., Vol. 39 (1987) pg 11-15

[106] Idowu O. A., Richards N. L., Chaturvedi M. C., Mat. Sci. Eng. A, 397 (2005) pg. 98-112

[107] Tokoro K., Wikstrom N., Ojo O.A. and Chaturvedi M.C., Mater. Sci. Eng. A 477 (2008) p.311.

[108] Xinjian Y., Myung B.K. and Chung Y.K., Metall. Mater. Trans. A 42 (2011) pg1310

[109] Kuntz M.L., PhD dissertation, University of Waterloo, Waterloo (2006)

[110] Dinkel M.K., Heinz P., Pyczak F., Volek A., Ott M., Affeldt E., Vossberg A., Goken M.

and Singer M.F., Proc. Superalloys 2008 (2008) p.211.

[111] Illingworth T.C., Golosnoy I.O. and Clyne T.W., Mater. Sci. Eng. 445/446, (2007) p.493.

[112] Prakash C.P., Ali M., Huang X. Jean-Francois T., Proc. of 43rd Conference of 450 Metallurgist, Canada (2004) p 413.

[113] Enomoto M., Nojiri N., Scrip. Mater., Vol. 36 No. 6 (1997) pg. 625-632.

[114] Tundal U.H., Ryum N., Met. Trans. 23A (1992) pg. 433–449.

[115] Vermolen F.J., Slabbekoorn H.M., Zwaag S., Mat. Sci. Eng. A,, Vol. 231 (1997) pg. 80- 89

[116] Sasikumar R., Sreenivasan R., Acta Met. Mater. 42 (1994) 2381–2386.

[117] Ojo OA., Ding R.G., Chaturvedi M.C. Scripta Mater, Vol. 54 (2006) pg. 2131.

[118] David S.A., Jemian W.A., Liu C.T., Horton J.A., Weld J, Vol.64 (1985) pg. 22s.

[119] Molian P.A., Yang Y.M., Srivatsan T.S., J Mater Sci, Vol. 27 (1992) pg. 1857.

[120] Patterson R.A., Martin P.L., Damkroger B.K., Christodoulou L. Weld J (1990) pg. 39s–44s.

[121] Ding R.G., Ojo OA., Chaturvedi M.C., Intermetallics Vol. 15 (2007) pg.1504.

[122] Abdelfatah M.M., Ojo OA., Metall Mater Trans A, Vol. 40 (2009) pg. 377.

[123] Villars P, Prince A, Okamoto H, Handbook of ternary alloy phase diagrams. ASM International, Metals Park, OH (1993)

[124] Ohsassa K, Shinimura T, Narita T, J. Phase Equilibria, Vol. 20 (1999) pg. 199

[125] Zhang, H. R., Ghoneim, A. and Ojo, O.A., Journal of Mater. Sci., Vol. 46 (2010) pg. 429

[126] Chalmers B.A.. Principles of solidification, John Wiley, New York (1964).

[127] Liao P.K., Spear K.E., Bull. Alloy Phase Diagrams, Vol. 7 (1986) pg. 550–555.

[128] Han Y.F., Xiao C.B. Report on alloy IC6 and IC6A. Beijing Institute of Aeronautical Materials, China (2004).

[129] Nishimoto, K., Saida, K., Kim, D. and Nakao, Y., ISIJ International, Vol. 35 (1995) pg. 1298

[130] Idowu, O. A., Ojo, O. A. and Chaturvedi, M. C. Metall. and Mater. Trans. A, Vol. 37 (2006) pg. 2787

[131] Zhang, H. R., Ojo, O. A and Chaturvedi, M. C., Scripta Mater. Vol. 58 (2008) pg.167

Refereed International Journal Publications from this Thesis

1. **A. Ghoneim** and O. A. Ojo, "*Understanding Reversed Temperature Dependence of Diffusional Solidification Time in Single Crystal Superalloy Brazement*" Philosophical Magazine (Manuscript Accepted, In Press 2011)

2. **A. Ghoneim** and O. A. Ojo; "*Numerical Simulation of Diffusional Solidification during Transient Liquid Phase Bonding of Dissimilar Materials*" Metallurgical and Materials Transactions A (Manuscript Accepted, In Press 2011)

3. **A. Ghoneim** and O. A. Ojo, "*Numerical Modeling and Simulation of Diffusion-Controlled Liquid-Solid Phase Change in Polycrystalline Solids*", Computational Materials Science, Vol. 50, No. 3 (2011) pg 1102-1113
4. H. R. Zhang, **A. Ghoneim** and O.A. Ojo, "*TEM Analysis of Diffusion Brazement Microstructure in a Ni_3Al-based Intermetallic Alloy*" Journal of Materials Science, Vol. 46, No. 2 (2011) pg. 429-437
5. **A. Ghoneim** and O. A. Ojo, "*On the Influence of Boron-Addition on TLP Bonding Time in a Ni_3Al-Based Intermetallic*" Intermetallics, Vol. 18, No. 4, (2010) pg 582-586.

Refereed International Conference Proceeding Publication from this Thesis

6. **A. Ghoneim**, O. A. Ojo and M. C. Chaturvedi "*Effect of Solute Solubility on Increased Processing Time during Transient Liquid Phase Bonding*" 4th International Brazing and Soldering Conference (April 26-29 2009), Orlando FL USA.